HOKKAIDO UNIVERSITY

Title	Effect of off-stoichiometry on the half-metallic character of quaternary Heusler alloy Co2(Mn,Fe)Si
Author(s)	Ayele, Kidist Moges
Degree Grantor	北海道大学
Degree Name	博士(工学)
Dissertation Number	甲第12401号
Issue Date	2016-09-26
DOI	https://doi.org/10.14943/doctoral.k12401
Doc URL	https://hdl.handle.net/2115/63330
Type	doctoral thesis
File Information	Ayele_Kidist_Moges.pdf

Hokkaido University Collection of Scholarly and Academic Papers : HUSCAP

Effect of off-stoichiometry on the half-metallic character of quaternary Heusler alloy $Co_2(Mn,Fe)Si$

A Doctoral Dissertation Submitted to

The Division of Electronics for Informatics

Graduate School of Information Science and Technology

Hokkaido University

by

Kidist Moges Ayele

August 2016

Copyright (C) 2016 Kidist Moges Ayele. All Rights Reserved.

ABSTRACT

The search for electronic devices with better functionalities such as nonvolatility, reconfigurable logic functions, and low power consumption led to a novel area of electronics, called spintronics. Spintronic devices utilize the spin degree of freedom of the electron in addition to its charge. Thus, the creation of a highly spin-polarized current is essential for spintronic devices. Originating from the existence of an energy gap at the Fermi level (E_F) for one spin direction (mostly the minority-spin band), half-metallic ferromagnets (HMFs) feature complete spin polarization at E_F. Accordingly, HMFs are seen as one of the most suitable spin source materials for spintronic devices. Co-based Heusler alloys (Co_2YZ, where Y is usually a transition metal and Z is a main group element) are among the most extensively applied to spintronic devices, including magnetic tunnel junctions (MTJs), in particular those with a MgO tunnel barrier, giant magnetoresistance (GMR) device, and to spin injection into semiconductors. One of the notable advantages of Co_2YZ is that they feature a variety of materials, including not only ternary alloys but also quaternary alloys, thereby providing flexibility in their application to spintronic devices.

One quaternary Heusler alloy system, $Co_2(Mn_{1-x}Fe_x)Si$, has been studied from the view point of tuning the E_F position around the center of the half-metal gap by changing the composition x in $Co_2(Mn_{1-x}Fe_x)Si$ in order to control the valence electron number per formula unit, Z_t. In practice, off-stoichiometry in Co_2YZ thin films prepared by magnetron sputtering or molecular beam epitaxy is inevitable and leads to structural defects. If the minority-spin in-gap states are introduced at E_F by a structural defect for a half-metallic thin film, the half-metallicity is strongly degraded. Thus, it is important to understand the effect of defects associated with off-stoichiometry on half-metallicity in order to take full advantage of the half-metallic character of Co-based Heusler alloys.

H. Liu et al. from our research group recently investigated the influence of varying the film composition of $Co_2(Mn,Fe)Si$ (CMFS) Heusler alloy on the tunneling magnetoresistance (TMR) characteristics of fully epitaxial CMFS/MgO/CMFS MTJs (CMFS MTJs) with $Co_2Mn_{\alpha}Fe_{\beta}Si_{0.84}$ electrodes. Through this study, we demonstrated giant TMR ratios of 2610% at 4.2 K and 429% at 290 K for CMFS MTJs with Mn-rich,

lightly Fe-doped CMFS electrodes.

The main purpose of the present study was to clarify the effect of off-stoichiometry on the half-metallicity of quaternary Heusler alloy CMFS. To do this, we experimentally investigated the film composition dependence of the saturation magnetization per formula unit, μ_s, of CMFS films with various compositions of α' and β' in $Co_2(Mn_{\alpha'}Fe_{\beta'})Si_{0.84}$, and that of the TMR ratio of CMFS MTJs, in combination with first-principles calculations. Furthermore, in order to clarify the origin of the giant TMR ratios demonstrated for CMFS MTJs with Mn-rich, lightly Fe-doped CMFS electrodes, we experimentally investigated how the TMR ratio of CMFS MTJs with lightly Fe-doped CMFS electrodes depends on the Mn composition α' in $Co_2(Mn_{\alpha'}Fe_{0.16})Si_{0.84}$ electrodes in the Mn-rich composition region. Finally, in this dissertation, we investigated the bias voltage dependence of the spin-dependent differential tunneling conductance of the CMFS and CMS MTJs along with its origin. To do this, we studied the dI/dV versus V characteristics (= G spectra) of MTJs having CMFS and CMS electrodes that showed giant TMR ratios.

This dissertation is organized into six chapters and the main content of each chapter is as follows:

Chapter 1 gives the general introduction and background of this dissertation. It first reviews important experimental and theoretical backgrounds related to this study, details the experimental investigation and result of the influence of film composition on the TMR characteristics of fully epitaxial CMFS MTJs and then it provides the overall purpose and approaches of this dissertation.

Chapter 2 describes the overall experimental and computational methods followed in this dissertation. It first details the sample preparation, structural characterization and measurement techniques of the samples prepared in this study and then it explains the theoretical and computational methods.

Chapter 3 details the effect of off-stoichiometry on the half-metallic character of CMFS investigated by studying the film composition dependence of μ_s and the TMR ratio for two series of CMFS films. The experimentally investigated μ_s and TMR ratios in combination with first-principles calculations indicated that $Co_{Mn/Fe}$ antisites in the quaternary alloy are detrimental to half-metallicity, in a similar way as in ternary alloy CMS. It was demonstrated that (Mn+Fe)-rich compositions are highly effective at

suppressing harmful $Co_{Mn/Fe}$ antisites and that a relatively small Fe ratio in the total (Mn+Fe) composition retains a half-metallic state.

Chapter 4 clarifies the origin of the giant TMR ratio obtained for CMFS MTJs with Mn-rich, lightly Fe-doped CMFS electrodes through the dependence of the TMR ratio of CMFS MTJs with $Co_2Mn_{\alpha'}Fe_{0.16}Si_{0.84}$ electrodes on α' in the Mn-rich composition region. It was revealed that residual $Co_{Mn/Fe}$ antisites were further suppressed in lightly Fe-doped CMFS due to the fact that the available (Mn+Fe) composition in (Mn+Fe)-rich CMFS became larger than the critical Mn composition in Mn-rich CMS. This resulted in giant TMR ratios for CMFS MTJs with Mn-rich, lightly Fe-doped CMFS electrodes. Furthermore, it was revealed from the dI/dV versus V characteristics that the Fermi level position of the Mn-rich, lightly Fe-doped CMFS was pushed up to around the center of the half-metal gap by an increase in the Z_t value due to small Fe doping compared with Mn-rich Co_2MnSi. This result supported our finding of the enhanced half-metallicity of the Mn-rich, lightly Fe-doped CMFS obtained by the film composition dependence of the TMR ratio.

Chapter 5 examines the bias voltage dependence of the spin-dependent differential tunneling conductance of CMFS and CMS MTJs along with the origin of this dependence. Clear dip structures were found in the G spectra for the antiparallel magnetization alignment (AP) in a small bias region of up to ±70 mV. Moreover, it is found that the dI/dV value for AP at characteristic voltages, $V_s = \pm 70$ mV, normalized by the value at $V = 0$ increased linearly with the TMR ratio at 4.2 K. Thus, it was clarified that MTJs having electrodes with higher spin polarization showed stronger bias voltage dependence. This feature was consistently explained by spin-flip tunneling via a magnon excited by a hot electron along with the strong temperature dependence of tunneling conductance for AP by spin-flip tunneling via a thermally excited magnon.

Chapter 6 summarizes and concludes this dissertation.

In summary, the findings of this dissertation indicate that the approach to controlling off-stoichiometry and film composition is promising for fully utilizing the half-metallicity of quaternary CMFS thin films as spin source materials.

Table of Contents

List of Figures ..... **VI**

List of Tables ..... **VIII**

1. Introduction **1**

1.1. Spintronic devices and their applications 1

1.2. Operation principle of MTJs 2

1.3. MTJs with half-metallic ferromagnetic electrodes 5

1.4. Influence of film composition on the TMR characteristics of CMFS MTJs 9

1.5. Purpose and approach 16

2. Experimental and Computational methods **17**

2.1 Sample preparation and characterization of CMFS-based thin films 17

2.2 Computational methods 24

2.3 Formula unit composition model 24

2.4 Preparation and characterization of MTJ layer structures 27

2.5 Summary 34

3. Effect of off-stoichiometry on the half-metallic character of quaternary Heusler alloy CMFS **35**

3.1 Results and discussion 36

3.2 Summary 46

4. Origin of the giant TMR ratios obtained for CMFS MTJs **47**

4.1 Investigation via μ_s and TMR ratio 48

4.2 Half-metallic electronic structure of Mn-rich, lightly Fe-doped CMFS 56

4.3 Summary 63

5. Bias voltage dependence of the spin-dependent tunneling conductance of CMFS MTJs 64

5.1 Experimental results and discussion 66

5.2 Correlation between bias voltage dependence and temperature dependence 77

5.3 Summary 78

6. Conclusion 79

Acknowledgements 81

References 83

Appendix 88

List of Figures

Fig. 1.1. A schematic diagram of the first MRAM product from Freescale Inc. with a 4M bit capacity having an MTJ as a memory element..... 2

Fig. 1.2. A schematic diagram of the structure of a magnetic tunnel junction (MTJ). 4

Fig. 1.3. A schematic diagram showing the basic spin-dependent tunneling mechanism occurring in MTJs. 4

Fig. 1.4. A schematic diagram showing the spin-resolved density of states (DOS) of half-metallic Heusler alloys. 6

Fig. 1.5. Theoretically calculated spin-resolved total density of states (DOS) of half-metallic Co_2MnSi Heusler alloy. 7

Fig. 1.6. TMR ratios at (a) 4.2 K and (b) 290 K for CMFS/MgO/CMFS MTJs (CMFS MTJs) as a function of (Mn + Fe) composition. 10

Fig. 1.7. TMR ratios at (a) 4.2 K and (b) 290 K for CMFS MTJs as a function of β' for a fixed δ = 1.40.... 15

Fig. 2.1. Cross sectional image of the layer structure of a CMFS thin film. 18

Fig. 2.2. RHEED pattern of a CMFS thin film after annealed at 600^{o}C showing an epitaxial growth of the film on MgO buffer. 20

Fig. 2.3. Typical magnetic hysteresis curves for (a) series-A and (b) series-B CMFS films at 10 K measured using a SQUID magnetometer. 22

Fig. 2.4. Typical low angle x-ray reflectivity scan of a CMFS thin film having a film composition of $Co_2Mn_{0.73}Fe_{0.67}Si_{0.84}$. 23

Fig. 2.5. Schematic diagram showing the regions of the SSFU composition types I to IV in the δ−β plane with $\delta = \alpha' + \beta'$ for $Co_2Mn_{\alpha'}Fe_{\beta'}Si_{\beta}$ with the restrictions of $0 < \delta < 2$ and $0 < \beta < 2$ [36]. 27

Fig. 2.6. Schematic diagram of MTJ layer structure grown on a MgO(001) single-crystal substrate..... 28

Fig. 2.7. High-resolution Z-contrast scanning TEM (STEM) image of a $Co_{50}Fe_{50}$ (CoFe)-buffered Co_2(Mn,Fe)Si (CMFS) MTJ layer structure. 30

Fig. 2.8. Two-beam bright-field TEM image of a CoFe-buffered CMFS MTJ layer structure with (Mn+Fe)-rich $Co_2Mn_{1.24}Fe_{0.16}Si_{0.84}$ electrodes. 32

Fig. 2.9. Typical dependence of R_PA, R_{AP}A, and TMR ratio on MgO barrier thickness (t_{MgO}) at 290 K for CMFS MTJs with $Co_2Mn_{1.24}Fe_{0.16}Si_{0.84}$ electrodes fabricated on a 20 x 20 mm^2 MgO(001) substrate..... 33

Fig. 3.1. (Mn+Fe) film composition dependence of the experimental saturation magnetization of series-A CMFS films at 10 K. 37

Fig. 3.2. Spin-projected LDOS per atom for (a) ordinary-site Mn ($Mn_{Mn/Fe}$), (b) ordinary-site Fe ($Fe_{Mn/Fe}$), (c) ordinary-site Co (Co_{Co}), and (d) $Co_{Mn/Fe}$ antisites for series-A CMFS ($Co_2Mn_{0.73}Fe_{\beta'}Si_{0.84}$)..... 39

Fig. 3.3. Spin-projected total DOS per formula unit for series-A CMFS, or $Co_2Mn_{0.73}Fe_{\beta'}Si_{0.84}$ with a fixed α' of 0.73 in $Co_2Mn_{\alpha'}Fe_{\beta'}Si_{0.84}$ and various β' ranging from 0 to 0.67. 40

Fig. 3.4. Theoretically calculated local spin magnetic moments per atom, m_{spin}, for Mn, Fe and Co at the nominal Mn/Fe site ($Mn_{Mn/Fe}$, $Fe_{Mn/Fe}$, and $Co_{Mn/Fe}$). 41

Fig. 3.5. Experimental tunneling spin polarizations, P_{exp}, deduced from the TMR ratio at 4.2 K using a modified Julliere model and two kinds of theoretical spin polarizations, $P_{th}(sp)$ and $P_{th}(spd)$, obtained by the KKR-CPA calculations as a function of $\delta = \alpha'+\beta'$ with $\alpha' = 0.73$ for series-A CMFS..... 45

Fig. 4.1. The (Mn+Fe) film composition dependence of the experimental saturation magnetization of series-B CMFS films at 10 K..... 49

Fig. 4.2. Spin-projected total DOS per formula unit for series-B CMFS, or $Co_2Mn_{\alpha'}Fe_{\beta'}Si_{0.84}$ with a fixed $\delta = \alpha'+\beta' = 1.40$ and various α' and β' ranging from $\alpha' = 0.73$ ($\beta' = 0.67$) to $\alpha' = 1.40$ ($\beta' = 0$). 50

Fig. 4.3. Experimental spin polarizations, P_{exp}, deduced from the TMR ratio at 4.2 K using a modified Julliere model and two kinds of theoretical spin polarizations, $P_{th}(sp)$ and $P_{th}(spd)$, obtained by the KKR-CPA calculations as a function of β' with $\alpha'+\beta' = 1.40$ for series-B CMFS..... 51

Fig. 4.4. TMR ratios at (a) 4.2 K and (b) 290 K for CMFS MTJs as a function of $\delta = \alpha'+\beta'$ in $Co_2Mn_{\alpha'}Fe_{\beta'}Si_{0.84}$ electrodes with $\beta' = 0.16$ ranging from 1.30 ($\alpha' = 1.14$) to 1.40 ($\alpha' = 1.24$). 54

Fig. 4.5. Bias voltage dependences of the normalized differential conductances of $Co_2Mn_{1.24}Fe_{0.16}Si_{0.84}$/MgO/ $Co_2Mn_{1.24}Fe_{0.16}Si_{0.84}$ MTJ showing characteristic voltages, V_{c1} and V_{c2} for (a) parallel and (b) antiparallel magnetization configurations. 57

Fig. 4.6. Bias voltage dependence of the second derivative, d^2I/dV^2, of $Co_2Mn_{1.24}Fe_{0.16}Si_{0.84}$/MgO/ $Co_2Mn_{1.24}Fe_{0.16}Si_{0.84}$ MTJ. 59

Fig. 4.7. Possible tunneling paths assumed during the parallel magnetization configuration for (a) a positive applied bias voltage (b) a negative applied bias voltage. 60

Fig. 4.8. Possible tunneling paths assumed during the antiparallel magnetization configuration for (a) a positive applied bias voltage (b) a negative applied bias voltage. 60

Fig. 4.9. Theoretically calculated spin-projected total DOS per formula unit for a CMFS film having a Mn-composition, α', of $\alpha' = 1.24$ and Fe-composition, β', of $\beta' = 0.16$ ($Co_2Mn_{1.24}Fe_{0.16}Si_{0.84}$). 62

Fig. 5.1. Normalized differential conductance, $G_N(V) = (dI/dV)/(dI/dV)\,|\,V=0$, as a function of the applied bias voltage for $Co_2Mn_{0.73}Fe_{0.62}Si_{0.84}$/MgO/ $Co_2Mn_{0.73}Fe_{0.62}Si_{0.84}$ MTJ showing a high TMR ratio. 67

Fig. 5.2. The bias voltage dependence of the TMR ratio of $Co_2Mn_{0.73}Fe_{0.62}Si_{0.84}$/MgO/$Co_2Mn_{0.73}Fe_{0.62}Si_{0.84}$ MTJ experimentally obtained at 4.2 K. 68

Fig. 5.3. Comparison of the bias voltage dependence of the normalized differential conductance for the antiparallel configuration of $Co_2Mn_{\alpha'}Fe_{\beta'}Si_{0.84}$/MgO/$Co_2Mn_{\alpha'}Fe_{\beta'}Si_{0.84}$MTJs..... 69

Fig. 5.4. The dependence of the normalized antiparallel conductance at the characteristics voltage, Vs, on $1/\xi$ (= TMR (4.2 K) + 1), of $Co_2Mn_{\alpha'}Fe_{\beta'}Si_{0.84}$/MgO/ $Co_2Mn_{\alpha'}Fe_{\beta'}Si_{0.84}$. 76

List of Tables

Table I. Site-specific formula unit (SSFU) compositions given by the antisite-based SSFU composition model for $Co_2Mn_{\alpha'}Fe_{\beta'}Si_{0.84}$ with a fixed value of α' = 0.73. 12

Table II. SSFU compositions given by the antisite-based SSFU composition model for $Co_2Mn_{\alpha'}Fe_{\beta'}Si_{0.84}$ with a fixed value of $\delta = \alpha'+\beta'$ = 1.40. 13

Table III. Film compositions expressed as $Co_2Mn_{\alpha'}Fe_{\beta'}Si_{\beta}$, site-specific formula unit (SSFU) composition types, SSFU compositions, measured in-plane (a) and out-of-plane (c) lattice constants, and Z_t-24 values of series-A CMFS films. 18

Table IV. Film compositions expressed as $Co_2Mn_{\alpha'}Fe_{\beta'}Si_{\beta}$, SSFU compositions, measured lattice constants *a* and *c*, and Z_t-24 values of series-B CMFS films. 19

Table V. Film compositions expressed as $Co_2Mn_{\alpha'}Fe_{\beta'}Si_{\beta}$, SSFU composition types, SSFU compositions, measured lattice constants *a* and *c*, and Z_t-24 values of series-C CMFS films. 23

Table VI. General expressions for SSFU compositions of $Co_2Mn_{\alpha'}Fe_{\beta'}Si_{\beta}$, from type I to type IV for $0 < \delta < 2$ and $0 < \beta < 2$; where, $\delta = \alpha'+\beta'$ and $\xi = \beta'/(\alpha'+\beta')$. 25

Table VII. Values of the half-metal gap, E_g, of $Co_2Mn_{1.24}Fe_{0.16}Si_{0.84}$ upper and lower electrodes (UE and LE) obtained experimentally and the relative position of E_F in the half-metal gap, E_v/E_g for the upper and lower electrodes. 61

Table VIII. Film composition expressed as $Co_2Mn_{\alpha'}Fe_{\beta'}Si_{0.84}$, Fe composition, β', in $Co_2Mn_{0.73}Fe_{\beta'}Si_{0.84}$ and TMR ratio at 4.2 K of $Co_2Mn_{0.73}Fe_{\beta'}Si_{0.84}$ /MgO/ $Co_2Mn_{0.73}Fe_{\beta'}Si_{0.84}$ MTJs 69

Chapter 1

Introduction

In this chapter, first, we will discuss the general background related to the research conducted in this dissertation. Then, a review of the important experimental and theoretical backgrounds related to this study will be made. Furthermore, a detailed discussion on the results of the experimental investigation of the influence of film composition on the tunneling magnetoresistance characteristics of fully expitaxial Co_2(Mn,Fe)Si-based MTJs will be given. Finally, the purpose and approaches of this dissertation will be stated.

1.1. Spintronic devices and their applications

Today's electronics industry is advancing at an alarming rate and novel technologies are being introduced. Nowadays, many advanced electronic devices are replacing conventional ones and are being implemented in a wide variety of applications. The advancement of the electronic memory (data storage) technology is a best example for the advancement of the electronic industry. The electronic memory technology is evolving very fast starting from the semiconductor memory which first replaced the magnetic core ferrite memory in 1970s [1]. Currently, we find static random access memory (SRAM), dynamic random access memory (DRAM), flash memory, hard disk drive (HDD) and other similar memory devices widely incorporated in different electronic devices. However, many researchers in academia and industry are still working hard to invent a novel memory device which at the same time incorporates the best features of all the memory devices which are mentioned before (i.e. a memory device with a large capacity (density), fast write/read capabilities, infinite endurance, nonvolatility, smaller size, low power consumption and so on). On the other hand, realizing a memory device with those functionalities by relying on the traditional charge-based electronic technology is becoming almost impossible. Therefore, it is compulsory to resort to a new field of electronics in order to further continue the technological advancements in this industry.

One such novel area of electronics which utilizes the spin-degree of freedom of an electron, in addition to its charge, is called spin electronics (or spintronics in short). Electronic devices which work based on the concept of spintronics are called spin-dependent devices. They have been extensively studied as potential candidates for electronic devices because they are expected to provide nonvolatility, reconfigurable logic functionalities, and ultralow power consumption [2,3]. Thus, spintronic devices are highly promising as future-generation electronic devices.

Spintronic devices are being implemented in many applications such as in memory devices (in magnetic random access memories (MRAMs) and HDDs), for application to sensors and so on. Among these devices, magnetic tunnel junctions (MTJs) and giant magnetoresistance (GMR) devices are the main candidates. They find many applications in magnetic field sensors, MRAMs, as read heads of HDDs, galvanic isolators and so on [3].

1.2. Operation principle of MTJs

Figure 1.1 shows a schematic diagram of the first MRAM product from Freescale Inc. which has MTJs as storage elements. As shown in this figure, MTJs are incorporated as the main storage components in the modern MRAM cells.

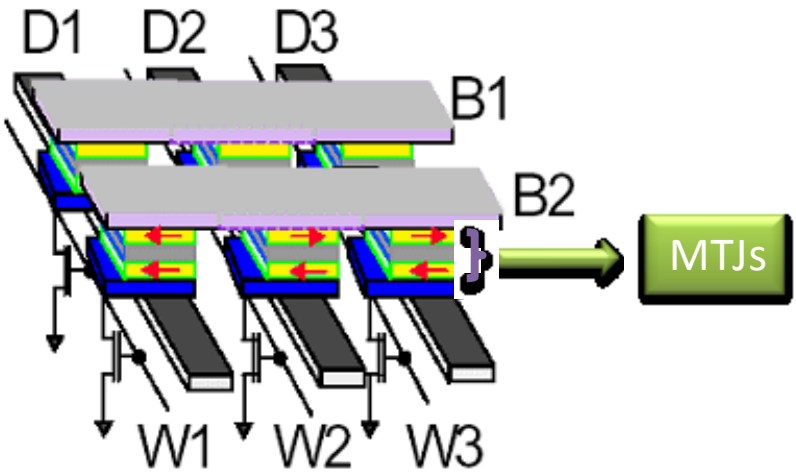

Fig. 1.1. A schematic diagram of the first MRAM product from Freescale Inc. with a 4M bit capacity having an MTJ as a memory element.

The basic schematic structure of an MTJ is shown in Fig. 1.2. It has two ferromagnetic electrodes (called upper and lower electrodes) separated by an insulating tunnel barrier. The basic operation of MTJs is that when the magnetization orientations of the upper and lower ferromagnetic electrodes are aligned parallel, the direction of the majority spins in the lower electrode (emitter electrode) will be parallel to that of the upper electrode (collector electrode). Furthermore, the direction of the minority spins in the lower electrode will be parallel to that in the upper electrode. Thus, because the spin of the tunneling electrode is conserved, the electrons in the majority-spin band of the emitter electrode tunnel into the majority spin band of the collector electrode. Similarly, the electrons in the minority-spin band of the emitter electrode tunnel to the minority-spin band of the collector electrode, as shown in Fig. 1.3 (a). Therefore, the resistance during the parallel magnetization alignment of the electrodes becomes very low and thus the tunneling current will be high. On the other hand, when the magnetization orientations of the two ferromagnets are aligned antiparallel, the direction of the majority spins in the lower electrode is antiparallel to that in the upper electrode. Furthermore, the direction of the minority spins in the lower electrode is antiparallel to that in the upper electrode, as shown in Fig. 1.3 (b). Thus, because of the conservation of the spin of the tunneling electron, the electrons in the majority-spin band of the emitter electrode tunnel to the minority-spin band of the collector electrode. Similarly, the electrons in the minority-spin band of the emitter electrode tunnel to the majority-spin band of the collector electrode. Therefore, during the antiparallel alignment of the ferromagnetic layers, the resistance becomes much higher and thus the tunneling current will be low. The basic spin-dependent tunneling mechanism in MTJs for parallel (Fig. 1.3 (a)) and antiparallel (Fig. 1.3 (b)) magnetization alignments of the upper and lower ferromagnetic electrodes is shown by a simple schematic in Fig. 1.3. Thus, depending on the magnetization orientation of the two ferromagnets, the device will attain either an ON (1) or OFF (0) state. Note that one of the electrodes of an MTJ is magnetically pinned and the other is free to rotate with the external magnetic field. Hence, electronic memory devices based on an MTJ store binary data (0, 1) as the orientation of the magnetization in the free layer, which may be parallel or antiparallel to the pinned layer as described above [1].

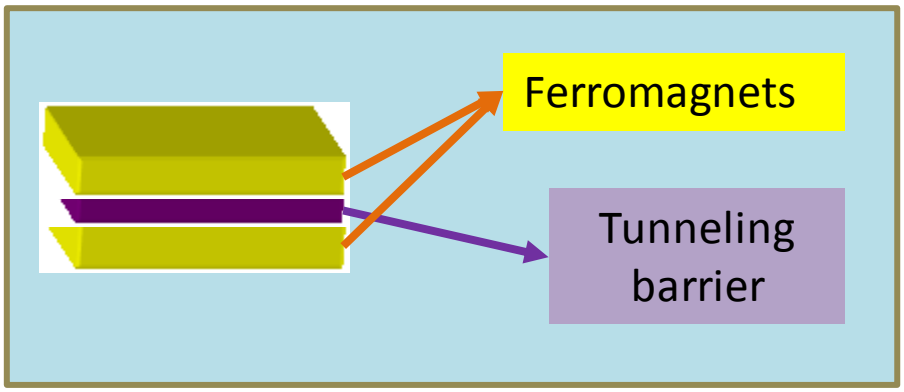

Fig. 1.2. A schematic diagram of the structure of a magnetic tunnel junction (MTJ). It has two ferromagnetic electrodes (upper and lower electrodes) separated by a tunneling barrier.

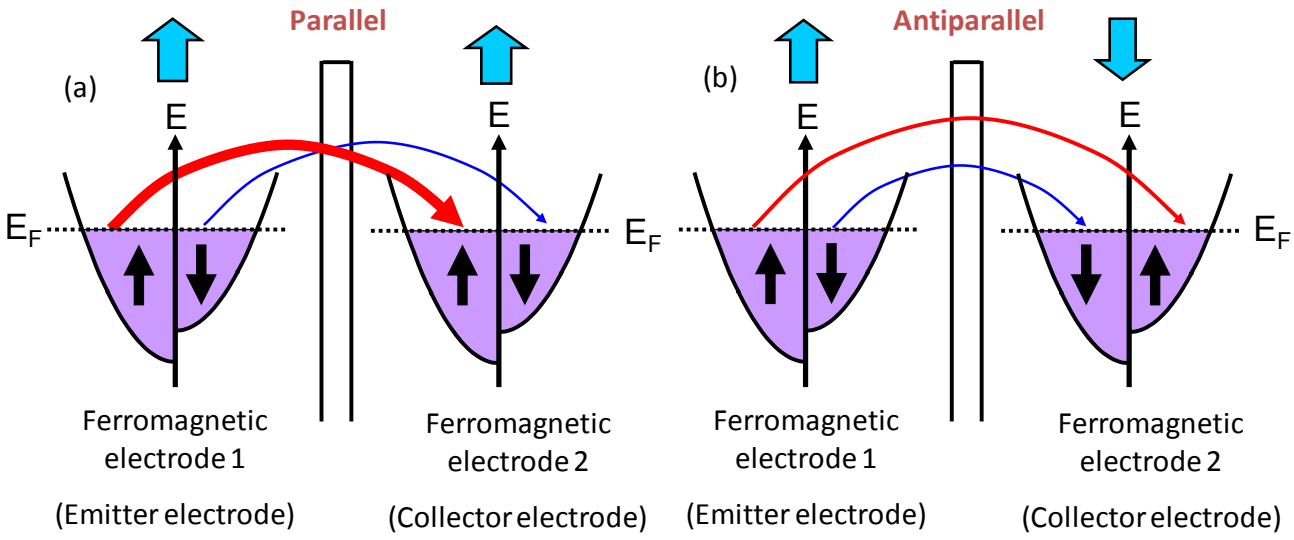

Fig. 1.3. A schematic diagram showing the basic spin-dependent tunneling mechanism occurring in MTJs for (a) parallel (b) antiparallel magnetization alignments of the upper (emitter) and lower (collector) electrodes.

A parameter which quantifies the difference in the parallel and antiparallel resistance (conductance) in MTJs is called the tunneling magnetoresistance (TMR) ratio. It is one of the figures of merit of an MTJ and is defined as the quotient of the difference in the antiparallel and parallel resistances to the parallel resistance as given by equation 1.1. It is a key parameter because, for example, it determines the maximum available read signal

from an MTJ [1]. Thus, the higher the TMR ratio, the higher is the read signal and thus the better is the performance and reliability of the memory device.

Therefore, it is very important to continuously improve the TMR ratio of MTJs in order to fully utilize the capabilities of these devices and to readily apply them in future generation electronic devices. One of the major techniques to improve the TMR ratio of MTJs is the selection of ferromagnetic materials with high spin polarizations. A ferromagnetic material which has a high spin polarization enhances the TMR ratio. On the other hand, a high quality, single crystalline tunneling barrier is proved to further improve the TMR ratios of MTJs through coherent tunneling [4−7] along with using ferromagnetic electrodes with high spin polarization.

$$\text{TMR ratio} = \frac{R_{AP} - R_P}{R_P} \qquad (1.1)$$

1.3. MTJs with half-metallic ferromagnetic electrodes

Originating from the existence of an energy gap for one spin direction (for minority or majority-spin band), as initially predicted by de Groot et al. in 1983 [8], half-metallic ferromagenets (HMFs) are characterized by a complete spin polarization at the Fermi energy (E_F), making them the most promising ferromagnetic materials to be applied to spintronic devices. Most Heusler alloys are predicted to have a half-metallic ferromagnetic nature featuring a band structure in which the minority-spin density of states (DOS) is semiconducting while that of the majority is metallic. In particular, Co-based full-Heusler alloys (Co_2YZ, where Y is usually a transition metal and Z is a main group element) are predicted to possess those peculiar properties [9] which make them promising candidates to be employed in the next generation spintronic devices. They are extensively applied to spintronics devices, including MTJs, in particular those with MgO barrier [10−17], and GMR devices [18−23], and to spin injection into semiconductors [24−30]. This is due to the theoretically predicted half-metallicity for many of them [31−33] and a high Curie temperature (T_c), which is well above room temperature (RT) [34]. Figure 1.4 shows a simple schematic of the spin-resolved DOS of a half-metallic Heusler alloy. As shown in this figure, there are states at the E_F for the majority-spin DOS

where as there are no states available at the E_F for the minority-spin state. Thus, ideally, these materials possess a 100% spin polarization at the E_F, where the spin polarization, P, is defined in terms of the majority- and minority-spin density of states at E_F, ρ_M and ρ_m respectively, as shown in Eq. (1.2).

$$P = \frac{\rho_M - \rho_m}{\rho_M + \rho_m} \qquad (1.2)$$

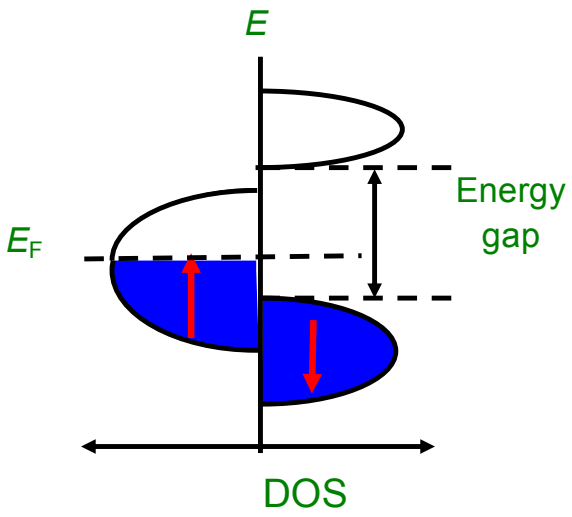

Fig. 1.4. A schematic diagram showing the spin-resolved density of states (DOS) of a half-metallic Heusler alloy. The up-spin state (shown by up arrow) displays a metallic band structure while the down-spin state (shown by down arrow) shows semiconducting band structure.

In practice, off-stoichiometry in Co_2YZ thin films prepared by magnetron sputtering or molecular beam epitaxy is inevitable and leads to the destruction of the ideal half-metallic electronic structure described above. If the minority-spin in-gap states are introduced at E_F by a structural defect for a half-metallic or nearly half-metallic film, the half-metallicity is strongly degraded. Here, experiments and first-principles calculations have identified harmful defects affecting the half-metallicity of Co_2MnSi (CMS) and Co_2MnGe (CMG), i.e., Co antisites at nominal Mn sites (Co_{Mn} antisites) [13,35,36]. The effect of these antisites has been studied in terms of TMR ratio [13−15,36], saturation magnetization per formula unit [13,36], and surface spin polarization [37]. Moreover, the electronic states of off-stoichiometric CMS and CMG films have been investigated by

high-energy x-ray photoelectron spectroscopy [38−40], and the magnetic states have been investigated by x-ray absorption spectroscopy and x-ray circular dichroism [41−43].

Picozzi at al. [35] theoretically predicted that Co_{Mn} antisites in CMS and CMG, where a Mn site is replaced by a Co atom, cause minority-spin in-gap states at E_F and thus are detrimental to the half-metallicity of CMS and CMG. Figure 1.5 shows the spin resolved total DOS for a disorder between Mn and Si in CMS (Fig. 1.5 (a)) and for disorder between Co and Mn sites (1.5 (b)). As shown in Fig. 1.5, a disorder between Mn and Si sites doesn't affect the half-metallicity of CMS Heusler alloys whereas a disorder between Co and Mn sites destroys the half-metallicity by introducing in-gap states at E_F in the minority-spin states as explained above. Similarly, Miura et al. [44] theoretically predicted that a disorder between Co site and Cr site in Co_2CrAl leads to a significant reduction in the spin polarization at E_F, while a disorder between Cr site and Al site does not significantly decrease the spin polarization.

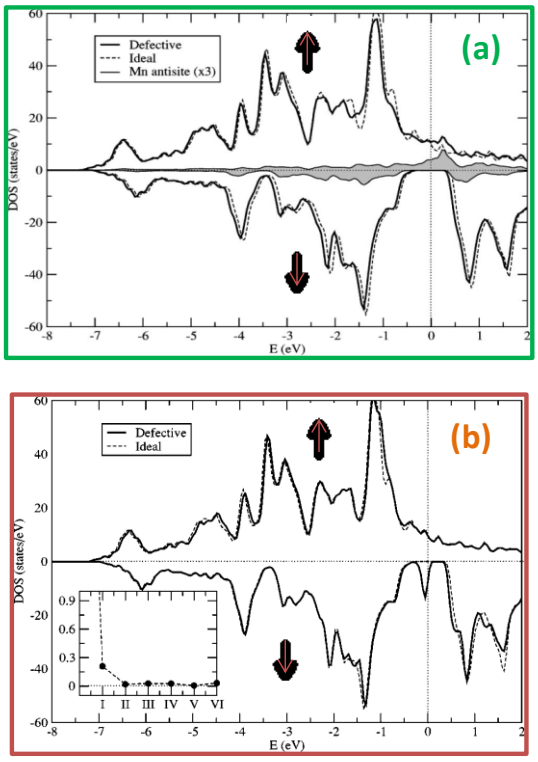

Fig. 1.5. Theoretically calculated spin-resolved total density of states (DOS) of half-metallic Co_2MnSi Heusler alloy calculated for a disorder between (a) Mn and Si sites (b) Co and Mn sites (antisite Co atom at the nominal Mn site) [35].

On the other hand, Julliere's model [45] predicted that the TMR ratio of MTJs depends merely on the spin polarization of the electrodes. Thus the TMR ratio of the MTJs is directly related to the spin polarization, P, of the ferromagnetic electrodes as shown by Eq. 1.3. Even though, later, it was shown that the crystalline quality of insulating tunnel barrier also affects the TMR ratio (by a coherent tunneling process [4−7]), the contribution of the spin polarization of the electrodes to the TMR ratio is still significant. Thus, by preparing MTJs with highly spin polarized electrode materials, it is possible to achieve giant TMR ratios.

$$\text{TMR ratio} = \frac{2P_1P_2}{1 - P_1P_2} \qquad (1.3)$$

Hence, experimental investigation of the half-metallicity of Heusler alloys are being done by preparing MTJs with Heusler alloy electrodes and studying their TMR characteristics. Ishikawa et al.[46] from our research group did an investigation of the Mn-film composition (α) dependence of the TMR ratio for MTJs having CMS upper and lower electrodes with various values of α in $Co_2Mn_\alpha Si$ which was grown on an MgO-buffer layer and having an MgO-tunneling barrier. MTJs with Mn-rich CMS electrodes showed TMR ratios, up to 1135% at 4.2 K and 236% at RT for $\alpha = 1.29$, exceeding those of MTJs with CMS electrodes having an almost stoichiometric composition. On the other hand, by introducing a CoFe as a buffer layer and a thin CMS as upper and lower electrode, Liu et al. [14,15] from our research group reported high TMR ratios of 1995% at 4.2 K and 354 % at 290 K for fully epitaxial CMS/MgO/CMS MTJs. The improvement of the TMR ratio for a CMS MTJ with CoFe-buffered CMS electrode as compared to that of an MgO-buffered one is due to the enhanced contribution of coherent tunneling originating from the increased misfit dislocation spacing at the lower and upper interfaces with a MgO barrier along with the half-metallicity of CMS electrodes [14,15]. Thus, markedly high TMR ratios were demonstrated by utilizing the half-metallicity of the CMS electrode and coherent tunneling effect. These results also demonstrated that a wide range of Mn-rich CMS films retain half-metallicity in terms of their Mn composition, which is also favorable for applying Co_2YZ thin films to spintronics devices.

Moreover, H. Liu et al. [47] recently investigated the influence of varying the film composition of a $Co_2(Mn,Fe)Si$ (CMFS) Heusler alloy on the TMR characteristics of fully epitaxial CMFS/MgO/CMFS MTJs (CMFS MTJs) with $Co_2Mn_{\alpha'}Fe_{\beta'}Si_{0.84}$ electrodes. Through this study, we demonstrated giant TMR ratios of 2610% at 4.2 K and 429% at 290 K for the MTJ with Mn-rich, lightly Fe-doped CMFS electrodes. In section 1.4, we will describe the main results of the experimental investigation on the influence of film composition on the TMR characteristics of fully epitaxial CMFS MTJs and discuss the origin of the film composition dependence.

1.4. Influence of film composition on the TMR characteristics of CMFS MTJs

In this section, the main results of the experimental investigation of the influence of Mn and Fe film compositions on the half-metallic character of quaternary Heusler alloy CMFS and the origins of the influence of film compositions will be given.

In Ref. [47], H. Liu et al. reported the influence of film composition on the half-metallic character of quaternary Heusler alloy thin films of CMFS by studying the composition dependence of the TMR ratio of fully epitaxial CMFS MTJs having $Co_2Mn_{\alpha'}Fe_{\beta'}Si_{0.84}$ electrodes with various Mn and Fe compositions. Two series of MTJs were investigated, series-A and series-B CMFS MTJs. In series-A CMFS MTJs the Mn-composition, α', in $Co_2Mn_{\alpha'}Fe_{\beta'}Si_{0.84}$ was fixed to 0.73 while the Fe-composition, β', was varied from 0 to 0.67. Whereas in series-B CMFS MTJs both α' and β' were varied while fixing their sum, δ, to 1.40. Figures 1.6 (a) and (b) plot the TMR ratios at 4.2 K and 290 K, respectively, of series-A CMFS MTJs, as a function of $\delta = \alpha' + \beta'$, with δ ranging from 0.73 ($\beta' = 0$) to 1.40 ($\beta' = 0.67$) while keeping α' fixed at 0.73.

The TMR ratio of the series-A CMFS MTJs increased with increasing δ, going from 1360% at 4.2 K and 300% at 290 K for $\delta = 1.0$ ($Co_2Mn_{0.73}Fe_{0.27}Si_{0.84}$) to 1700% at 4.2 K and 368% at 290 K for $\delta = 1.35$ ($Co_2Mn_{0.73}Fe_{0.62}Si_{0.84}$). It then decreased to 1290% at 4.2 K and 285% at 290 K for the δ-rich composition of $\delta = 1.40$ ($Co_2Mn_{0.73}Fe_{0.67}Si_{0.84}$).

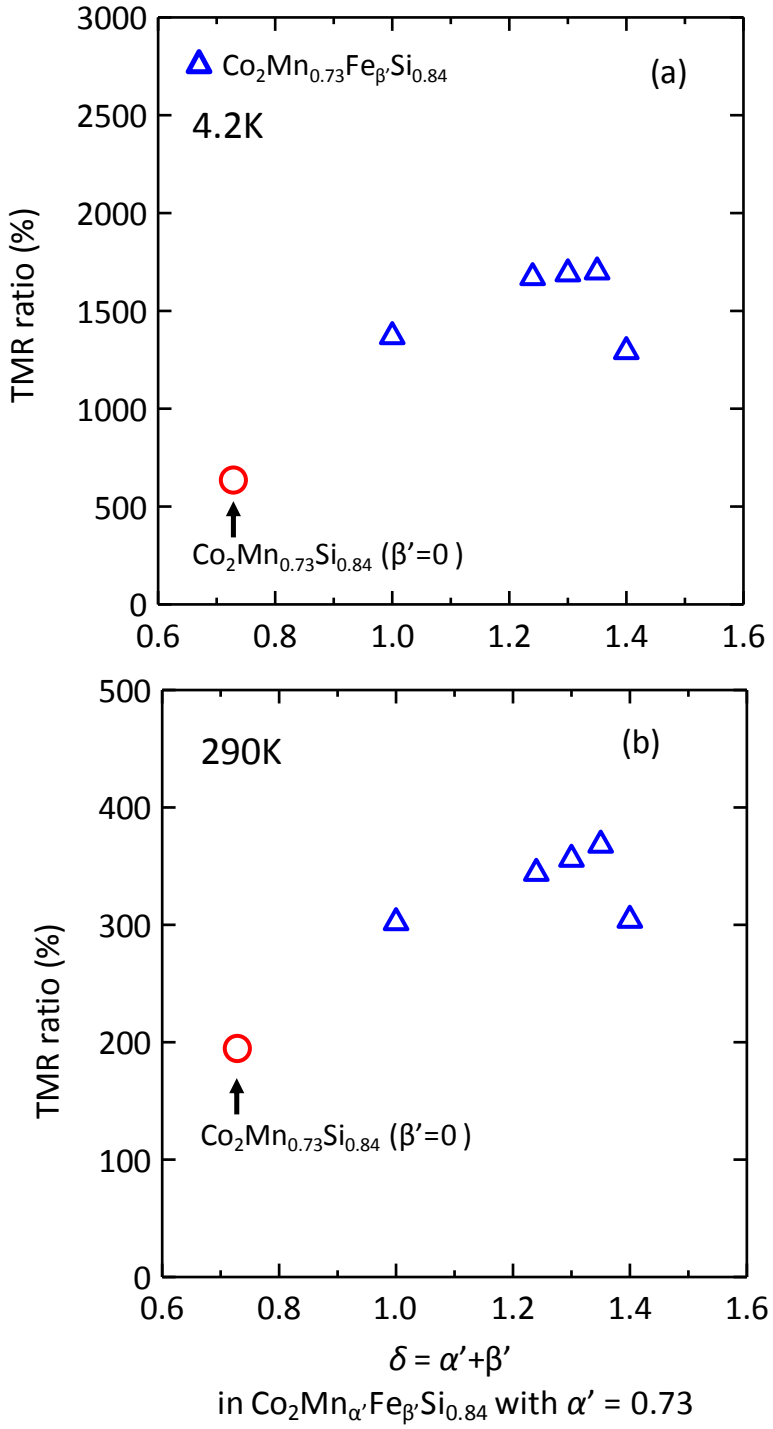

Fig. 1.6. TMR ratios at (a) 4.2 K and (b) 290 K for CMFS/MgO/CMFS MTJs (CMFS MTJs) as a function of (Mn + Fe) composition, $\delta = \alpha' + \beta'$, ranging from 0.73 ($\beta' = 0$) to 1.40 ($\beta' = 0.67$) with a constant $\alpha' = 0.73$ in $Co_2Mn_{\alpha'}Fe_{\beta'}Si_{0.84}$ electrodes (CMFS MTJ of series A). The $\delta = 0.73$ ($\beta' = 0$) MTJ corresponds to the $Co_2Mn_{0.73}Si_{0.84}$ MTJ (open red circle) [47].

Now, it is important to first discuss about the site-specific formula unit (SSFU) composition model in order to explain the observed experimental features of the influence of film composition on the TMR characteristics of CMFS MTJs discussed above. An antisite-based SSFU composition model was devised for the quaternary Heusler alloy CMFS on the basis of the antisite-based SSFU composition model developed for ternary Heusler alloy CMS [36], by assuming that the Mn to Fe ratio is constant for all nominal Mn/Fe, Si, and Co sites. The detail explanation of the SSFU composition model will be given in the experimental and computational methods (in chapter 2). Here it will be briefly described for the sake of explaining the experimental results presented in this section. The nominal SSFU compositions for series-A CMFS films are listed in Table I, along with (1) the Fe ratio ξ with respect to the total (Mn+Fe) concentration $\delta = \alpha' + \beta'$, i.e., $\xi = \beta'/\delta$, (2) Z_t–24, where Z_t is the valence electron number per formula unit, and (3) the occupation ratio of antisite Co at the nominal Mn/Fe site, γ_a. The Z_t−24 values for off-stoichiometric quaternary CMFS films in this study are those given by the antisite-based SSFU composition model. Note, however, that the same values can also be obtained by assuming that each formula unit contains four atoms along with antisites, not vacant sites, to accommodate off-stoichiometry. In other words, the antisite-based SSFU composition model and the antisite-based, but not site-specific formula unit model are equivalent in terms of Z_t−24.

Table I. Site-specific formula unit (SSFU) compositions given by the antisite-based SSFU composition model for $Co_2Mn_{\alpha'}Fe_{\beta'}Si_{0.84}$ with a fixed value of $\alpha' = 0.73$ used in the CMFS MTJs of series A together with the Fe ratio ξ with respect to the total (Mn+Fe) concentration $\delta = \alpha'+\beta'$, i.e., $\xi = \beta'/\delta$, Z_t–24, where Z_t is the valence electron number per formula unit, and the occupation ratio of antisite Co at the nominal Mn/Fe site, γ_a. The SSFU composition type II is $Co_2[(Mn_{1-\xi}Fe_\xi)_{1-x}Co_x][Si_{1-y}(Mn_{1-\xi}Fe_\xi)_y]$, where the second and third brackets represent the nominal Mn/Fe and Si sites, and the type III is $[Co_{2-x}(Mn_{1-\xi}Fe_\xi)_x][Mn_{1-\xi}Fe_\xi][Si_{1-y}(Mn_{1-\xi}Fe_\xi)_y]$, where the first, second and third brackets represent the nominal Co, Mn/Fe and Si sites [36, 47].

Film composition expressed as $Co_2Mn_{\alpha'}Fe_{\beta'}Si_\beta$ ($\alpha' = 0.73$, $\beta = 0.84$)	β' in $Co_2Mn_{0.73}Fe_{\beta'}Si_{0.84}$ and $\delta = \alpha' + \beta'$		SSFU composition type No.	SSFU composition in type II or type III			γ_a	Z_t–24
	β'	$\delta = \alpha' + \beta'$		ξ	x	y		
$Co_2Mn_{0.73}Si_{0.84}$	0	0.73	II	0	0.24	0.06	0.24	5.66
$Co_2Mn_{0.73}Fe_{0.27}Si_{0.84}$	0.27	1.00	II	0.27	0.083	0.13	0.083	5.82
$Co_2Mn_{0.73}Fe_{0.51}Si_{0.84}$	0.51	1.24	III	0.41	0.039	0.18	0	5.95
$Co_2Mn_{0.73}Fe_{0.57}Si_{0.84}$	0.57	1.30	III	0.44	0.068	0.19	0	5.98
$Co_2Mn_{0.73}Fe_{0.62}Si_{0.84}$	0.62	1.35	III	0.46	0.091	0.20	0	6.00
$Co_2Mn_{0.73}Fe_{0.67}Si_{0.84}$	0.67	1.40	III	0.48	0.11	0.21	0	6.03

The SSFU composition type for β' from 0 to 0.27 is $Co_2[(Mn_{1-\xi}Fe_\xi)_{1-x}Co_x][Si_{1-y}(Mn_{1-\xi}Fe_\xi)_y]$; this is called type II as reported in Ref. 36, where the first and second brackets represent the nominal Mn/Fe and Si sites. Type II features antisite Co at the nominal Mn/Fe site. On the other hand, the SSFU composition type for β' from 0.51 to 0.67 is $[Co_{2-x}(Mn_{1-\xi}Fe_\xi)_x][Mn_{1-\xi}Fe_\xi][Si_{1-y}(Mn_{1-\xi}Fe_\xi)_y]$; this is called type III in Ref. 36, where the first, second, and third brackets represent the nominal Co, Mn/Fe and Si sites. In contrast to type II, no antisite Co atom at the nominal Mn/Fe site ($Co_{Mn/Fe}$ antisites) is present in type III. More generally, the SSFU composition of $Co_2(Mn_{1-\xi}Fe_\xi)_\delta Si_\beta$ belongs to type II (type III) for $\delta < 2-\beta$ ($\delta > 2-\beta$) [36] by assuming that the Mn to Fe ratio is constant for all the nominal Mn/Fe, Si, and Co sites.

Now let us discuss the origin of the observed dependence of the TMR ratio on δ of series-A CMFS MTJs on the basis of the SSFU composition model. The increase in the TMR ratio with increasing δ (through β') from $\delta = 0.73$ ($\beta' = 0$) to $\delta = 1.24$ ($\beta' = 0.51$) corresponds to a decrease in γ_a in the SSFU composition from $\gamma_a = 0.24$ for $\delta = 0.73$ ($Co_2Mn_{0.73}Si_{0.84}$) to $\gamma_a = 0$ for $\delta = 1.24$ ($Co_2Mn_{0.73}Fe_{0.51}Si_{0.84}$). Thus, we anticipate that the observed increase in the TMR ratios for this δ range can be ascribed to the suppression of $Co_{Mn/Fe}$ antisites, based on the results obtained for CMS MTJs [36].

Next, we discuss the origin of the increase in the TMR ratio for the δ range from 1.24 to 1.35, where no $Co_{Mn/Fe}$ antisite is present ($\gamma_a = 0$) in the SFFU composition model. The increase suggests that there is a slight difference between γ_a in the films prepared by sputtering under non-equilibrium conditions and the nominal γ_a given by the SSFU composition model. The increase in the TMR ratio in the δ range from 1.24 to 1.35 can then be ascribed to a further decrease in residual $Co_{Mn/Fe}$ antisites in the films. In summary, the dependence of the TMR ratio on δ of the series-A CMFS MTJs with δ ranging from 0.73 (β' = 0) to 1.35 (β' = 0.62) is close to that for CMS/MgO/CMS MTJs (CMS MTJs) with $Co_2Mn_\alpha Si$ electrodes on the value of α [11,13−15].

Now let's discuss the influence of film composition on the TMR ratios of CMFS/MgO-based MTJs as a function of Fe composition for a fixed (Mn+Fe) composition, series-B CMFS MTJs. Because it was revealed that high tunnelling spin polarizations, *i.e.*, high TMR ratios, are obtained for CMFS MTJs with (Mn+Fe)-rich compositions, we further investigated the α' and β' dependences of the TMR ratios in the δ-rich composition region in order to clarify the factors that determine the half-metallic character. In particular, we varied the Fe ratio of δ-rich electrodes while keeping δ constant (δ=1.40; series-B CMFS). The film compositions and corresponding SSFU compositions for series B are shown in Table II, along with ξ, Z_t–24, and γ_a.

Table II. SSFU compositions given by the antisite-based SSFU composition model for $Co_2Mn_{\alpha'}Fe_{\beta'}Si_{0.84}$ with a fixed value of $\delta = \alpha' + \beta' = 1.40$. used in CMFS MTJs of series B along with $\xi = \beta'/\delta$, Z_t–24, and γ_a. The SSFU composition type III is $[Co_{2-x}(Mn_{1-\xi}Fe_\xi)_x][Mn_{1-\xi}Fe_\xi][Si_{1-y}(Mn_{1-\xi}Fe_\xi)_y]$, where the first, second and third brackets represent the nominal Co, Mn/Fe and Si sites [36, 47].

Film composition expressed as $Co_2Mn_{\alpha'}Fe_{\beta'}Si_\beta$ ($\delta = \alpha' + \beta' = 1.40$, $\beta = 0.84$)	α' and β' in $Co_2Mn_{\alpha'}Fe_{\beta'}Si_{0.84}$ with $\delta = \alpha' + \beta' = 1.40$		SSFU composition type No.	SSFU composition in type III			γ_a	Z_t−24
	α'	β'		ξ	x	y		
$Co_2Mn_{1.40}Si_{0.84}$	1.40	0	III	0	0.11	0.21	0	5.40
$Co_2Mn_{1.35}Fe_{0.05}Si_{0.84}$	1.35	0.05	III	0.036	0.11	0.21	0	5.44
$Co_2Mn_{1.30}Fe_{0.10}Si_{0.84}$	1.30	0.10	III	0.071	0.11	0.21	0	5.49
$Co_2Mn_{1.24}Fe_{0.16}Si_{0.84}$	1.24	0.16	III	0.11	0.11	0.21	0	5.55
$Co_2Mn_{1.16}Fe_{0.24}Si_{0.84}$	1.16	0.24	III	0.17	0.11	0.21	0	5.62
$Co_2Mn_{1.00}Fe_{0.40}Si_{0.84}$	1.00	0.40	III	0.29	0.11	0.21	0	5.77
$Co_2Mn_{0.85}Fe_{0.55}Si_{0.84}$	0.85	0.55	III	0.39	0.11	0.21	0	5.92
$Co_2Mn_{0.73}Fe_{0.67}Si_{0.84}$	0.73	0.67	III	0.48	0.11	0.21	0	6.03

Note that Z_t–24 increased linearly with β' for series-B CMFS characterized by a constant δ from Z_t–24 = 5.40 for β'= 0 to Z_t–24 = 6.03 for β' = 0.67. Figures 1.7 (a) and (b) plot the TMR ratios at 4.2 K and 290 K, respectively, for series-B CMFS MTJs as a function of β' ranging from 0 (α' = 1.40, ξ = 0) to 0.67 (α' = 0.73, ξ = 0.48). The Z_t–24 and ξ values, both of which change linearly with β' for series B, are plotted on the upper *x*-axes of these figures. The TMR ratios of $Co_2Mn_{1.40}Si_{0.84}$ MTJs at both 4.2 K and 290 K markedly increased with a slight amount of Fe doping to replace Mn. They increased from ξ = 0 ($Co_2Mn_{1.40}Si_{0.84}$) to ξ = 0.11 ($Co_2Mn_{1.24}Fe_{0.16}Si_{0.84}$) (region a). This resulted in significantly high TMR ratios of 2610% at 4.2 K and 429% at 290 K for slightly Fe-doped, Mn-rich CMFS MTJs having $Co_2Mn_{1.24}Fe_{0.16}Si_{0.84}$ (ξ = 0.11) electrodes. These giant TMR ratios for the CMFS MTJ with $Co_2Mn_{1.24}Fe_{0.16}Si_{0.84}$ are much higher than the highest ratios obtained for the CMS MTJ with α =1.30, *i.e.*, 2110% at 4.2 K and 366% at 290 K.

The dependence of the TMR ratio in the range from ξ = 0.11 up to ξ = 0.48 (region b) for series-B CMFS MTJs was also investigated. In contrast to the dependence in region a, the TMR ratios in region b decreased with increasing ξ (1290% at 4.2 K and 304% at 290 K for ξ = 0.48). Note, however, the TMR ratios of 2340% at 4.2 K (360% at 290 K) for ξ = 0.17 ($Co_2Mn_{1.16}Fe_{0.24}Si_{0.84}$ = $Co_2(Mn_{0.83}Fe_{0.17})_{1.40}Si_{0.84}$) and 1950% at 4.2 K (339% at 290 K) for ξ = 0.29 ($Co_2Mn_{1.0}Fe_{0.40}Si_{0.84}$ = $Co_2(Mn_{0.71}Fe_{0.29})_{1.40}Si_{0.84}$) are still higher than or comparable to the 2110% at 4.2 K (366% at 290 K) for CMS with α =1.30. To summarize the above, CMFS MTJs with (Mn+Fe)-rich (δ = 1.40) CMFS electrodes in the relatively low Fe-composition range from ξ = 0.11 to 0.29 exhibited TMR ratios higher than or comparable to the highest TMR ratios for the CMS MTJs (i.e., 2110% at 4.2 K and 366% at 290 K for CMS with α =1.30).

As it is discussed in detail in this section, a systematic investigation of the influence of Mn and Fe film compositions on the TMR characteristics of various CMFS MTJs was done. Furthermore, giant TMR ratios of 2610% at 4.2 K and 429% at 290 K were demonstrated. Note that the TMR ratio of 2610% is the highest TMR ratio demonstrated as of today at 4.2 K and 429% is a very high TMR ratio at 290 K. However, a detailed investigation of the effect of off-stoichiometry on the half-metallic character of quaternary Heusler alloy CMFS has to be done in order to fully understand the key factors that affect the half-metallicity of these materials and thus to fully utilize its characteristics

in spintronic devices.

In the next section the purpose and approaches of this dissertation will be discussed.

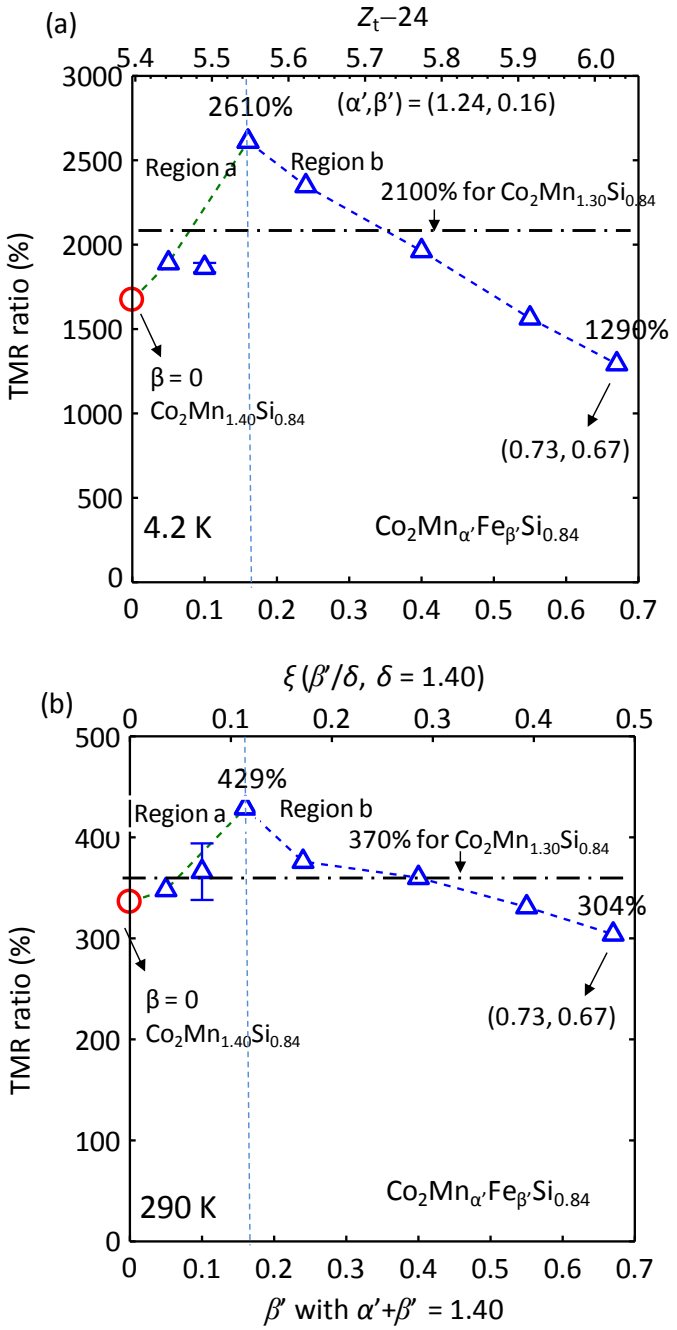

Fig. 1.7. TMR ratios at (a) 4.2 K and (b) 290 K for CMFS MTJs as a function of β' ranging from $\beta' = 0$ ($\alpha' = 1.40$, $\xi = 0$) to $\beta' = 0.67$ ($\alpha' = 0.73$, $\xi = 0.48$) for a fixed $\delta = 1.40$ (CMFS MTJ of series B), where Z_t−24 and ξ, both of which change linearly with β' for series B, are plotted on the upper x-axis of Fig. 1.7 (a) and Fig. 1.7 (b), respectively. The $\beta' = 0$ MTJ corresponds to the $Co_2Mn_{1.40}Si_{0.84}$ MTJ (open red circle) [47].

1.5. Purpose and approach

To take full advantage of the half-metallic character of the quaternary Heusler alloy $Co_2(Mn,Fe)Si$ thin films for spintronic device applications, it is important to study the effect of off-stoichiometry on the half-metallic property of the quaternary CMFS. Therefore, the main purpose of this study was to clarify the effect of off-stoichiometry on the half-metallicity of quaternary Heusler alloy CMFS. To do this, we experimentally investigated the film composition dependence of the saturation magnetization per formula unit, μ_s, of CMFS films with various combinations of α' and β' in $Co_2Mn_{\alpha'}Fe_{\beta'}Si_{0.84}$, and that of the TMR ratio of CMFS MTJs, in combination with first-principles calculations.

Specific objectives include:

[1] Clarification of the origin of the giant TMR ratios demonstrated for CMFS MTJs with Mn-rich, lightly Fe-doped CMFS electrodes. To do this, we experimentally investigated how the TMR ratios of CMFS MTJs with lightly Fe-doped CMFS electrodes depend on the Mn-composition, α', in $Co_2(Mn_{\alpha'}Fe_{0.16})Si_{0.84}$ electrodes in the Mn-rich composition region.

[2] Investigation of the bias voltage dependence of the spin-dependent differential tunneling conductance of CMFS and CMS MTJs exhibiting giant TMR ratios and clarify the origin of this dependence. For this purpose, we studied the dI/dV versus V characteristics (= G spectra) of MTJs having CMFS and CMS electrodes that showed giant TMR ratios.

Chapter 2

Experimental and Computational methods

In this chapter we will explain the overall experimental and computational methods followed in this dissertation. In particular, we will discuss the preparation of CMFS thin films, which were prepared to investigate (1) the effect of off-stoichiometry on the half-metallic characters of quaternary Heusler alloy CMFS and (2) their structural and magnetic properties. We will also give a detailed explanation of the SSFU composition model which was devised by extending the SSFU composition model of the ternary alloy CMS as reported in [36,47] and then we will discuss the computational methods. Furthermore, the detailed experimental procedure of the MTJ preparation and the structural characterization of the prepared MTJs for the purpose of clarifying the giant TMR ratios obtained for Mn-rich, lightly Fe-doped CMFS electrodes will be discussed.

2.1 Sample preparation and characterization of CMFS-based thin films

Epitaxial CMFS thin films with various Mn and Fe compositions, α' and β', were prepared for investigating the effect of off-stoichiometry on μ_s. The layer structure of all thin films prepared for the magnetization measurements was, from the substrate side, MgO buffer (10 nm)/$Co_2Mn_{\alpha'}Fe_{\beta'}Si_{0.84}$ (~30 nm)/MgO barrier (2 nm)/AlO_x cap layer (1 nm) grown on a (001)-oriented MgO single crystalline substrate. This layer structure corresponds to half of an MTJ. Two series of CMFS thin films with different values of α' and β' in $Co_2Mn_{\alpha'}Fe_{\beta'}Si_{\beta}$ (β = 0.84) were prepared. In the series-A CMFS films, α' was fixed at 0.73 while β' was varied from 0 to 0.67 (Table III). Thus, the (Mn+Fe) composition, $\delta = \alpha'+\beta'$, in series A was varied from a δ-deficient composition, δ = 0.73, to a δ-rich composition, δ = 1.40 (a δ-deficient composition in CMFS corresponds to $\delta < 2-\beta$, while a δ-rich composition corresponds to $\delta > 2-\beta$). However, in the series-B films, α' and β' were systematically varied while δ was fixed to a δ-rich value of 1.40; i.e., β' (α') was varied from β' = 0 to 0.67 (from α' = 1.40 to 0.73) (Table IV). Figure 2.1 shows the layer structure of the prepared thin films.

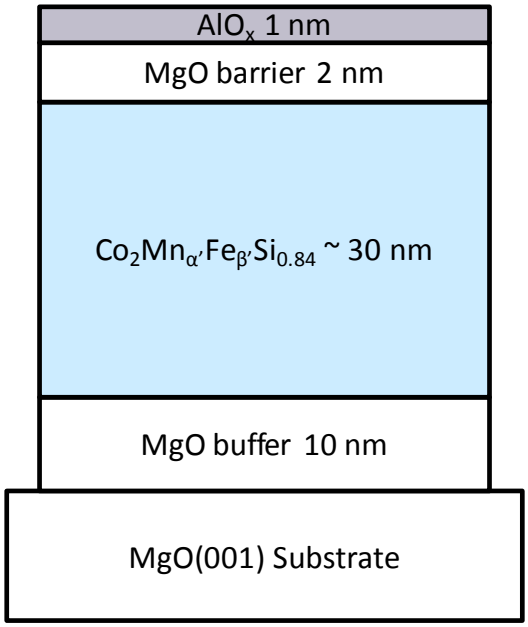

Fig. 2.1. Cross sectional image of the layer structure of a CMFS thin film having a layer structure of from substrate side: MgO buffer (10 nm)/ $Co_2Mn_{\alpha'}Fe_{\beta'}Si_{0.84}$ (30 nm)/ MgO barrier (2 nm)/ AlO_x (1 nm).

Table III. Film compositions expressed as $Co_2Mn_{\alpha'}Fe_{\beta'}Si_{\beta}$, site-specific formula unit (SSFU) composition types, SSFU compositions, measured in-plane (a) and out-of-plane (c) lattice constants, and Z_t-24 values of series-A CMFS films, where Z_t is the valance electron number per formula unit. The first, second, and third brackets in the SSFU composition of type III represent the nominal Co, Mn/Fe, and Si sites, respectively.

$Co_2Mn_{\alpha'}Fe_{\beta'}Si_{0.84}$ (α' = 0.73)	SSFU composition type	SSFU composition	a (nm)	c (nm)	Z_t-24
$Co_2Mn_{0.73}Si_{0.84}$	II	$Co_2[Mn_{0.759}Co_{0.241}][Si_{0.941}Mn_{0.059}]$	0.5610	0.5642	5.658
$Co_2Mn_{0.73}Fe_{0.13}Si_{0.84}$	II	$Co_2[Mn_{0.711}Fe_{0.127}Co_{0.162}][Si_{0.908}Mn_{0.078}Fe_{0.014}]$			5.741
$Co_2Mn_{0.73}Fe_{0.27}Si_{0.84}$	II	$Co_2[Mn_{0.669}Fe_{0.248}Co_{0.083}][Si_{0.875}Mn_{0.091}Fe_{0.034}]$	0.5633	0.5673	5.823
$Co_2Mn_{0.73}Fe_{0.51}Si_{0.84}$	III	$[Co_{1.961}Mn_{0.023}Fe_{0.016}][Mn_{0.589}Fe_{0.411}][Si_{0.824}Mn_{0.104}Fe_{0.073}]$			5.951
$Co_2Mn_{0.73}Fe_{0.57}Si_{0.84}$	III	$[Co_{1.932}Mn_{0.038}Fe_{0.030}][Mn_{0.562}Fe_{0.438}][Si_{0.812}Mn_{0.106}Fe_{0.083}]$	0.5643	0.5679	5.981
$Co_2Mn_{0.73}Fe_{0.62}Si_{0.84}$	III	$[Co_{1.909}Mn_{0.049}Fe_{0.042}][Mn_{0.541}Fe_{0.459}][Si_{0.802}Mn_{0.107}Fe_{0.091}]$			6.005
$Co_2Mn_{0.73}Fe_{0.67}Si_{0.84}$	III	$[Co_{1.887}Mn_{0.059}Fe_{0.054}][Mn_{0.521}Fe_{0.479}][Si_{0.792}Mn_{0.108}Fe_{0.099}]$	0.5633	0.5645	6.028

Now, let's discuss the preparation of the CMFS thin films prepared for the x-ray and magnetization measurements. The CMFS thin film was deposited at RT using radio-frequency magnetron cosputtering from three targets, i.e., nearly stoichiometric CMS, Mn, and Fe, in an ultrahigh vacuum chamber (that has a base pressure of 6×10^{-8} Pa) and was subsequently *in situ* annealed at 600°C for 15 min. to improve the atomic ordering. The α' and β' in $Co_2Mn_{\alpha'}Fe_{\beta'}Si_{0.84}$ were systematically varied by adjusting the relative amounts of sputtered Mn and Fe. The MgO barrier was deposited as a protection layer of the CMFS film because the interface between CMS, CMG, or CMFS with a MgO barrier has high-quality structural [47], electronic, and magnetic properties [38−32,48−50]. The MgO buffer and barrier were deposited by electron beam evaporation in the same chamber at 400°C and RT, respectively. After depositing the MgO barrier, the sample was transferred to another ultrahigh-vacuum chamber (through an ultrahigh vacuum), and an Al metallic layer (1 nm) was deposited by electron beam evaporation. After that, the AlO_x cap was prepared by exposing the Al layer to an O_2 atmosphere of ~ 1×10^5 Pa for 2 h. The film composition of the prepared CMFS film was determined by inductively coupled plasma analysis with an accuracy of 2%−3% for each element except Si, for which the accuracy was 5%.

Table IV. Film compositions expressed as $Co_2Mn_{\alpha'}Fe_{\beta'}Si_{\beta}$, SSFU compositions, measured lattice constants *a* and *c*, and Z_t−24 values of series-B CMFS films.

$Co_2Mn_{\alpha'}Fe_{\beta'}Si_{0.84}$ ($\delta = \alpha' + \beta' = 1.40$)	SSFU composition type	SSFU composition	*a* (nm)	*c* (nm)	Z_t−24
$Co_2Mn_{1.40}Si_{0.84}$	III	$[Co_{1.887}Mn_{0.113}][Mn_{1.00}][Si_{0.792}Mn_{0.208}]$	0.5690	0.5657	5.396
$Co_2Mn_{1.35}Fe_{0.05}Si_{0.84}$	III	$[Co_{1.887}Mn_{0.109}Fe_{0.004}]$ $[Mn_{0.964}Fe_{0.036}][Si_{0.792}Mn_{0.200}$ $Fe_{0.007}]$			5.443
$Co_2Mn_{1.30}Fe_{0.10}Si_{0.84}$	III	$[Co_{1.887}Mn_{0.105}Fe_{0.008}][Mn_{0.029}Fe_{0.071}][Si_{0.792}Mn_{0.193}$ $Fe_{0.015}]$			5.491
$Co_2Mn_{1.24}Fe_{0.16}Si_{0.84}$	III	$[Co_{1.887}Mn_{0.100}Fe_{0.013}][Mn_{0.886}Fe_{0.114}][Si_{0.792}Mn_{0.184}$ $Fe_{0.024}]$	0.5679	0.5666	5.547
$Co_2Mn_{1.16}Fe_{0.24}Si_{0.84}$	III	$[Co_{1.887}Mn_{0.094}Fe_{0.019}][Mn_{0.829}Fe_{0.171}][Si_{0.792}Mn_{0.172}$ $Fe_{0.036}]$			5.623
$Co_2Mn_{1.00}Fe_{0.40}Si_{0.84}$	III	$[Co_{1.887}Mn_{0.081}Fe_{0.032}][Mn_{0.714}Fe_{0.286}][Si_{0.792}$ $Mn_{0.148}$ $Fe_{0.059}]$	0.5656	0.5677	5.774
$Co_2Mn_{0.85}Fe_{0.55}Si_{0.84}$	III	$[Co_{1.887}Mn_{0.069}Fe_{0.044}][Mn_{0.607}Fe_{0.393}][Si_{0.792}Mn_{0.126}$ $Fe_{0.082}]$			5.915
$Co_2Mn_{0.73}Fe_{0.67}Si_{0.84}$	III	$Co_{1.887}Mn_{0.059}Fe_{0.054}][Mn_{0.521}Fe_{0.479}][Si_{0.792}Mn_{0.108}$ $Fe_{0.099}]$	0.5633	0.5645	6.028

The CMFS layers grown on MgO-buffered MgO(001) substrates were characterized by making reflection high-energy electron diffraction (RHEED) observations during growth. We made in situ observations of the RHEED patterns for each successive layer of the MgO buffer/CMFS (30 nm) heterostructures. Sharp streak patterns dependent on the electron injection direction were obtained for each successive layer, clearly indicating that the CMFS layer grew epitaxially on a MgO buffer. Typical RHEED pattern of a CMFS thin film with a composition of $Co_2Mn_{1.00}Fe_{0.40}Si_{0.84}$ grown on a 10 nm MgO buffer is shown in Fig. 2.2 along with the RHEED pattern of the MgO buffer layer. These results were consistent with those of the structural characterization by aberration-corrected Z-contrast scanning transmission electron microscopy for a CMFS lower electrode grown on a CoFe buffer layer and a CMFS upper electrode grown on a MgO tunnel barrier in a fully epitaxial MTJ with $Co_2Mn_{1.24}Fe_{0.16}Si_{0.84}$ electrodes: both consisted of $L2_1$ regions and B2 regions [47] as will be later discussed in this chapter of section 2.4.

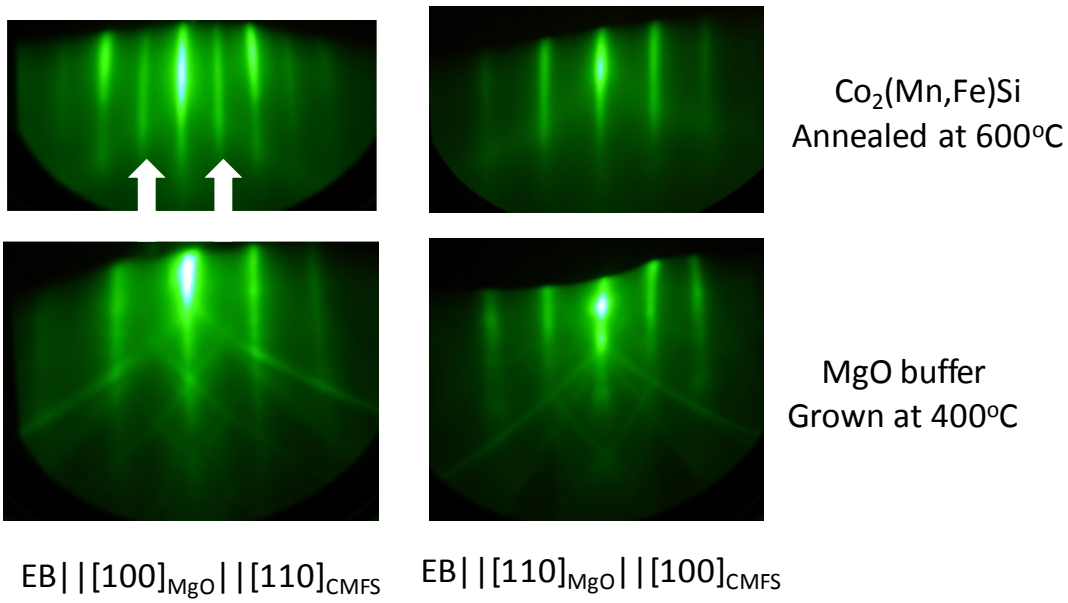

Fig. 2.2. RHEED pattern of a CMFS thin film after annealed at 600°C showing an epitaxial growth of the film on MgO buffer. The two arrows show the 11* superlattice peaks observed for this film. The RHEED pattern of the MgO buffer layer grown at a substrate temperature of 400°C is also shown.

The magnetic properties of the two series of CMFS films were investigated using a superconducting quantum interference device (SQUID) magnetometer at 10 K. The saturation magnetization for the total volume of each film, M_s, at 10 K was estimated by extrapolation of the obtained *M-H* curve to $H = 0$ to subtract the contribution from the MgO substrate. Figure 2.3 shows the *M-H* curve of series-A and series-B CMFS films. In order to determine μ_s from the obtained M_s of each CMFS film, the film thickness was precisely measured by using a low-angle x-ray reflectivity (XRR) technique. For all films, clear oscillations in the experimental reflectivity scan were observed up to $2\theta \sim 7^o$, indicating smooth interfaces and surface. A fit of the oscillatory XRR intensity for a 2θ range from 1.4 to 5.6° by Parratt formalism [36,51] was used to determine the thickness of each $Co_2Mn_{\alpha'}Fe_{\beta'}Si_{0.84}$ layer. Figure 2.4 shows typical XXR scan of a CMFS thin film with a composition of $Co_2Mn_{0.73}Fe_{0.67}Si_{0.84}$. We also determined the in-plane, *a*, and out-of-plane, *c*, lattice constants of each series of films, including the CMS films, by making x-ray Bragg scans with a four-axis x-ray diffractometer (Bruker AXS D8 Discover Hybrid) equipped with a scintillation counter (Tables III and IV) and then incorporated these values into the determination of μ_s.

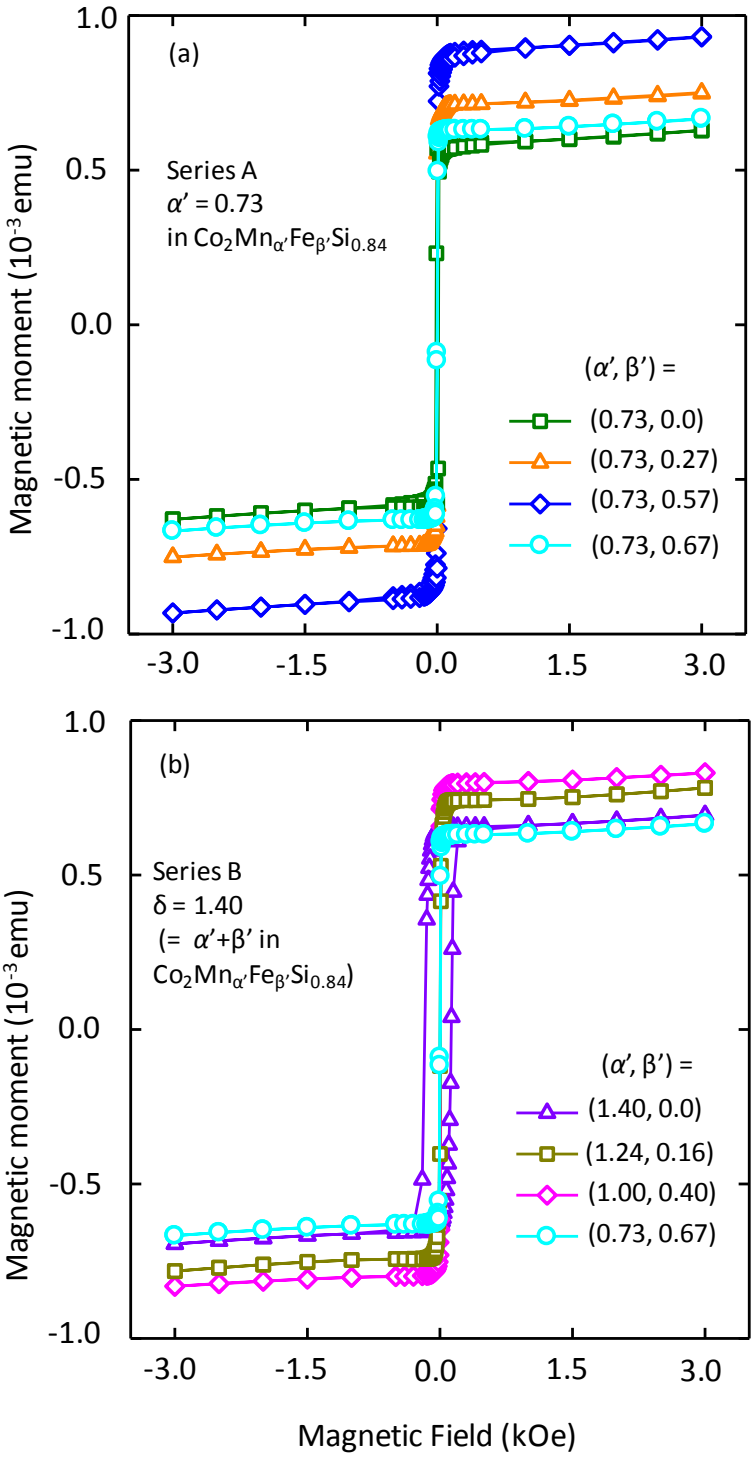

Fig. 2.3. Typical magnetic hysteresis curves for (a) series-A and (b) series-B CMFS films at 10 K measured using a SQUID magnetometer, where the magnetic field (H) was applied in the plane of the film along the [1−10] CMFS easy axis.

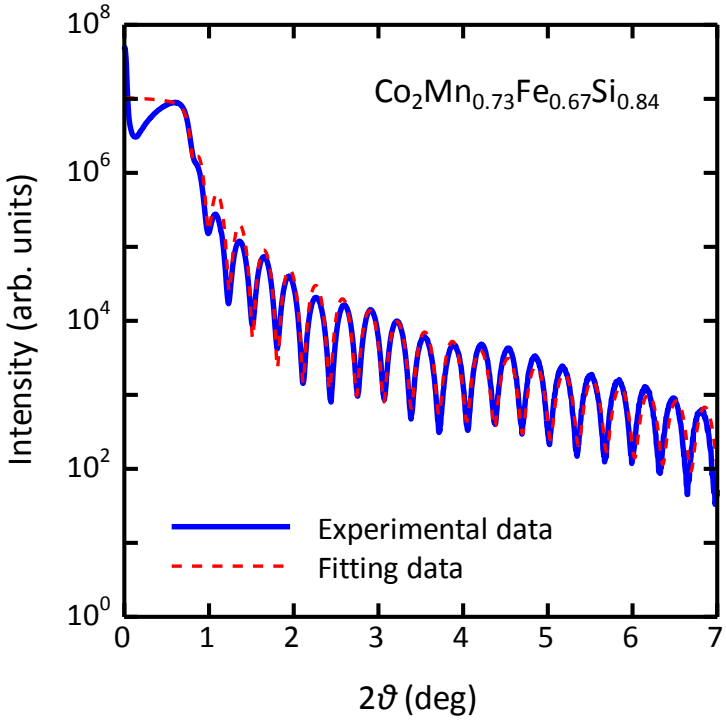

Fig. 2.4. Typical low angle x-ray reflectivity scan of a CMFS thin film having a film composition of $Co_2Mn_{0.73}Fe_{0.67}Si_{i0.84}$.

Table V. Film compositions expressed as $Co_2Mn_{\alpha'}Fe_{\beta'}Si_{\beta}$, SSFU composition types, SSFU compositions, measured lattice constants *a* and *c*, and Z_t−24 values of series-C CMFS films.

$Co_2Mn_{\alpha}Fe_{\beta'}Si_{0.84}$ (β' = 0.16)	SSFU composition type	SSFU composition	*a* (nm)	*c* (nm)	Z_t−24
$Co_2Mn_{1.14}Fe_{0.16}Si_{0.84}$	III	$[Co_{1.932}Mn_{0.059}Fe_{0.008}][Mn_{0.877}Fe_{0.123}][Si_{0.812}Mn_{0.165}Fe_{0.023}]$			5.585
$Co_2Mn_{1.19}Fe_{0.16}Si_{0.84}$	III	$[Co_{1.909}Mn_{0.080}Fe_{0.011}][Mn_{0.881}Fe_{0.119}][Si_{0.802}Mn_{0.175}Fe_{0.023}]$			5.566
$Co_2Mn_{1.24}Fe_{0.16}Si_{0.84}$	III	$[Co_{1.887}Mn_{0.100}Fe_{0.013}][Mn_{0.886}Fe_{0.114}][Si_{0.792}Mn_{0.184}Fe_{0.024}]$	0.5679	0.5666	5.547

2.2 Computational methods

We performed first-principles density functional calculations to theoretically investigate the effect of off-stoichiometry in CMFS on the electronic and magnetic states on the basis of the Korringa-Kohn-Rostoker (KKR) method [52,53] with the coherent potential approximation (CPA) for atomic disorder. The generalized gradient approximation (GGA) was used for the exchange and correlation term [54]. We theoretically evaluated the total spin magnetic moments per formula unit, m_{spin}; the spin-resolved, local density of states (LDOS); and spin polarizations at E_F for three series of CMFS: (1) series A and (2) series B, and (3) series C of $Co_2(Mn_{\alpha'}Fe_{0.16})Si_{0.84}$ with a fixed β' of 0.16 in $Co_2(Mn_{\alpha'}Fe_{\beta'})Si_{0.84}$ and α' ranging from α' = 1.14 (δ = 1.30) to α' = 1.24 (δ = 1.40). We used a scalar relativistic calculation, in which the spin-orbit interaction was neglected. For the Brillouin zone (BZ) integration, 8000 points were included in the full BZ. The unit cell of the full-Heusler alloy X_2YZ with the $L2_1$ structure consists of four face-centered cubic sublattices. Each has an atom basis as follows: X element at (1/4,1/4,1/4) and (3/4,3/4,3/4), Y at (0,0,0), and Z at (1/2,1/2,1/2). We used the experimental lattice constants a described above for series-A (Table III), series-B (Table IV), and series-C (Table V) CMFS but ignored the small difference between a and c, assuming a cubic lattice with the experimental a value for each film. The calculations were based on the SSFU composition model assuming antisite formation rather than vacancy formation to accommodate off-stoichiometry, as described in Sec. 2.3 below.

2.3 Formula unit composition model

The SSFU compositions for off-stoichiometric Co-based Heusler alloys are essential to understanding the effect of off-stoichiometry on their half-metallicity. We have proposed an antisite-based SSFU composition model for the ternary Heusler alloys CMS and CMG, which assumes the formation of only antisite defects, not vacancies, to accommodate off-stoichiometry [13,36]. The basis for this assumption is the theoretically predicted higher formation energies of vacancies compared with those of antisite defects for CMS [32,55]. We extended this model to off-stoichiometric quaternary $Co_2(Mn_{\alpha'}Fe_{\beta'})Si_{\beta}$ by assuming that the Mn-to-Fe ratio is constant for all nominal Mn/Fe,

Si, and Co sites. According to this model, each site in the $L2_1$ structure is occupied either by the nominal atom (Co, Mn/Fe, or Si for CMFS) for that site or by an antisite defect atom, so the total number of atoms included in the formula unit is always four, even though the film is off-stoichiometric in terms of the Co:Mn/Fe:Si atomic ratio. Thus, this model preserves a generalized 2:1:1 stoichiometry in terms of the site occupancy.

Table VI. General expressions for SSFU compositions of $Co_2Mn_{\alpha'}Fe_{\beta'}Si_{\beta}$, from type I to type IV for $0 < \delta < 2$ and $0 < \beta < 2$; where, $\delta = \alpha'+\beta'$ and $\xi = \beta'/(\alpha'+\beta')$. The first, second, and third brackets in the SSFU composition of type III, $[Co_{2-x}(Mn_{1-\xi}Fe_{\xi})_x][Mn_{1-\xi}Fe_{\xi}][Si_{1-y}(Mn_{1-\xi}Fe_{\xi})_y]$, represent the nominal Co, Mn/Fe, and Si sites.

SSFU composition type	Site-specific formula unit composition (SSFU composition)	x	y
I	$Co_2[(Mn_{1-\xi}Fe_{\xi})_{1-x-y}Co_xSi_y]Si$	$\frac{2(2-(\delta+\beta))}{2+\delta+\beta}$	$\frac{3\beta-(2+\delta)}{2+\delta+\beta}$
II	$Co_2[(Mn_{1-\xi}Fe_{\xi})_{1-x}Co_x][Si_{1-y}(Mn_{1-\xi}Fe_{\xi})_y]$	$\frac{2(2-(\delta+\beta))}{2+\delta+\beta}$	$\frac{2+\delta-3\beta}{2+\delta+\beta}$
III	$[Co_{2-x}(Mn_{1-\xi}Fe_{\xi})_x][Mn_{1-\xi}Fe_{\xi}][Si_{1-y}(Mn_{1-\xi}Fe_{\xi})_y]$	$\frac{2(\delta+\beta-2)}{2+\delta+\beta}$	$\frac{2+\delta-3\beta}{2+\delta+\beta}$
IV	$[Co_{2-x}(Mn_{1-\xi}Fe_{\xi})_x][(Mn_{1-\xi}Fe_{\xi})_{1-y}Si_y]Si$	$\frac{2(\delta+\beta-2)}{2+\delta+\beta}$	$\frac{3\beta-(2+\delta)}{2+\delta+\beta}$

Given this assumption, the role of $\delta = \alpha'+\beta'$ for the quaternary CMFS is identical to α for the ternary CMS expressed as $Co_2Mn_{\alpha}Si_{\beta}$ in terms of the determination of the SSFU composition type. Accordingly, the SSFU composition types developed for off-stoichiometric ternary $Co_2Mn_{\alpha}Si_{\beta}$ ($0 < \alpha < 2$ and $0 < \beta < 2$) [36] can be applied to off-stoichiometric quaternary $Co_2(Mn_{\alpha'}Fe_{\beta'})Si_{\beta}$ ($0 < \delta < 2$ and $0 < \beta < 2$) by replacing α in $Co_2Mn_{\alpha}Si_{\beta}$ with $\delta = \alpha'+\beta'$ for quaternary $Co_2(Mn_{\alpha'}Fe_{\beta'})Si_{\beta}$. This is because we can

rewrite the empirical expression of $Co_2(Mn_{\alpha'}Fe_{\beta'})Si_\beta$ as $Co_2[(Mn_{1-\xi}Fe_\xi)]_\delta Si_\beta$ and thus make a direct correspondence between α and δ. The resultant general expressions for the SSFU composition types I to IV are shown in Table VI. Here, the Mn-to-Fe ratio, $1-\xi$: ξ, in the general expressions of the SSFU compositions is given by the α'-to-β' ratio in the expression of $Co_2(Mn_{\alpha'}Fe_{\beta'})Si_\beta$. (The expression of $Co_2(Mn_{\alpha'}Fe_{\beta'})Si_\beta$ is an empirical one for a film composition in which each atomic composition is expressed with respect to Co_2.) In addition to the previously introduced type I to type III SSFU compositions [36], we introduced composition type IV for the region of $\beta > (2+\delta)/3$ and $\delta > 2-\beta$ in order to extend the generality of the antisite-based SSFU composition model.

Tables III, IV, and V, respectively, show the calculated SSFU compositions for CMFS series A ($Co_2(Mn_{0.73}Fe_{\beta'})Si_{0.84}$), with a fixed α' of 0.73 and various β' ranging from 0 (δ = 0.73) to 0.67 (δ = 1.40); series B ($Co_2(Mn_{\alpha'}Fe_{\beta'})Si_{0.84}$), with a constant δ of 1.40 and various α' and β' ranging from α' = 0.73 (β' = 0.67) to α' = 1.40 (β' = 0); and series C ($Co_2(Mn_{\alpha'}Fe_{0.16})Si_{0.84}$), with a fixed β' of 0.16 and various α' ranging from 1.14 (δ = 1.30) to 1.24 (δ = 1.40). All films of series A−C fall into type II or type III SSFU compositions, where type II contains $Co_{Mn/Fe}$ antisites, while type III contains no $Co_{Mn/Fe}$ antisites. The Z_t-24 value for each film composition is also shown for series-A to series-C CMFS films, where Z_t is the valence electron number per formula unit. The Z_t-24 values for off-stoichiometric CMFS films are those given by the antisite-based SSFU composition model. Note, however, that the same values can be obtained by assuming that each formula unit contains four atoms along with antisites, not vacant sites, to accommodate off-stoichiometry without specifying the site occupation [47]. Figure 2.5 shows a schematic diagram showing the regions of the SSFU composition types I to IV in the $\delta-\beta$ plane with $\delta = \alpha' + \beta'$ for $Co_2Mn_{\alpha'}Fe_{\beta'}Si_\beta$ with the restrictions of $0 < \delta < 2$ and $0 < \beta < 2$

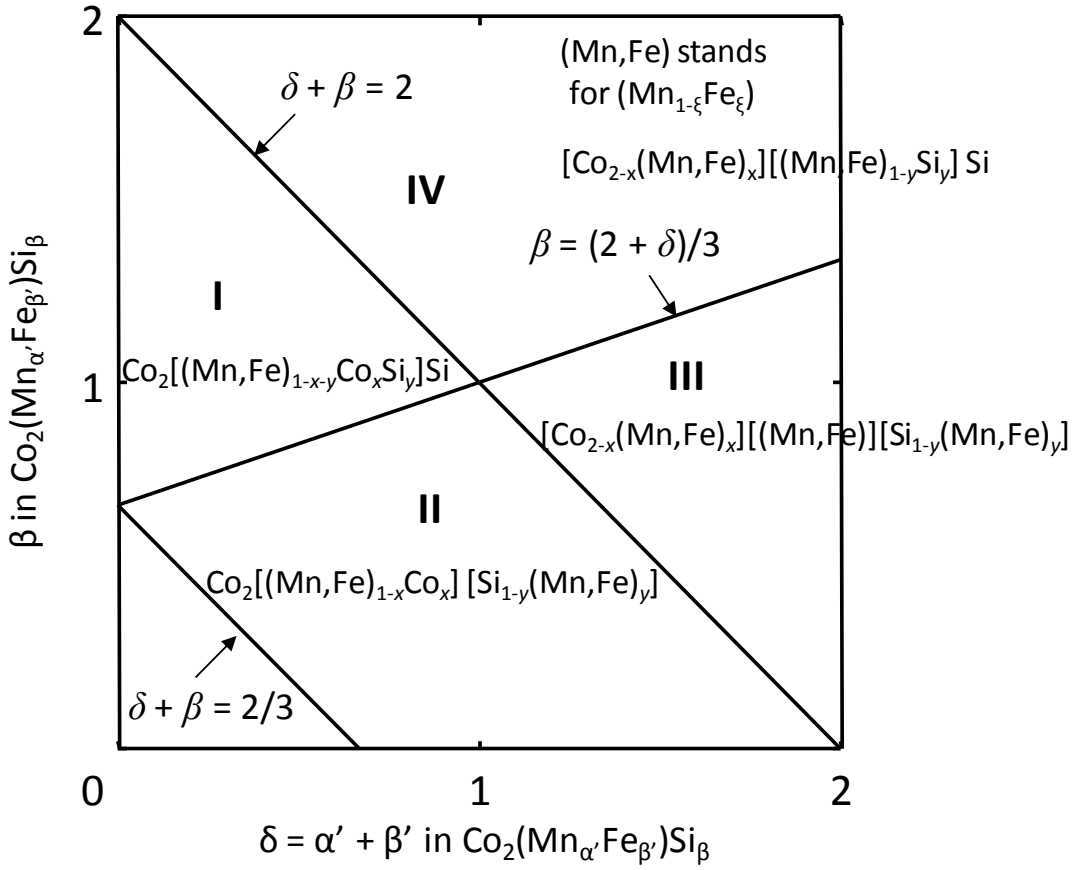

Fig. 2.5. Schematic diagram showing the regions of the SSFU composition types I to IV in the δ–β plane with $\delta = \alpha' + \beta'$ for $Co_2Mn_{\alpha'}Fe_{\beta'}Si_\beta$ with the restrictions of $0 < \delta < 2$ and $0 < \beta < 2$ [36].

2.4 Preparation and characterization of MTJ layer structures

For the purpose of investigating the origin of the giant TMR ratios of 2610% at 4.2 K and 429% at 290 K for a CMFS MTJ with Mn-rich, lightly Fe-doped electrodes, we prepared MTJs with CMFS upper and lower electrodes having a Mn-rich, and lightly Fe-doped composition, $Co_2Mn_{\alpha'}Fe_{0.16}Si_{0.84}$. That is, we fixed the Fe-composition to $\beta' = 0.16$ while the Mn-composition, α', was varied in the Mn-rich region from $\alpha' = 1.14$ to $\alpha' = 1.24$. The layer structure of the MTJs is as follows (from the substrate side): MgO buffer (10 nm)/$Co_{50}Fe_{50}$ (CoFe) buffer (30 nm)/$Co_2Mn_{\alpha'}Fe_{0.16}Si_{0.84}$ lower electrode (3 nm)/MgO barrier (1.4−3.2 nm)/$Co_2Mn_{\alpha'}Fe_{0.16}Si_{0.84}$ upper electrode (3 nm)/CoFe (1.1 nm)/$Ir_{22}Mn_{78}$ (10 nm)/Ru cap (5 nm), grown on a MgO (001) single-crystal substrate. The schematic diagram of the layer structure of the MTJ is shown in Fig. 2.6.

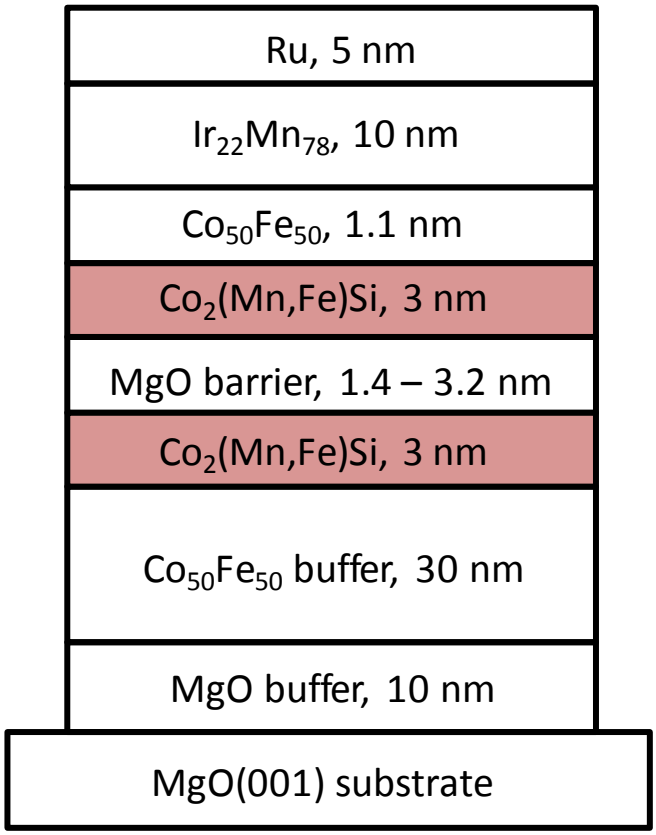

Fig. 2.6. Schematic diagram of MTJ layer structure consisting of (from the substrate side) MgO buffer (10 nm)/$Co_{50}Fe_{50}$ (CoFe) buffer (30 nm)/Co_2(Mn,Fe)Si (CMFS) lower electrode (3 nm)/MgO barrier (1.4–3.2 nm)/CMFS upper electrode (3 nm)/CoFe (1.1 nm)/$Ir_{22}Mn_{78}$ (10 nm)/Ru cap (5 nm), grown on a MgO(001) single-crystal substrate.

Each layer was successively deposited in an ultrahigh vacuum chamber (having a base pressure of 6×10^{-8} Pa). The MgO buffer was deposited by electron beam evaporation at a substrate temperature of 400°C. Then, after cooling down, the CoFe buffer was deposited at RT and was subsequently annealed at 400°C. The CMFS upper and lower electrodes were deposited at RT using radio-frequency (rf) magnetron cosputtering from three targets, i.e., nearly stoichiometric Co_2MnSi, Mn, and Fe, in an ultrahigh vacuum chamber and was subsequently *in situ* annealed at 600°C for 15 min. to improve the atomic ordering. α' and β' in $Co_2Mn_{\alpha'}Fe_{\beta'}Si_{0.84}$ were systematically varied by adjusting the relative amounts of sputtered Mn and Fe. The composition of the CMFS film was determined through inductively coupled plasma analysis with an accuracy of 2–3% for each element, except Si, for which the accuracy was 5%. As explained at the beginning of this section, the upper and lower CMFS electrodes have a fixed Fe

composition of β' = 0.16 while the Mn-composition is varied slightly from α' = 1.14 to α' = 1.24.

The MTJ layer structure was annealed *in situ* at 600°C both just after deposition of the CMFS lower electrode and fairly soon after deposition of the CMFS upper electrode. Similar to MgO buffer, the MgO barrier layer was prepared by electron beam evaporation at RT. Layers for the exchange bias, i.e. CoFe(1.1 nm)/$Ir_{22}Mn_{78}$(10 nm), were deposited at RT using rf magnetron sputtering. Finally, the whole MTJ layer structure was capped by depositing Ru at RT using rf magnetron sputtering.

The MTJ layer structures were characterized by making RHEED observations during growth and by aberration-corrected Z-contrast scanning transmission electron microscopy (STEM). High-resolution STEM (HRSTEM) was performed on an FEI Titan STEM with a CEOS probe aberration corrector operated at 200 kV at about 0.1 nm spatial resolution, 24.5 mrad convergence angle, and 25 pA probe current. The high-angle annular dark-field (HAADF) detector subtended 54 to 270 mrad. All the HRSTEM images were smoothed with a Gaussian filter smaller than the 0.1 nm instrumental resolution to reduce shot noise. Bright field TEM observations were carried out with an FEI Tecnai TF-30 operated at 300 kV. The STEM samples were prepared by tripod polishing [47] and finished by ion milling. Figure 2.7 shows a typical Z-contrast STEM image of an as-prepared CoFe-buffered CMFS MTJ layer structure consisting of (from the lower side) CoFe buffer/lower CMFS (3 nm)/MgO barrier (~1.4 nm)/upper CMFS (3 nm)/CoFe (1.1 nm)/$Ir_{22}Mn_{78}$ (10 nm)/Ru cap (5 nm) with $Co_2Mn_{1.24}Fe_{0.16}Si_{0.84}$ electrodes; it was taken along the [1−10] direction of the CMFS layers. This image clearly shows that all layers grew epitaxially and were single-crystalline. The interfaces were atomically flat. Similar to CoFe-buffered CMS MTJs [15], there were no lattice misfit dislocations between the CoFe buffer and CMFS lower electrode. This indicates that the CMFS lower electrode was lattice-matched to the CoFe buffer.

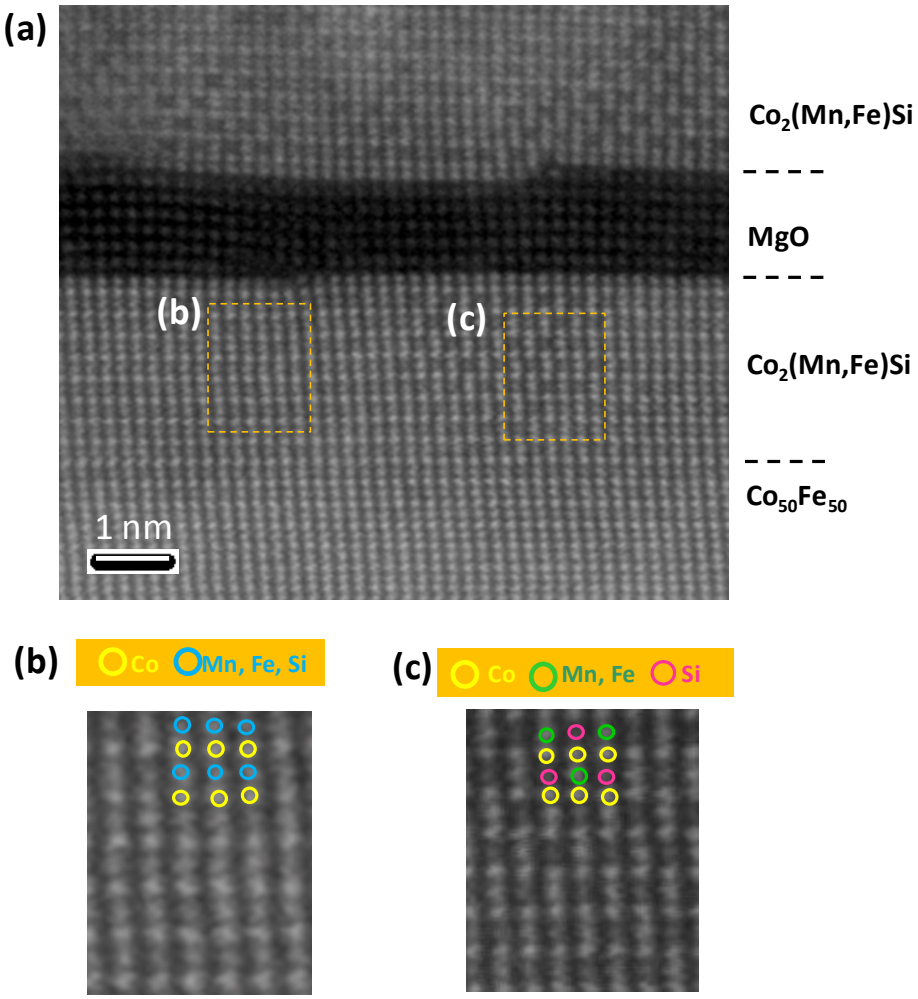

Fig. 2.7. High-resolution Z-contrast scanning TEM (STEM) image of a $Co_{50}Fe_{50}$ (CoFe)-buffered $Co_2(Mn,Fe)Si$ (CMFS) MTJ layer structure consisting of (from the lower side) CoFe buffer/lower CMFS (3 nm)/MgO barrier (~1.4 nm)/upper CMFS (3 nm)/CoFe (1.1 nm)/$Ir_{22}Mn_{78}$ (10 nm)/Ru cap (5 nm) with (Mn+Fe)-rich $Co_2Mn_{1.24}Fe_{0.16}Si_{0.84}$ electrodes; it was taken along the [1-10] direction of the CMFS. (b) and (c) Enlarged images of two different regions of (a) respectively showing the B_2 and L_{21} structures in the lower CMFS electrode [47].

In Figure 2.7 (a), the atomic lattice with all three sites is clearly visible in both the upper and lower (Mn+Fe)-rich CMFS electrodes. Figure 2.7 (a) also shows the upper and lower electrodes consisting of $L2_1$ regions and B2 regions. Figure 2.7 (b) and 2.7 (c) show enlarged images of two different regions of the lower CMFS electrode; they reveal B2 and $L2_1$ structures, respectively. The coexistence of these structures in the δ-rich CMFS electrodes (3 nm) is similar to that in thick Mn-rich CMS films (30 nm) [36]. Note that the higher ratio of the $L2_1$ region for Mn-deficient CMS films and the increased ratio of the B2 region for Mn-rich CMS films have been observed in the previous study and were explained in terms of the Si occupation ratio at the nominal Si site being higher for Mn-deficient CMS and lower for Mn-rich CMS in their SSFU compositions [47]. Thus, the coexistence of the $L2_1$ and B2 regions can be ascribed to the (Mn+Fe)-rich composition of the $Co_2Mn_{1.24}Fe_{0.16}Si_{0.84}$ electrodes.

To further characterize the interfacial structural quality of CoFe-buffered CMFS MTJs, we investigated the densities of misfit dislocations at the interfaces with the MgO barrier by examining the two-beam bright-field TEM images. Figure 2.8 shows an image of a CoFe-buffered CMFS MTJ layer structure with $Co_2Mn_{1.24}Fe_{0.16}Si_{0.84}$ electrodes excited with reciprocal vectors parallel to the plane (g = $[200]_{MgO}$ and $[220]_{CMFS}$). The image shows strain contrasts arising from periodically spaced misfit dislocations at the lower and upper interfaces with the MgO barrier. The dislocation spacing values at the lower and upper interfaces were respectively 6.3 (0.3) and 6.1 (0.2) nm, where the values in parentheses are the standard deviations. These values are comparable to the value of 6.3 ± 0.1 nm for the lower and upper interfaces in the CoFe-buffered CMS MTJ with Mn-rich $Co_2Mn_{1.29}Si_{1.0}$ electrodes [15]. Thus, the structural properties of the upper and lower interfacial regions of the CoFe-buffered CMFS MTJ were similar to those of the CoFe-buffered CMS MTJ in terms of the misfit dislocation spacing at the interfaces. Such a large misfit dislocation spacing would enhance the contribution of coherent tunnelling to the TMR characteristics [15].

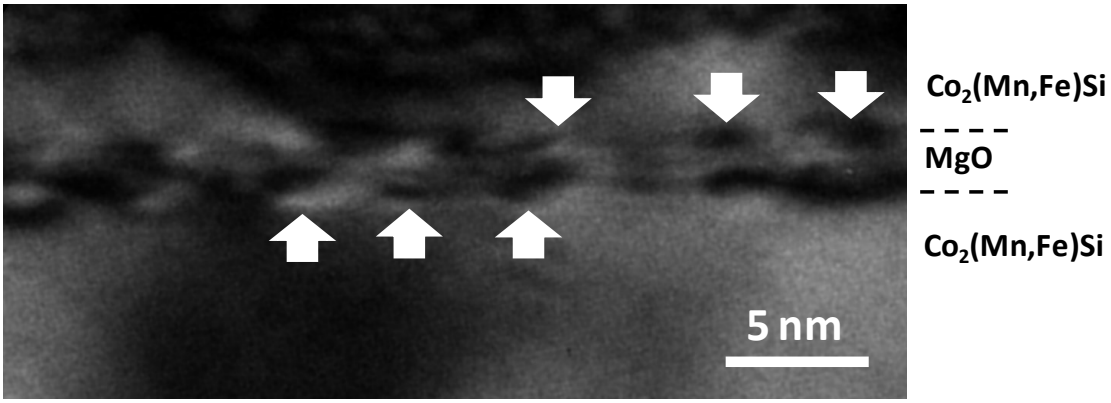

Fig. 2.8. Two-beam bright-field TEM image of a CoFe-buffered CMFS MTJ layer structure with (Mn+Fe)-rich $Co_2Mn_{1.24}Fe_{0.16}Si_{0.84}$ electrodes (the same sample as shown in Fig. 2(a)) excited with reciprocal vectors parallel to the plane (g = $[200]_{MgO}$ and $[220]_{Co2(Mn,Fe)Si}$). The arrows provide a guide to show the misfit dislocation contrasts [47].

The magnetoresistance was measured using the dc four-probe method. The TMR characteristics of the MTJs were measured at a bias voltage of 5 mV at 290 K and 1 mV at 4.2 K. We defined the TMR ratio as $(R_{AP}-R_P)/R_P$, where R_{AP} and R_P are the tunneling resistances for the antiparallel and parallel magnetization configurations between the upper and the lower electrodes. The minor-loop TMR curves for the fabricated MTJs showed that the tunneling resistances R_P and R_{AP} were almost constant against the magnetic field. Accordingly, the error of the TMR ratio, defined as $(R_{AP}-R_P)/R_P$, was less than about 2% for each junction.

Figure 2.9 plots typical dependences on t_{MgO} of R_PA, $R_{AP}A$, and the TMR ratio at 290 K for these MTJs fabricated on a 20 x 20 mm^2 MgO(001) substrate over a t_{MgO} range from 2.2 to 3.0 nm, where A is the nominal junction area of 10 x 10 μm^2. The dependences of R_pA and $R_{AP}A$ on t_{MgO} were exponential, with almost identical slopes in $\log(RA)$ over the whole plotted range. Moreover, the almost identical slopes resulted in nearly constant TMR ratios from 2.2 to 3.0 nm of t_{MgO}. Accordingly, the standard deviation of the TMR ratio obtained for the MTJs was about 3%. These results indicate that the TMR characteristics of the MTJs fabricated on a 20×20 mm^2 substrate had good reproducibility.

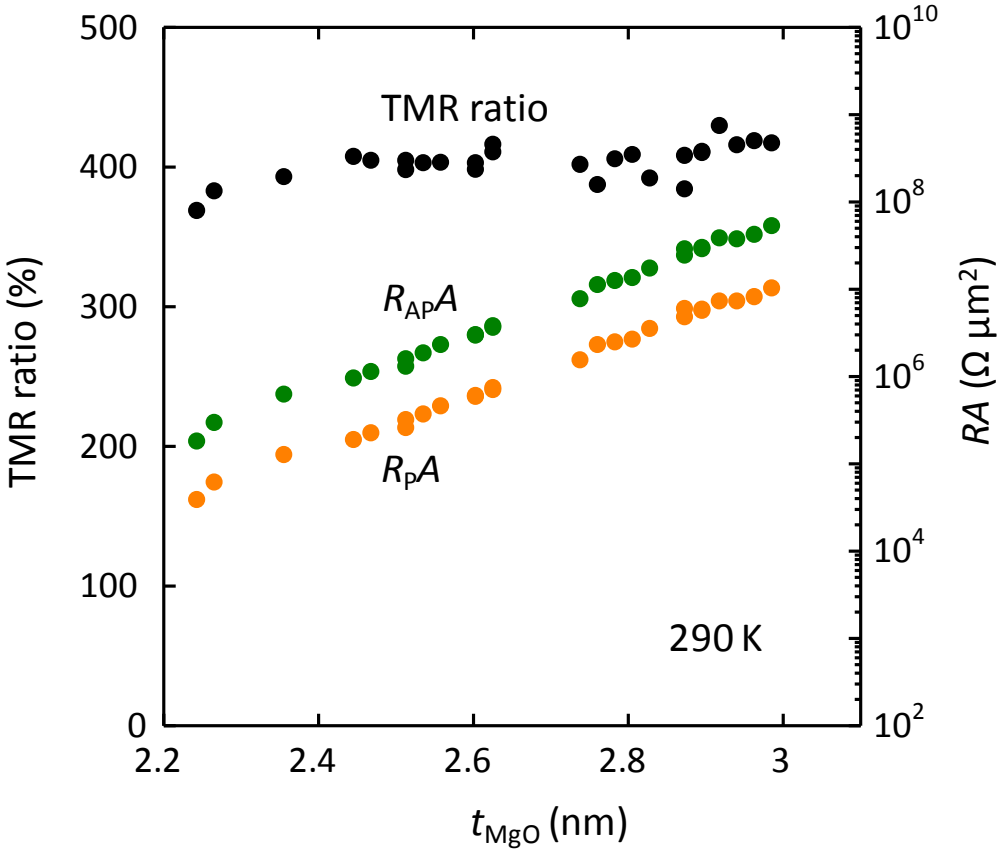

Fig. 2.9. Typical dependence of R_PA, $R_{AP}A$, and TMR ratio on MgO barrier thickness (t_{MgO}) at 290 K for CMFS MTJs with $Co_2Mn_{1.24}Fe_{0.16}Si_{0.84}$ electrodes fabricated on a 20 x 20 mm^2 MgO(001) substrate for a t_{MgO} range from 2.2 to 3.0 nm, where A is the nominal junction area of 10 x 10 μm^2. The MgO tunnel barrier had a wedge structure, and its nominal thickness was varied from 1.4 to 3.2 nm on each 20 × 20 mm^2 substrate by linearly moving the shutter during the deposition by electron-beam evaporation.

Finally, in order to investigate the half-metallic electronic structure of the CMFS electrodes and study the bias voltage dependence of the spin-dependent differential conductance characteristics, the differential conductance (G = dI/dV) versus V of the fabricated MTJs was measured with a conventional lock-in method at 4.2 K. The modulation peak-to-peak voltage was 10 mV and the modulation frequency was 317 Hz. The second derivative d^2I/dV^2 spectra were obtained mathematically from the dI/dV data. The bias voltage (V) was defined with respect to the lower CMFS electrode, i.e., electrons tunnel from the lower CMFS electrode to the upper CMFS electrode at a positive V.

2.5 Summary

In summary, we prepared two series of CMFS thin films, series A and series B, for the purpose of investigating the effect of off-stoichiometry on the half-metallic characteristics of the quaternary Heusler alloy CMFS. Furthermore, as an aid to analyze our experimentally obtained results, we conducted first-principles density functional calculation which was based the proposed anti-sites based SSFU composition model. In this study, the antisite-based SSFU composition model originally developed for ternary CMS was extended for the quaternary Heusler alloy. Finally, in order to clarify the bias voltage dependence of the spin-dependent tunneling conductance, we prepared MTJs having CMFS electrodes with a fixed Fe-composition of β' = 0.16 and varying Mn-composition in the Mn-rich composition region. We, then, conducted a spectroscopy analysis by measuring the bias voltage dependence of the differential conductance of CMFS and CMS MTJs in order to investigate the half-metallic electronic structure of quaternary Heusler alloy CMFS and also to investigate the bias voltage dependence of the spin-dependent differential tunneling conductance of CMFS and CMS MTJs.

Chapter 3

Effect of off-stoichiometry on the half-metallic character of quaternary Heusler alloy CMFS

To fully exploit the half-metallic character of Co_2YZ Heusler alloys, the effect of defects associated with off-stoichiometry on their half-metallicity has to be understood. As it is discussed in detail in chapter 1 of this dissertation, it is theoretically predicted that a disorder between Co and *Y* site destroys the half-metallicity by introducing in-gap states at E_F in the minority-spin states [35,44]. Li et al. [36] from our research group reported an experimental investigation of the effect of defects on the half-metallicity of the ternary Heusler alloy CMS through Mn composition (α) dependence of the μ_s of $Co_2Mn_\alpha Si_\beta$ thin films and the TMR ratio of CMS MTJs having $Co_2Mn_\alpha Si_\beta$ electrodes. In particular, it was demonstrated that harmful Co_{Mn} antisites were present in Mn-deficient CMS and the effectiveness of preparing CMS thin films with Mn-rich composition was highly effective to retain the half-metallic character of ternary alloy CMS.

Similarly, as it is discussed in detail in chapter 1 for series-A and series-B CMFS MTJs, by systematically varying the Mn and Fe composition, high TMR ratios were demonstrated for CMFS MTJs having (Mn + Fe)-rich CMFS electrodes. Therefore, it is important to experimentally investigate the origin of this dependence and the key factors affecting the half-metallicity of the quaternary Heusler alloy CMFS.

Given this background, in this chapter, the investigation of the effect of off-stoichiometry on the half-metallic character of quaternary Heusler alloy CMFS will be explained in detail. This investigation was done through studying the film composition dependence of the μ_s of series-A CMFS thin films, whose preparation and characterization was explained in chapter 2. Furthermore, we will analyze the experimentally observed results along with the first-principles density functional theoretical calculations.

3.1 Results and discussion

Figure 3.1 (a) plots the experimental μ_s at 10 K for series-A CMFS as a function of δ ranging from δ = 0.73 (β' = 0, $Co_2Mn_{0.73}Si_{0.84}$) to δ = 1.40 (β' = 0.67, $Co_2Mn_{0.73}Fe_{0.67}Si_{0.84}$), along with the Z_t–24 values. A μ_s much lower than the Z_t–24 value was observed for δ = 0.73 (β' = 0) film, i.e., a Mn-deficient CMS film. This result has been explained by the deviation from half-metallicity due to the existence of Co_{Mn} antisites for Mn-deficient CMS [36]. Importantly, by increasing the Fe composition β', μ_s increased and got closer to the Z_t–24 value with increasing δ, from δ = 0.73 (β' = 0) to δ = 1.30 (β' = 0.57), and μ_s for δ = 1.30 (β' = 0.57) was in good agreement with the half-metallic value, Z_t–24. This dependence of μ_s on δ in the range from δ = 0.73 (β' = 0) to δ = 1.30 (β' = 0.57) was similar to the dependence of μ_s on the Mn composition, α, in off-stoichiometric $Co_2Mn_\alpha Si$ films [36]. However, a further increase in δ from δ = 1.30 (β' = 0.57) to δ = 1.40 (β' = 0.67) resulted in a μ_s that is distinctly lower than its Z_t–24 value, indicating a deviation from half-metallicity in $Co_2Mn_{0.73}Fe_{0.67}Si_{0.84}$.

Figure 3.1 (b) compares the experimental μ_s with the theoretical m_{spin} for series-A CMFS films with various values of β' in $Co_2Mn_{0.73}Fe_{\beta'}Si_{0.84}$. Good agreement between μ_s and m_{spin} was obtained for the entire δ range from δ = 0.73 (β' = 0) to δ = 1.40 (β' = 0.67). The μ_s value of δ = 1.40 (β' = 0.67) was apparently lower than its Z_t–24, but it was well reproduced by the m_{spin} value. The overall agreement indicates that the proposed antisite-based SSFU compositions properly describe the SSFU compositions of off-stoichiometric quaternary CMFS of series A.

In chapter 1, Fig. 1.6 shows the δ dependence of the TMR ratio at 4.2 K of CMFS MTJs that have the corresponding series-A films as the lower and upper electrodes, as previously reported in Ref. [47]. We found a clear correspondence between the δ dependence of the TMR ratio at 4.2 K with that of the experimental μ_s. More specifically, MTJs that had CMFS films whose experimental μ_s got closer to the half-metallic Z_t–24 value exhibited higher TMR ratios at 4.2 K. A similar film composition dependence of the TMR ratio was observed at RT.

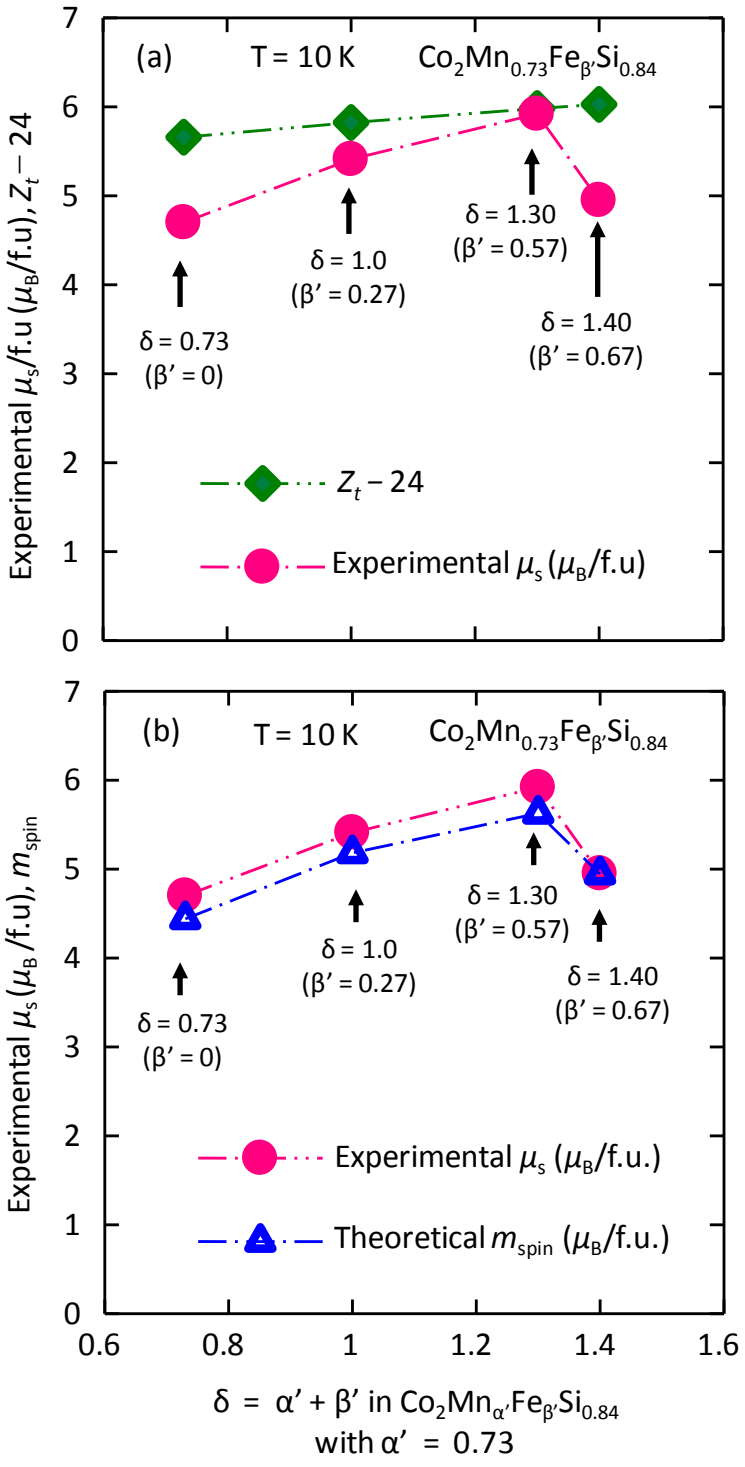

Fig. 3.1. (Mn+Fe) film composition dependence of the experimental saturation magnetization of series-A CMFS films at 10 K in comparison with (a) the Slater-Pauling value of Z_t–24 and (b) the theoretical total spin magnetic moment per formula unit.

Now let us discuss the origin of the film composition dependences of μ_s of series-A CMFS films and the TMR ratio of series-A CMFS MTJs. Figure 3.2 (a)−(d) shows the local DOS (LDOS) for Mn at its ordinary site ($Mn_{Mn/Fe}$), Fe at its ordinary site ($Fe_{Mn/Fe}$), Co at its ordinary site (Co_{Co}), and the $Co_{Mn/Fe}$ antisite for series-A CMFS, respectively. Here, the LDOS of $Mn_{Mn/Fe}$ features a wide half-metal gap for the minority-spin states around E_F over the entire range of β' investigated: from β' = 0 (δ = 0.73) to β' = 0.67 (δ = 1.40). Meanwhile, the LDOS of $Fe_{Mn/Fe}$ shows a finite density for the minority-spin states at E_F over the entire range. In contrast, the LDOS of the $Co_{Mn/Fe}$ antisite for δ-deficient CMFS with δ = 0.86 (β' = 0.13) and δ = 1.0 (β' = 0.27) had a peak in the minority-spin density of states (DOS) around E_F with an appreciable DOS similar to that of Mn-deficient CMS [36], corresponding to β' = 0 (δ = 0.73) in the plot. The critical δ value for which the $Co_{Mn/Fe}$ antisite disappears (δ_c) from the nominal SSFU composition of $Co_2Mn_{\alpha'}Fe_{\beta'}Si_{\beta}$ is given by $\delta_c = 2-\beta = 1.16$ for $\beta = 0.84$. Thus, the nominal SSFU compositions for δ = 1.30 (β' = 0.57) and δ = 1.40 (β' = 0.67) do not contain $Co_{Mn/Fe}$ antisites. In addition, the LDOS curve of Co at the ordinary site (Co_{Co}) for δ-deficient, δ = 0.86 (β' = 0.13) CMFS had a peak in the minority-spin DOS around E_F as did Mn-deficient, β' = 0.0 (δ = 0.73) CMS although the height was much smaller than that for $Co_{Mn/Fe}$. This result suggests that $Co_{Mn/Fe}$ antisites in (Mn + Fe)-deficient CMFS affect the electronic state of Co atoms at the ordinary sites in a similar way to in Mn-deficient CMS [36].

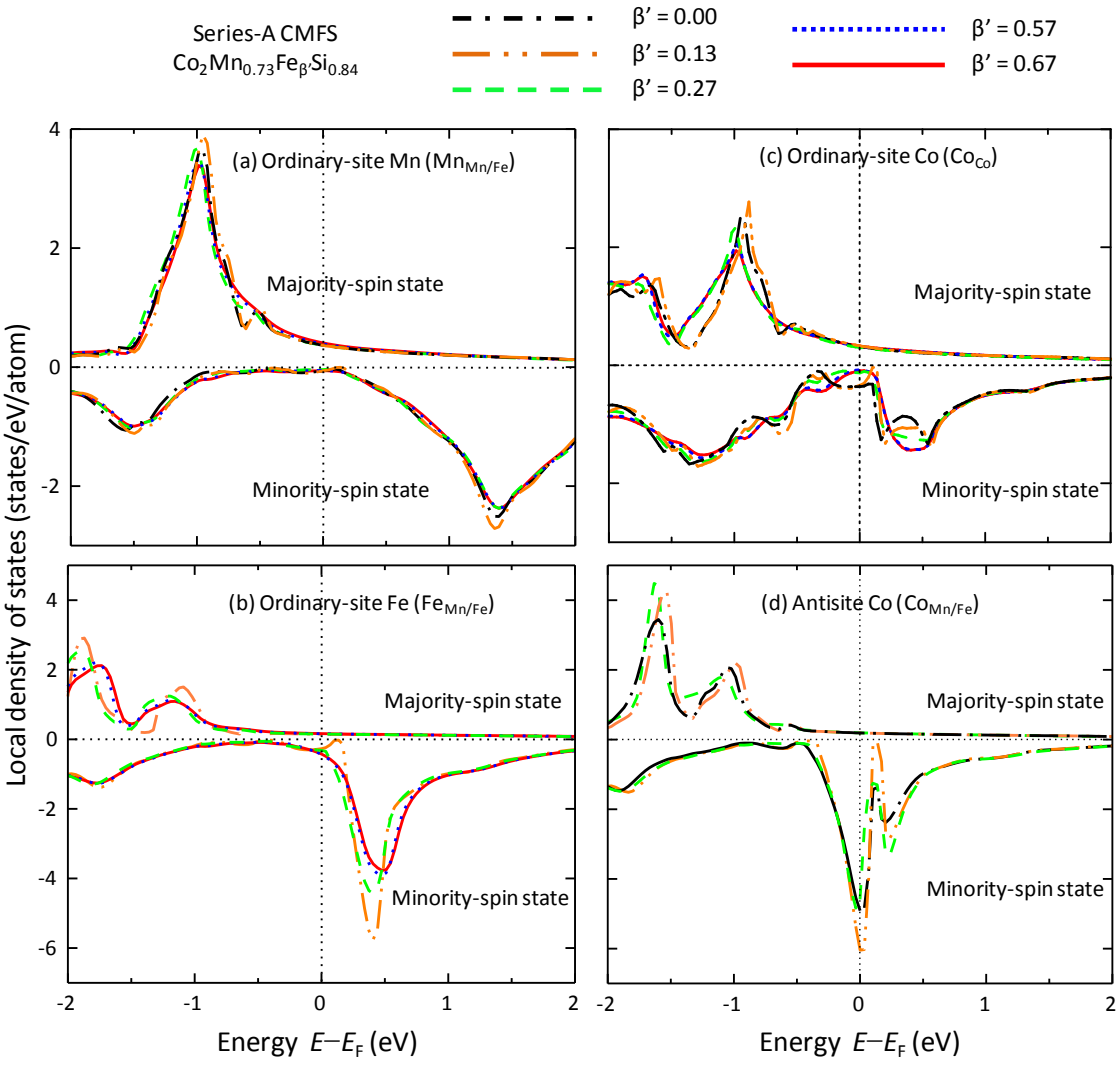

Fig. 3.2. Spin-projected LDOS per atom for (a) ordinary-site Mn ($Mn_{Mn/Fe}$), (b) ordinary-site Fe ($Fe_{Mn/Fe}$), (c) ordinary-site Co (Co_{Co}), and (d) $Co_{Mn/Fe}$ antisites for series-A CMFS ($Co_2Mn_{0.73}Fe_{\beta'}Si_{0.84}$).

Figure 3.3 plots the spin-projected total DOS of series-A CMFS ($Co_2Mn_{0.73}Fe_{\beta'}Si_{0.84}$) for various β'. The minority-spin total DOS curve of series-A CMFS with δ-deficient, δ = 0.86 (β' = 0.13) showed a characteristic peaked structure around E_F in the half-metal gap, with an appreciable DOS at the peak, like that of Mn-deficient, β' = 0 (δ = 0.73) CMS. This peak is due to the existence of the peak in the minority-spin LDOS of $Co_{Mn/Fe}$ around E_F described above. However, there was no peak in the minority-spin total DOS in the half-metal gap for the δ-deficient, δ = 1.0 (β' = 0.27) and δ-rich, δ = 1.30 (β' = 0.57) and δ = 1.40 (β' = 0.67) series-A CMFS, although a small, finite minority-spin DOS

remained around E_F in the half-metal gap. The disappearance of the peak for the $\delta = 1.0$ (β' = 0.27) CMFS can be ascribed to its reduced $Co_{Mn/Fe}$ ratio in the SSFU composition (Table III) compared with that for the more δ-deficient, $\delta = 0.86$ (β' = 0.13) sample, whereas the disappearance of the peak for the δ-rich, $\delta = 1.30$ (β' = 0.57) and $\delta = 1.40$ (β' = 0.67) samples can be explained by the disappearance of $Co_{Mn/Fe}$ antisites in their nominal SSFU compositions. The origin of the finite minority-spin DOS at E_F for the $\delta = 1.0$ (β' = 0.27) CMFS is due to the remaining $Co_{Mn/Fe}$ antisites in its SSFU composition. On the other hand, the origin of the finite minority-spin DOS at E_F for the δ-rich, $\delta = 1.30$ (β' = 0.57) and $\delta = 1.40$ (β' = 0.67) samples is due to the finite minority-spin LDOS of $Fe_{Mn/Fe}$ at E_F. Thus, the slightly lower μ_s and m_{spin} for the δ-deficient, $\delta = 1.0$ (β' = 0.27) CMFS than its Z_t−24 is ascribed to the reduced but still remaining $Co_{Mn/Fe}$ antisites and that μ_s is closer to its Z_t−24 value for the δ-rich, $\delta = 1.30$ (β' = 0.57) sample is due to suppression of $Co_{Mn/Fe}$ antisites. The origin of the distinctly lower μ_s and m_{spin} for $\delta = 1.40$ (β' = 0.67) CMFS than its Z_t−24 value is the increased Fe/(Mn+Fe) ratio and will be discussed in detail below.

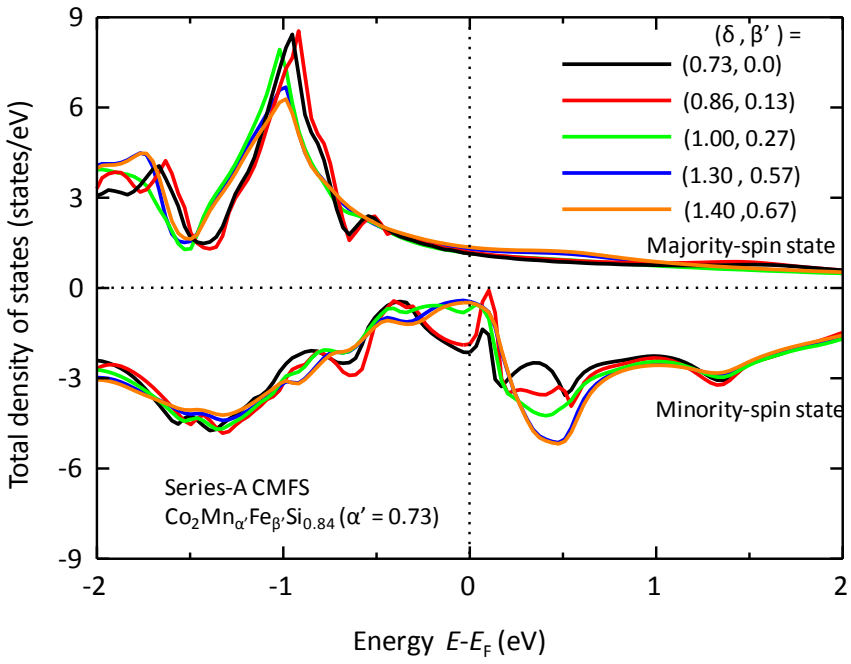

Fig. 3.3. Spin-projected total DOS per formula unit for series-A CMFS, or $Co_2Mn_{0.73}Fe_{\beta'}Si_{0.84}$ with a fixed α' of 0.73 in $Co_2Mn_{\alpha'}Fe_{\beta'}Si_{0.84}$ and various β' ranging from 0 to 0.67.

We theoretically calculated the δ dependence of the spin magnetic moments of Co, Mn, and Fe atoms at their respective ordinary site and antisite for series-A CMFS using the KKR-CPA method. Figure 3.4 shows the calculated spin magnetic moments of Mn, Fe, and Co at the nominal Mn/Fe sites, $m_{spin}(Mn_{Mn/Fe})$, $m_{spin}(Fe_{Mn/Fe})$, and $m_{spin}(Co_{Mn/Fe})$. The m_{spin} for $Co_{Mn/Fe}$ antisite is much smaller than those for Mn and Fe: $m_{spin}(Co_{Mn/Fe}) = 1.77\mu_B$ versus $m_{spin}(Mn_{Mn/Fe}) = 3.15\mu_B$, and $m_{spin}(Fe_{Mn/Fe}) = 2.93\mu_B$ for series-A CMFS with $\delta = 1.0$ (β' = 0.27). This result supports the conclusion that the origin of μ_s that is slightly lower than Z_t−24 for δ-deficient, $\delta = 1.0$ (β' = 0.27) CMFS is the existence of $Co_{Mn/Fe}$ antisites. Compared with μ_s of δ-deficient, $\delta = 1.0$ (β' = 0.27) CMFS, μ_s of δ-rich, $\delta = 1.30$ (β' = 0.57) CMFS is close to its Z_t−24 value. This behavior is consistent with the disappearance of Co_{Mn} antisites in the nominal SSFU composition.

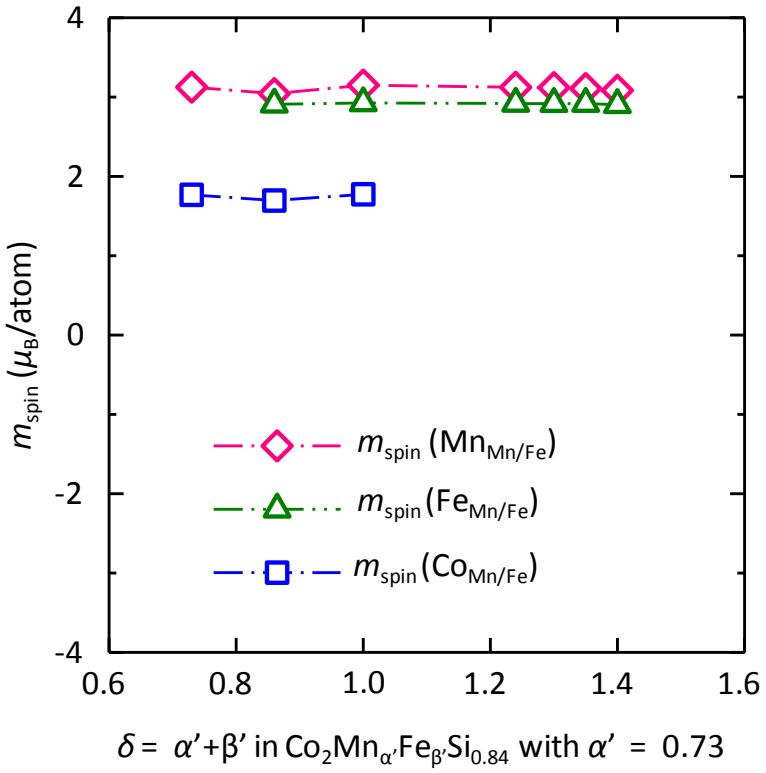

Fig. 3.4. Theoretically calculated local spin magnetic moments per atom, m_{spin}, for Mn, Fe and Co at the nominal Mn/Fe site ($Mn_{Mn/Fe}$, $Fe_{Mn/Fe}$, and $Co_{Mn/Fe}$).

Next, let us discuss the origin of μ_s that is lower than the half-metallic Z_t−24 value for heavily Fe-doped $\delta = 1.40$ ($\beta' = 0.67$). The total DOS of this Heusler alloy is plotted in Fig. 3.3 (shown by the orange solid line). From this plot we found that $\delta = 1.40$ ($\beta' = 0.67$) CMFS featured a narrower half-metal gap with rounded falling and rising edges of the minority-spin DOS at the top of the valence band and the bottom of the conduction band. Furthermore, $\delta = 1.40$ ($\beta' = 0.67$) had a finite DOS at E_F in the half-metal gap region. These features are due to the increased Fe atomic ratio (ξ) in the nominal Mn/Fe site in the type III SSFU composition for δ-rich CMFS, where ξ is determined as $\xi = \beta'/(\alpha' + \beta')$, and thus they were observed for $\delta = 1.30$ ($\beta' = 0.57$) and $\delta = 1.40$ ($\beta' = 0.67$) series-A CMFS that had relatively high ξ values ranging from 0.44 to 0.48. To be precise, the structure featuring a narrow half-metal gap region and a finite minority-spin DOS at E_F for the $\delta = 1.30$ ($\beta' = 0.57$) and $\delta = 1.40$ ($\beta' = 0.67$) CMFS should be called a quasi-half-metal gap. The finite minority-spin DOS at E_F in the quasi-half-metal gap for $\delta = 1.30$ ($\beta' = 0.57$) and $\delta = 1.40$ ($\beta' = 0.67$) is due to the finite LDOS of Fe at its ordinary site [Fig. 3.2 (b)].

The origin of the decrease in μ_s from its Z_t−24 value for heavily Fe-doped $\delta = 1.40$ ($\beta' = 0.67$) is the smaller local m_{spin} of ordinary-site Fe compared with that of ordinary-site Mn (Fig. 3.4) and the larger ξ of up to 0.48 for heavily Fe-doped $\delta = 1.40$ ($\beta' = 0.67$).

Now let us discuss the origin of the δ dependence of the TMR ratio at 4.2 K of series-A CMFS MTJs with $Co_2Mn_{0.73}Fe_{\beta'}Si_{0.84}$ electrodes in comparison with the results of the KKR-CPA calculations. To do this, we semiquantitatively compared the experimentally deduced tunneling spin polarizations, P_{exp}, with the theoretical spin polarizations, $P_{th}(sp)$ and $P_{th}(spd)$. We did so because a straightforward first-principles calculation of the TMR ratio for epitaxial MTJs with electrodes with off-stoichiometric compositions is not realistic because of the lack of translational symmetry in the electrodes. We compared P_{exp} with $P_{th}(sp)$ determined by considering only the contributions from s-, and p-orbital components to the majority- and minority-spin DOS at E_F, $D_M(sp)$ and $D_m(sp)$, respectively, for series-A CMFS electrodes. $P_{th}(sp)$ is defined as:

$$P_{th}(sp) = \frac{D_M(sd) - D_m(sp)}{D_M(sp) + D_m(sp)}. \qquad (3.1)$$

We also made a comparison between P_{exp} and $P_{th}(spd)$, the theoretical value that takes into consideration all the contributions from *s*-, *p*- and *d*-orbital components to the majority- and minority-spin DOS, $D_M(spd)$ and $D_m(spd)$. $P_{th}(spd)$ is defined as:

$$P_{th}(spd) = \frac{D_M(spd) - D_m(spd)}{D_M(spd) + D_m(spd)}. \qquad (3.2)$$

We estimated the tunneling spin polarization, P_{exp}, which is involved in electron tunneling in MTJs, from the TMR ratio at a low temperature, 4.2 K, by using the Julliere model [45] with a modified interpretation from the original one, as described below. The original Julliere model was derived by assuming that the tunneling matrix element for tunneling from the state characterized by a crystal momentum $\boldsymbol{k}$ to $\boldsymbol{k}$' at E_F is independent of $\boldsymbol{k}$ and $\boldsymbol{k}$' and is constant for any tunneling process from $\boldsymbol{k}$ to $\boldsymbol{k}$'. As a result, the original model takes into account all majority- and minority-spin DOS at E_F in the spin polarization *P*. However, the tunneling probability from $\boldsymbol{k}$ to $\boldsymbol{k}$' is strongly dependent on the wave function symmetry in epitaxial, single-crystalline MTJs [56,57]. Accordingly, in epitaxial MgO-based MTJs, including CMS/MgO-based MTJs [58], where the transverse crystal momentum of an electron is conserved for tunneling, an electron with a Δ_1 symmetry wave function at E_F has a higher transmission probability. To make a semiquantitative comparison, we assumed that only the electronic states of the majority- and minority-spin bands at E_F that satisfy the condition of coherent tunneling contribute to tunneling in CMS/MgO- and CMFS/MgO-based MTJs at 4.2 K. Furthermore, we assumed that all these electronic states have an equal transmission probability. These assumption lead to the same expression for the TMR ratio as the Julliere model, i.e.,

$$\mathrm{TMR} = \frac{2P_{exp}{}^2}{1 - P_{exp}{}^2}, \qquad (3.3)$$

where the tunneling spin polarization P_{exp} corresponds to a spin polarization determined by the majority- and minority-spin DOS at E_F, effectively contributing to coherent tunneling. Here, we assumed that the lower and upper electrodes had an identical tunneling spin polarization.

The experimental dependence of P_{exp} on δ for series-A CMFS with $Co_2Mn_{0.73}Fe_{\beta'}Si_{0.84}$ electrodes is compared with those of $P_{th}(sp)$ and $P_{th}(spd)$ in Fig. 3.5. The P_{exp} values that increased with increasing δ from $\delta = 0.73$ ($\beta' = 0$) to $\delta = 1.35$ ($\beta' = 0.62$) were semiquantitatively well explained by the $P_{th}(sp)$ values. These CMFS electrodes showed P_{exp} values, typically $P_{exp} = 0.946$ for $\delta = 1.35$ ($\beta' = 0.62$), higher than those of the Mn-deficient CMS electrode with $\delta = 0.73$ ($\beta' = 0$), which showed a lower P_{exp} of 0.87. In more detail, P_{exp} significantly increased from $\delta = 0.73$ ($\beta' = 0$) to $\delta = 1.24$ ($\beta' = 0.51$). After that, it slightly increased, reaching a maximum at $\delta = 1.35$ ($\beta' = 0.62$), and then decreased upon a further increase in δ to $\delta = 1.40$ ($\beta' = 0.67$). This experimental behavior was well reproduced by $P_{th}(sp)$, although there was a slight difference in the δ value that gave the highest P value; i.e., $P_{th}(sp)$ increased from $\delta = 0.73$ ($\beta' = 0$) to $\delta = 1.24$ ($\beta' = 0.51$), after which it gradually decreased upon a further increase in δ to $\delta = 1.40$ ($\beta' = 0.67$). The significant increase in P_{exp} from $P_{exp} = 0.871$ for $\delta = 0.73$ ($\beta' = 0$) to $P_{exp} = 0.945$ for $\delta = 1.24$ ($\beta' = 0.51$) is due to the suppression of $Co_{Mn/Fe}$ antisites in the SSFU composition, with increasing δ in going from a (Mn + Fe)-deficient composition to a (Mn + Fe)-rich one. However, the decrease in P_{exp} from $\delta = 1.35$ ($\beta' = 0.62$) to $\delta = 1.40$ ($\beta' = 0.67$) is due to the influence of the increasing Fe/(Mn+Fe) atomic ratio on the half-metallicity. This slight difference in the dependence of P_{exp} and $P_{th}(sp)$ on δ is ascribed to the following reasons: first, there remained a small amount of residual $Co_{Mn/Fe}$ antisites in the actual SSFU composition for CMFS that had the nominally $Co_{Mn/Fe}$ antisite-free type III SSFU composition, and the residual $Co_{Mn/Fe}$ antisites were further suppressed with a (Mn + Fe)-rich composition. Second, the increased Fe/(Mn + F e) atomic ratio degraded the half-metallicity, as discussed above. Thus, there should be a competition between these two effects that results in a slight difference in the dependences of P_{exp} and $P_{th}(sp)$ on δ.

However, the P_{exp} values for various δ were significantly different from $P_{th}(spd)$. For the negative $P_{th}(spd)$ of $\delta = 0.73$ ($\beta' = 0$), its absolute value should be compared with P_{exp}; but this comparison still results in a big difference between P_{exp} and the absolute value of $P_{th}(spd)$ for $\delta = 0.73$ ($\beta' = 0$). A comparison of P_{exp} with $P_{th}(sp)$ and $P_{th}(spd)$ for series-A CMFS indicates that the tunneling spin polarization, which is responsible for tunneling in CMFS MTJs in which coherent tunneling is dominant, is mainly explained by $P_{th}(sp)$. This finding is in agreement with the previous findings for CMS MTJs [36].

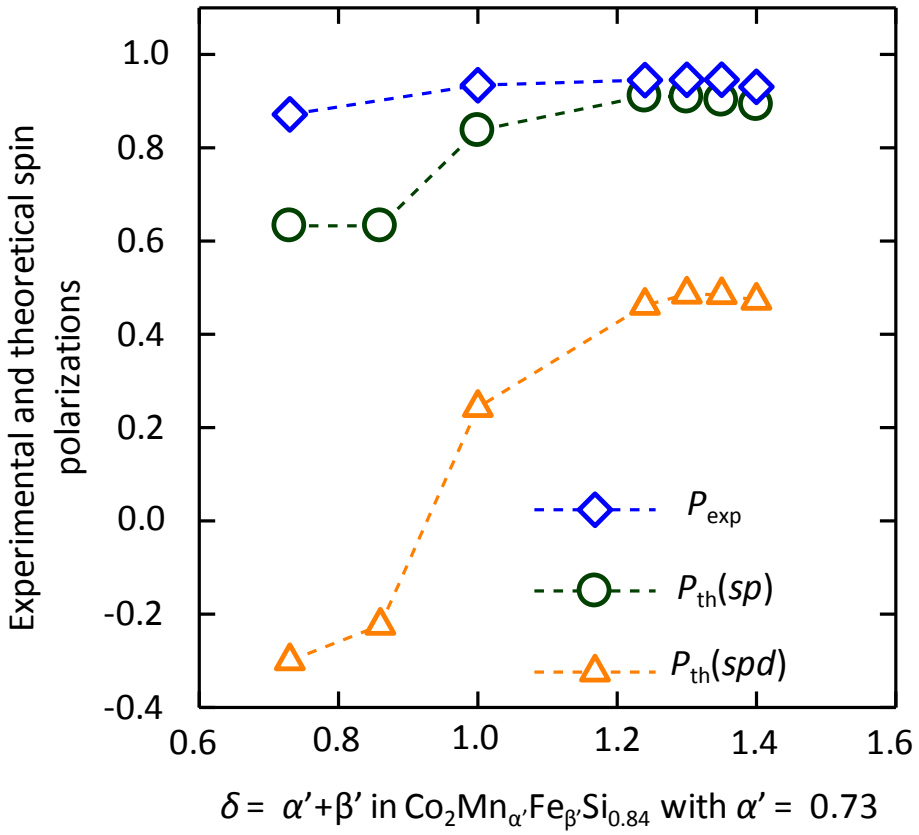

Fig. 3.5. Experimental tunneling spin polarizations, P_{exp}, deduced from the TMR ratio at 4.2 K using a modified Julliere model and two kinds of theoretical spin polarizations, $P_{th}(sp)$ and $P_{th}(spd)$, obtained by the KKR-CPA calculations as a function of $\delta = \alpha'+\beta'$ with $\alpha' = 0.73$ for series-A CMFS.

3.2 Summary

In summary, we investigated how the film compositions in terms of off-stoichiometry and Fe/(Mn+Fe) atomic ratios affect the half-metallicity of the quaternary Heusler alloy CMFS by analyzing the saturation magnetization per formula unit, μ_s, of CMFS thin films with various Mn and Fe compositions and the TMR ratios of CMFS MTJs and by performing first-principles calculations. The μ_s that is lower than the half-metallic Z_t-24 for (Mn+Fe)-deficient CMFS films was explained by the spin magnetic moment of $Co_{Mn/Fe}$ being smaller than those of Mn and Fe at their nominal Mn/Fe site. Furthermore, the film composition dependence of the TMR ratio was well explained by the theoretical spin polarizations derived from only the *s*- and *p*-orbital components of the DOS at E_F. Analyses of the experimental μ_s and the TMR ratios, together with first-principles calculations for off-stoichiometric CMFS, clarified that $Co_{Mn/Fe}$ antisites in quaternary CMFS are detrimental to half-metallicity, similar way to in ternary CMS. It was also found that (Mn+Fe)-rich compositions in CMFS led to higher TMR ratios through suppression of harmful $Co_{Mn/Fe}$ antisites. Furthermore, it was indicated that the Fe/(Mn+Fe) ratio influenced the half-metallicity, in particular for the relatively large Fe/(Mn+Fe) ratio.

Chapter 4

Origin of the giant TMR ratios obtained for CMFS MTJs

In section 1.1. of chapter 1, a detailed explanation of the influence of film composition on the TMR ratio of two series of CMFS MTJs was given. By investigating the Fe composition dependence of the TMR ratio of CMFS MTJs that have $Co_2(Mn_{\alpha'}Fe_{\beta'})Si_{0.84}$ electrodes with a constant ($\alpha' + \beta'$) value of 1.40 (series-B CMFS MTJs), giant TMR ratios of 2610% at 4.2 K and 429% at 290 K were demonstrated for the MTJs with Mn-rich, lightly Fe-doped CMFS ($Co_2Mn_{1.24}Fe_{0.16}Si_{0.84}$) electrodes [47]. As noted previously, these TMR ratios are significantly higher than those obtained for CMS MTJs that have Mn-rich CMS electrodes [15]. However, the origin of the giant TMR ratio obtained for CMFS MTJs with Mn-rich, lightly Fe-doped CMFS electrodes has yet to be fully understood.

Given this background, in this chapter, we will discuss how the half-metallicity of (Mn+Fe)-rich CMFS depends on the Fe composition. Then, we will discuss the origin of the giant TMR ratio of CMFS MTJs with Mn-rich, lightly Fe-doped CMFS electrodes. We investigated μ_s of series-B CMFS, i.e., (Mn+Fe)-rich $Co_2Mn_{\alpha'}Fe_{\beta'}Si_{0.84}$ alloy that have a fixed $\delta = \alpha' + \beta' = 1.40$ with various combinations of α' and β' ranging from $\beta' = 0$ ($\alpha' = 1.40$) to $\beta' = 0.67$ ($\alpha' = 0.73$) (Table IV). Furthermore, we experimentally investigated the TMR ratios of CMFS MTJs with Mn-rich, lightly Fe-doped CMFS electrodes as a function of α' in $Co_2Mn_{\alpha'}Fe_{0.16}Si_{0.84}$ (series-C CMFS) for a δ-rich range from $\delta = 1.30$ ($\alpha' = 1.14$) to $\delta = 1.40$ ($\alpha' = 1.24$) and compared the results with those of the previously reported CMFS MTJs with series-A and series-B CMFS electrodes [47]. Finally, in this chapter we will explain the tunneling spectroscopy analysis which was done for CMFS MTJs to extract the half-metallic electronic structure of the CMFS electrode having a Mn-rich, lightly Fe-doped composition. We will also discuss the respective tunneling paths for P and AP responsible for the appearance of the characteristic voltages in dI/dV versus V characteristics to be analysed to extract the half-metallic band-gap information.

4.1 Investigation via μ_s and TMR ratio

In this section, we will discuss how the half-metallicity of (Mn+Fe)-rich CMFS depends on the Fe composition by studying the saturation magnetization per formula unit in combination with first-principles theoretical calculations. Then, we will discuss the origin of the giant TMR ratio of CMFS MTJs with Mn-rich, lightly Fe-doped CMFS electrodes by investigating the Fe-composition dependence of series-C CMFS MTJs.

Figure 4.1 compares μ_s at 10 K with Z_t−24 and m_{spin} obtained by the KKR-CPA calculations for series-B CMFS films with β' ranging from β' = 0 (α' = 1.40) to β' = 0.67 (α' = 0.73). The β' = 0.67 (α' = 0.73) CMFS belongs to both series A and series B, as noted in chapter 3. It was found that μ_s of β' = 0.16 (α' = 1.24), i.e., $Co_2Mn_{1.24}Fe_{0.16}Si_{0.84}$, in which a small amount of Mn was replaced with Fe in $Co_2Mn_{1.40}Si_{0.84}$, was close to its Z_t−24 value. Thus, the good agreement between μ_s and Z_t−24 for these Heusler alloys indicates that their electronic states are close to being half-metallic in terms of μ_s. Furthermore, their μ_s values were close to the theoretical m_{spin} values. However, the experimental μ_s for β' = 0 (α' = 1.40), i.e., Mn-rich $Co_2Mn_{1.40}Si_{0.84}$, was evidently lower than its Z_t−24 value, while its theoretical m_{spin} value was in rather good agreement with Z_t−24. Similarly, as mentioned in chapter 3, μ_s of heavily Fe-doped β' = 0.67 (α' = 0.73) was significantly lower than its Z_t−24 value, while m_{spin} reproduced the experimental μ_s. The origin of this behavior has already been discussed in chapter 3.

As explained in section 1.1 of chapter 1, Figure 1.7 shows the TMR ratios at 4.2 K of CMFS MTJs that have series-B CMFS films as the lower and upper electrodes as a function of β' [47], along with Z_t−24 values on the top axis. Two characteristic results can be seen. Firstly, the TMR ratio significantly increases from β' = 0 (α' = 1.40) to β' = 0.16 (α' = 1.24) (region a). Indeed, it increases from 1670% at 4.2 K (336% at 290 K) for β' = 0 (α' = 1.40), i.e., $Co_2Mn_{1.40}Si_{0.84}$, to 2610% at 4.2 K (429% at 290 K) for β' = 0.16 (α' = 1.24), i.e., Mn-rich, lightly Fe-doped $Co_2Mn_{1.24}Fe_{0.16}Si_{0.84}$. Thus, this significant increase in the TMR ratio of β' = 0.16 (α' = 1.24) compared with that of β' = 0 (α' = 1.40) coincides with the recovery of μ_s to a value close to the half-metallic Z_t−24 for β' = 0.16 (α' = 1.24). This result is a key to understanding the origin of the giant TMR ratio of the MTJs with Mn-rich, lightly Fe-doped CMFS electrodes. Second, the TMR ratio at 4.2 K of the MTJs with series-B films gradually decreases from β' = 0.16 (α' = 1.24) to β' =

0.67 (α' = 0.73) (region b). Indeed, it gradually decreases from 2610% at 4.2 K (429% at 290 K) for Mn-rich, lightly Fe-doped β' = 0.16 (α' = 1.24) to 1290% at 4.2 K (304% at 290 K) for heavily Fe-doped β' = 0.67 (α' = 0.73). The drop in the TMR ratio for β' = 0.67 (α' = 0.73) corresponds to a μ_s that is lower than its Z_t–24.

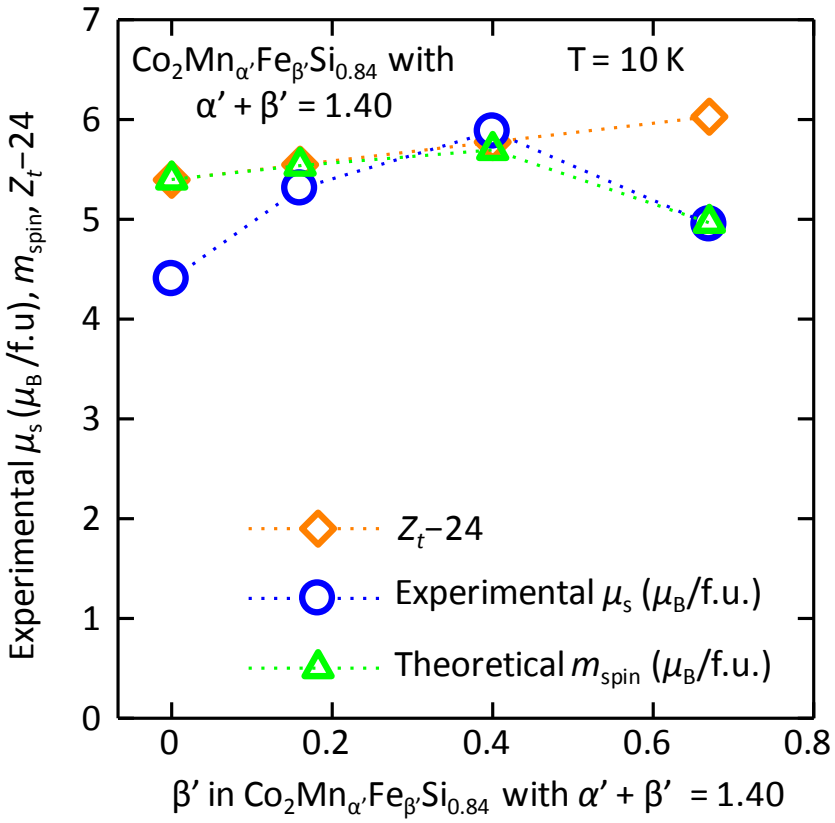

Fig. 4.1. The (Mn+Fe) film composition dependence of the experimental saturation magnetization of series-B CMFS films at 10 K in comparison with the Slater-Pauling value of Z_t–24 and theoretically calculated total spin magnetic moment, m_{spin}.

Figure 4.2 shows the spin-projected total DOS curves of series-B CMFS with a fixed $\delta = \alpha' + \beta' = 1.40$ and various α' and β' ranging from α' = 0.73 (β'= 0.67) to α' = 1.40 (β'= 0). The KKR-CPA calculations predicted that Mn-rich, lightly Fe-doped CMFS, i.e., α'=1.24 (β'=0.16), retains a distinct half-metallic gap structure characterized by sharp falling and rising edges of the minority-spin DOS at the top of the valence band and the bottom of the conduction band, although the minority-spin DOS in the half-metal gap region slightly increased with increasing energy across E_F, resulting in a small finite minority-spin DOS at E_F. However, the KKR-CPA calculations for $Co_2Mn_{1.40}Si_{0.84}$ (α' =

1.40, β' = 0) based on the Co_{Mn}-antisite-free SSFU composition (Table IV) indicated a more complete half-metallic structure, as has been predicted for Mn-rich CMS with type III SSFU composition [36,50]. The theoretically predicted half-metallic character of α' = 1.24 (β' = 0.16) CMFS is consistent with the experimentally observed giant TMR ratio and the μ_s being close to its Z_t−24 value. The minority-spin DOS at E_F gradually increased when β' was further increased from β' = 0.16 (ξ = 0.11) to β' = 0.67 (ξ = 0.48), as shown in Fig. 4.2. This is associated with the more rounded rising edge at the bottom of the minority-spin conduction band for CMFS with increased ξ, and its origin can be mainly ascribed to the LDOS curve of Fe at the ordinary Mn/Fe site (not shown).

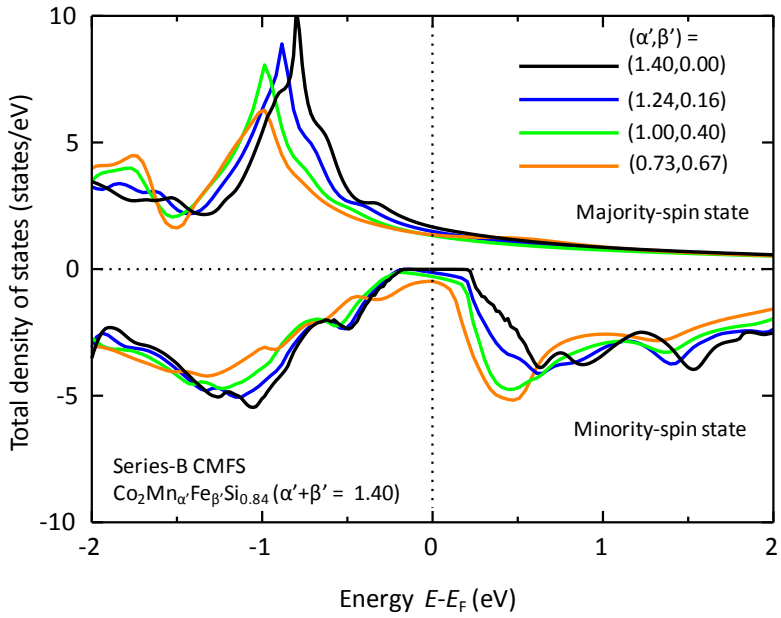

Fig. 4.2. Spin-projected total DOS per formula unit for series-B CMFS, or $Co_2Mn_{\alpha'}Fe_{\beta'}Si_{0.84}$ with a fixed $\delta = \alpha'+\beta' = 1.40$ and various α' and β' ranging from $\alpha' = 0.73$ ($\beta' = 0.67$) to $\alpha' = 1.40$ ($\beta' = 0$).

To compare the experimentally obtained TMR ratios for various β' values with the theoretically derived spin polarizations for series-B CMFS, we plot P_{exp}, along with $P_{th}(sp)$ and $P_{th}(spd)$, as a function of β' in Fig. 4.3, where the P_{exp} values are estimated from the TMR ratios at 4.2 K using the Julliere model with the modified interpretation as discussed in chapter 3. The figure shows that P_{exp} for the entire β' range from β' = 0 (α' = 1.40) to β' = 0.67 (α' = 0.73) is generally in good agreement with $P_{th}(sp)$, as in the case of series-A CMFS. In contrast, the difference between P_{exp} and $P_{th}(spd)$ is significant; in particular, the degree of the difference increases as P_{exp} decreases. Summarizing the comparison of

P_{exp} with $P_{th}(sp)$ and $P_{th}(spd)$ for series-A and series-B CMFS, we find that P_{exp} for highly spin-polarized CMFS electrodes is semiquantitatively in agreement with $P_{th}(sp)$ but not $P_{th}(spd)$. This finding is reasonable because tunneling in epitaxial MgO-based MTJs is dominated by coherent tunneling of electrons of Δ_1 symmetry states of CMFS in which itinerant s and p(z) states rather than $d(3z^2\text{-}r^2)$ states are the main components. Note that the agreement between P_{exp} and $P_{th}(sp)$ was better for electrodes with higher P_{ex}.

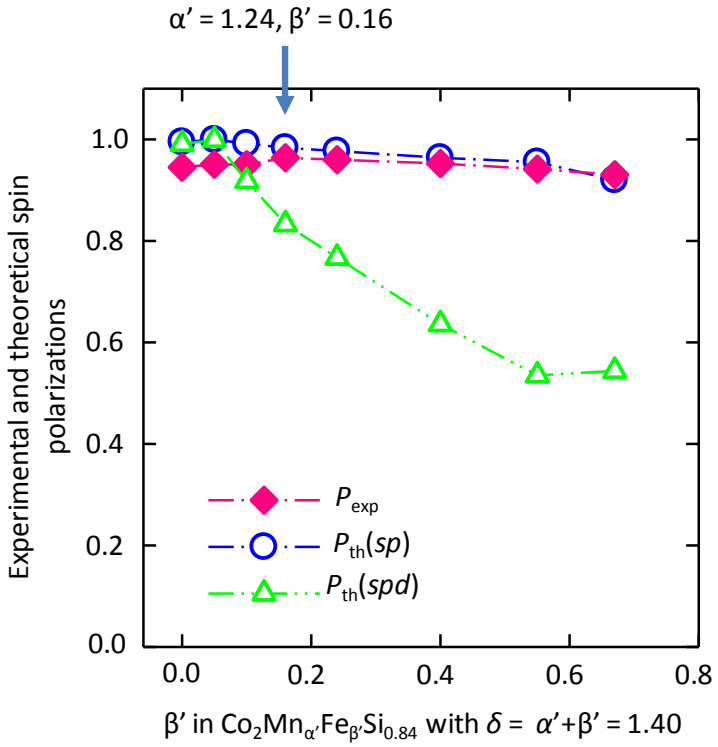

Fig. 4.3. Experimental spin polarizations, P_{exp}, deduced from the TMR ratio at 4.2 K using a modified Julliere model and two kinds of theoretical spin polarizations, $P_{th}(sp)$ and $P_{th}(spd)$, obtained by the KKR-CPA calculations as a function of β' with $\alpha'+\beta' = 1.40$ for series-B CMFS.

Next, let us compare the β' dependence of P_{exp} with that of $P_{th}(sp)$ in more detail, in particular for a lightly Fe-doped composition range (region a in Fig. 1.7). The high P_{exp} of 0.964 corresponding to a giant TMR ratio of 2610% at 4.2 K for α' = 1.24 (β' = 0.16) CMFS was close to the $P_{th}(sp)$ of 0.984. This high level of agreement is due to the theoretically predicted half-metal gap. In contrast, the lower P_{exp} of 0.945 (the TMR ratio of 1670% at 4.2 K) for $Co_2Mn_{1.40}Si_{0.84}$ (α' = 1.40, β' = 0) was in apparent disagreement with that of the theoretically predicted spin polarization of almost 100%. Indeed, the

KKR-CPA calculations predicted $P_{th}(sp) = 0.995$ and $P_{th}(spd) = 0.991$ due to the more complete half-metal gap for (α' = 1.40, β' = 0). Summarizing the experimental results on μ_s and the TMR ratio, we conclude that although the electronic state of Mn-over-rich CMS with $\alpha > \alpha_c$ ($Co_2Mn_{1.40}Si_{0.84}$ that have $\alpha = 1.40$) slightly deviated from the theoretically predicted half-metallic Slater-Pauling value of Z_t−24, the Mn-rich, lightly Fe-doped CMFS with $\delta > \alpha_c$ ($Co_2Mn_{1.24}Fe_{0.16}Si_{0.84}$ that have $\delta = 1.40$) retained the half-metallic state. Here α_c is the critical Mn composition over which the TMR ratio of CMS MTJs showed a decrease. We have supposed that the origin of the inconsistency between the experimental and the theoretical results for Mn-over-rich CMS with $\alpha > \alpha_c$ is the slight deviation of the SSFU composition from the predicted Co_{Mn}-antisite-free SSFU composition for CMS with $\alpha > \alpha_c$ and that the actual SSFU composition for CMS with $\alpha > \alpha_c$ had a certain amount of Co_{Mn} antisites that reappeared [36]. The μ_s that is lower than Z_t−24 and the decreased TMR ratio for $Co_2Mn_{1.40}Si_{0.84}$ can be explained by this supposition. The origin of this deviation has been assumed to be the appearance of a second phase such as antiferromagnetic Mn_3Si with a Neel temperature of 25 K [36,55], although it has not been experimentally confirmed. The experimentally demonstrated half-metallic character of Mn-rich, lightly Fe-doped CMFS indicates the suppression of the deviation of the SSFU composition from the proposed Co_{Mn}-antisite-free SSFU composition for Mn-rich CMS, even with $\alpha > \alpha_c$, by replacing a small amount of Mn by Fe. Thus, the significant increase in the TMR ratio with increasing β' in a small β' range from β' = 0 (α' = 1.40) to β' = 0.16 (α' = 1.24) in the series-B CMFS MTJs [region a in Fig. 1.7] can be explained by the recovery of the half-metallic electronic state via the recovery of the $Co_{Mn/Fe}$-antisite-free type III SSFU composition induced by replacing a small amount of Mn with Fe. However, this idea is not sufficient to explain why the α' = 1.24 (β' = 0.16) CMFS MTJ had a significantly higher TMR ratio compared with the highest TMR ratio that the Mn-rich CMS MTJs exhibited [14,47].

To further clarify the origin of the giant TMR ratio for Mn-rich, lightly Fe-doped CMFS, we adopted a more systematic approach to lightly Fe-doped CMFS MTJs and investigated the dependence of their TMR ratio on the film composition. In this approach, we investigated CMFS MTJs with lightly Fe-doped CMFS electrodes by systematically increasing α' with a fixed β' = 0.16. Figure 4.4 (a) and (b) shows the TMR ratios at 4.2 and 290 K of CMFS MTJs, respectively, with Mn-rich, lightly Fe-doped (β' = 0.16)

$Co_2Mn_{\alpha'}Fe_{0.16}Si_{0.84}$ electrodes (series-C CMFS) as a function of α' ranging from α' = 1.14 (δ = 1.30) to α' = 1.24 (δ = 1.40). For the sake of comparison, the figures also show the TMR ratios at 4.2 and 290 K of identically prepared CoFe-buffered CMS MTJs that have $Co_2Mn_{\alpha}Si_{0.84}$ electrodes as a function of α ranging from 0.73 to 1.40 [47]. The TMR ratio of CMS MTJs increased with α to 2110% at 4.2 K and 366% at 290 K for α = 1.30; beyond $\alpha_c \sim 1.33$, i.e., the critical Mn composition in the CMS series of $Co_2Mn_{\alpha}Si_{0.84}$, it decreased to 1670% at 4.2 K and 336% at 290 K for α = 1.40. The TMR ratios of the δ = 1.30 (β' = 0.16) CMFS MTJ (2110% at 4.2 K and 366% at 290 K) were almost equal to those obtained for the α = 1.30 CMS MTJ. Most importantly, we found an increase in the TMR ratio for CMFS MTJs with lightly Fe-doped $Co_2Mn_{\alpha'}Fe_{0.16}Si_{0.84}$ when δ was increased beyond 1.30 to δ = 1.40. This resulted in significantly high TMR ratios of 2610% at 4.2 K and 429% at 290 K for the CMFS MTJ with α' = 1.24 and β' = 0.16 (δ = 1.40). This dependence was in sharp contrast to the decrease in the TMR ratio for CMS MTJs when α was larger than α_c.

The increase in the TMR ratio with α' in the series-C lightly Fe-doped CMFS is on the extended line of the increase in the TMR ratio for CMS MTJs (Fig. 4.4). The increase in the TMR ratio with increasing α for CMS MTJs with $Co_2Mn_{\alpha}Si_{\beta}$ (β is about 1.0) has been explained by a decrease in Co_{Mn} antisites with increasing α in the Mn-deficient composition region ($\alpha < 2-\beta$) and by further suppression of residual Co_{Mn} antisites in the nominally Co_{Mn}-antisite-free type III SSFU composition ($\alpha > 2-\beta$) by further increasing α [13,36]. The α = 1.24 and α = 1.30 CMS electrodes featured the Co_{Mn}-antisite-free type III SSFU compositions. The first-principles calculations have predicted almost 100% spin polarization for such CMS featuring the Co_{Mn}-antisites-free type III SSFU composition [36,40]. Indeed, the KKR-CPA calculations predicted $P_{th}(sp)$ values of about 0.995 and $P_{th}(spd)$ of about 0.991 for these CMS electrodes [36].

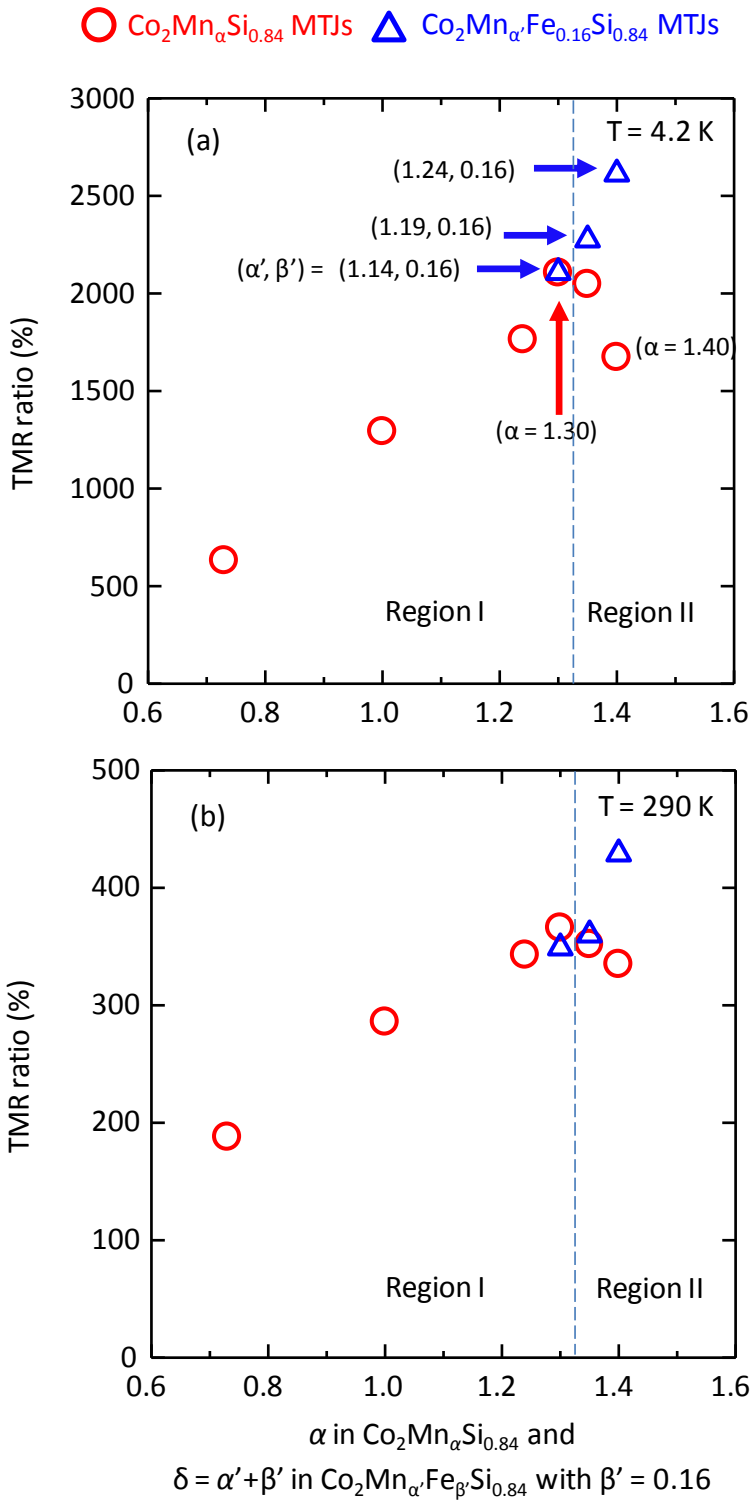

Fig. 4.4. TMR ratios at (a) 4.2 K and (b) 290 K for CMFS MTJs as a function of $\delta = \alpha' + \beta'$ in $Co_2Mn_{\alpha'}Fe_{\beta'}Si_{0.84}$ electrodes with $\beta' = 0.16$ ranging from 1.30 ($\alpha' = 1.14$) to 1.40 ($\alpha' = 1.24$). TMR ratios at (a) 4.2 K and (b) 290 K for identically fabricated CMS MTJs as a function of α in $Co_2Mn_{\alpha}Si_{0.84}$ electrode are shown for comparison [47].

The total DOS curves of series-C CMFS (α' = 1.14, 1.19, and 1.24), one of which, for α' = 1.24 (δ = 1.40), was shown in Fig. 4.2, are almost identical for the entire α' range from α' = 1.14 (δ = 1.30) to α' = 1.24 (δ = 1.40) and commonly show a distinct half-metal gap, as described above for δ =1.40 (α' = 1.24). These half-metal gap structures led to the $P_{th}(sp)$ values being close to the half-metallic value and almost constant for series-C CMFS, ranging from 0.984 for δ = 1.30 (α' = 1.14) to 0.987 for δ = 1.40 (α' = 1.24). Thus, the experimentally observed increase in the TMR ratio of CMS MTJs from α = 1.24 (TMR ratio of 1790% at 4.2 K, corresponding to P_{exp} = 0.948) to α = 1.30 (TMR ratio of 2110%, P_{exp} = 0.956) and the continuous increase in the TMR ratio of series-C CMFS from δ = 1.30 (α' = 1.14) (TMR ratio of 2110%, P_{exp} = 0.956) to δ = 1.40 (α' = 1.24) (TMR ratio of 2610%, P_{exp} = 0.964) cannot be explained by the almost constant half-metallic $P_{th}(sp)$ values derived from the KKR-CPA calculations based on the nominal SSFU compositions for CMS with α ranging from 1.24 to 1.30 and for series-C CMFS. The observed increase in the TMR ratio should be explained by another factor that is not included in the SSFU compositions. The enhanced TMR ratio obtained by increasing α for CMS and by increasing δ in lightly Fe-doped CMFS suggests an identical origin, i.e., the suppression of residual Co_{Mn} antisites in CMS or $Co_{Mn/Fe}$ antisites in CMFS by increasing the Mn ratio with respect to Co in the nominal type III SSFU compositions. This idea is the same as that for Mn-rich CMS [13,36,55]. The residual Co_{Mn} antisite for CMS or lightly Fe-doped CMFS is not taken into account in the type III, Co_{Mn}-antisite-free SSFU composition model. However, the further increase in the TMR ratio for the Mn-rich composition in CMS and lightly Fe-doped CMFS suggests that detrimental Co_{Mn} antisites are hard to avoid in experimentally prepared films, even with a stoichiometric composition or Mn-rich composition, but that they can be reduced by enriching the compositions with more Mn. However, there is a certain critical Mn composition for CMS [13,36]. This paper indicated that the critical Mn composition for CMS became larger as a result of replacing a small amount of Mn with Fe. Accordingly, a further reduction in the residual $Co_{Mn/Fe}$ antisites occurred for CMFS with δ being larger than α_c in Mn-rich CMS. Thus, we conclude that enhanced half-metallicity due to further reduction of residual $Co_{Mn/Fe}$ antisites is the origin of the giant TMR ratio of CMFS MTJs with Mn-rich, lightly Fe-doped CMFS electrodes.

Finally, let us discuss the origin of the gradual decrease in the TMR ratio with increasing β' for series-B CMFS in region b of Fig. 1.7. The P_{exp} values derived from the TMR ratios at 4.2 K for region b ranging from β' = 0.16 (α' = 1.24) to β' = 0.67 (α' = 0.73) were in good agreement with $P_{th}(sp)$ obtained from the KKR-CPA calculations. The gradual decrease in P_{exp} with the increasing Fe/(Mn+Fe) atomic ratio, ξ, in this region was well reproduced by the first-principles calculations. P_{exp} gradually decreased with increasing β' from P_{exp} = 0.964 (TMR ratio at 4.2 K = 2610%) for β' = 0.16 (α' = 1.24, corresponding to ξ = 0.11) to P_{exp} = 0.931 (TMR ratio at 4.2 K = 1290%) for β' = 0.67 (α' = 0.73, corresponding to ξ = 0.48). The total DOS curves showed that the most enhanced half-metallic electronic state among CMFS of region b [Fig.1.7] is for lightly Fe-doped β' = 0.16 (α' = 1.24). The minority-spin DOS at E_F gradually increased with increasing ξ. This is due to the more rounded rising edge of the minority-spin DOS at the bottom of the conduction band with increasing ξ and the E_F position crossing this rounded rising edge region. This resulted in the narrower half-metal gap for β' = 0.67 (α' = 0.73) that has the highest ξ = 0.48 among series-B CMFS. Furthermore, the majority-spin DOS at E_F gradually decreased with increasing ξ. These factors led to the gradual decrease in $P_{th}(sp)$ with increasing ξ.

4.2 Half-metallic electronic structure of Mn-rich, lightly Fe-doped CMFS

In this section, we will discuss how the half-metallic electronic structure of the quaternary Heusler alloy $Co_2Mn_{1.24}Fe_{0.16}Si_{0.84}$ is deduced experimentally from the dI/dV versus V characteristics for parallel (P) and antiparallel (AP) magnetization alignments. We will also discuss the respective tunneling paths for P and AP responsible for the appearance of the characteristic voltages in the dI/dV versus V characteristics to be analysed to extract the half-metallic band-gap information.

Figure 4.5 (a) and (b) shows the normalized differential conductances for P (G_P) and AP (G_{AP}) magnetization alignments of a $Co_2Mn_{1.24}Fe_{0.16}Si_{0.84}$/MgO/ $Co_2Mn_{1.24}Fe_{0.16}Si_{0.84}$ MTJ. The appearance of the characteristic voltages, V_{c1} for P and V_{c2} for AP, in the dI/dV versus V characteristics where the dI/dV values start to increase from the baseline suggests the existence of the half-metal gap [77].

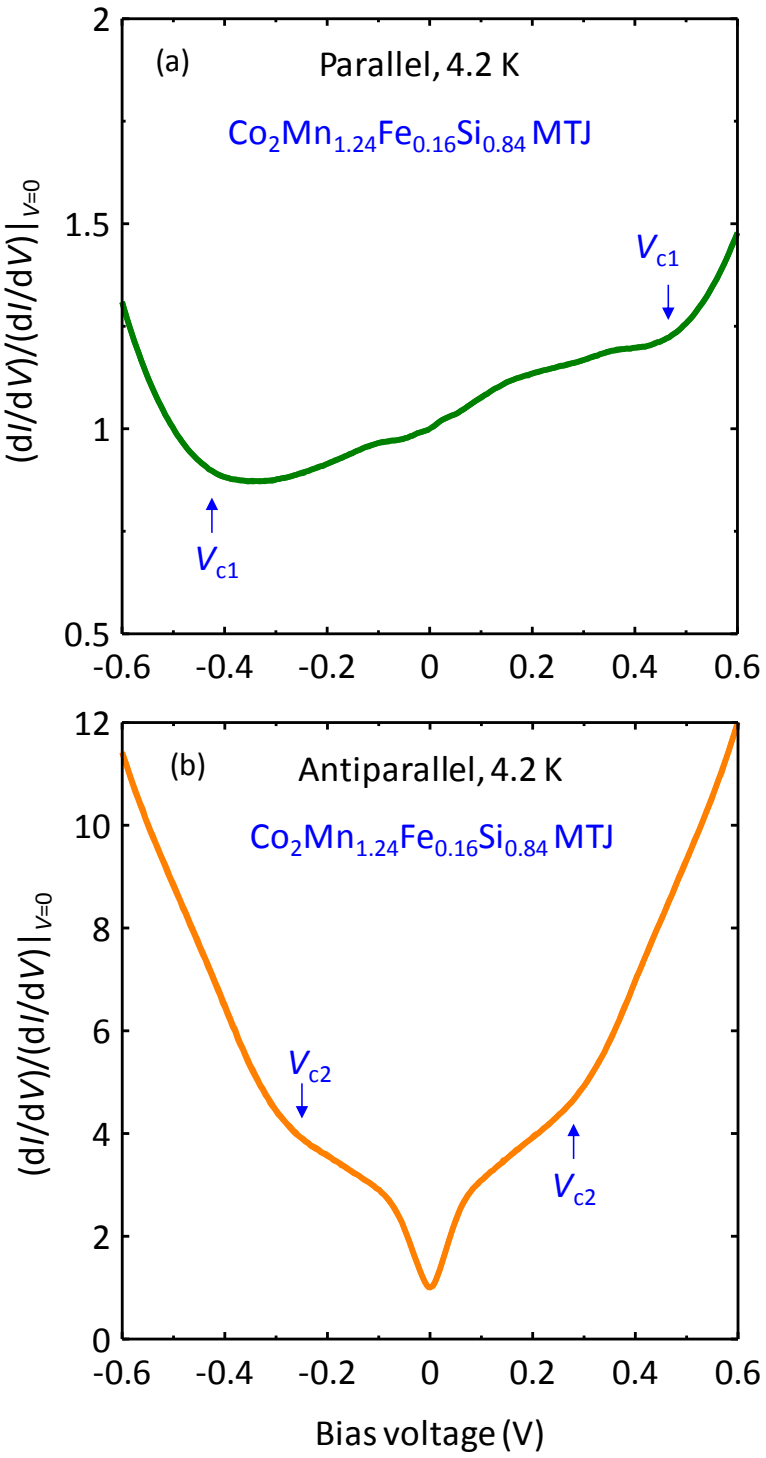

Fig. 4.5. Bias voltage dependences of the normalized differential conductances of $Co_2Mn_{1.24}Fe_{0.16}Si_{0.84}$/MgO/ $Co_2Mn_{1.24}Fe_{0.16}Si_{0.84}$ MTJ showing characteristic voltages, V_{c1} and V_{c2} for (a) parallel and (b) antiparallel magnetization configurations.

These characteristic voltages, V_{c1} and V_{c2}, can also be clearly seen from the second derivative data, d^2I/dV^2, as shown in Fig. 4.6 (a) and (b). We deduced the energy differences E_v between E_F to the top of the minority-spin valence band and E_c between the bottom of the minority-spin conduction band and E_F for the lower and upper electrodes by appropriately assigning the tunneling path to each characteristic voltage. That is, we assumed that the characteristic voltage, V_{c1}, for P would correspond to the opening of the tunneling path from the filled states of the minority-spin (m-spin) valence band of the emitter electrode to the empty states of the m-spin conduction band of the collector. This is because it is reasonable to assume that the tunneling current, due to the tunneling path from the majority-spin (M-spin) band of the emitter electrode to the M-spin band of the collector electrode, increases more continuously with V.

The tunneling path for the parallel magnetization configuration is shown by Fig. 4.7 for the positive (Fig. 4.7 (a)) and negative applied bias voltages (Fig. 4.7 (b)). We also assumed the characteristic voltage, V_{c2}, for AP would correspond to the opening of the tunneling path from the filled states of the M-spin band of the emitter electrode to the empty states of the m-spin conduction band of the collector electrode rather than the tunneling path from the m-spin valence band to the M-spin band. Similarly, the tunneling path for the antiparallel magnetization configuration is shown by Fig. 4.8 for positive (Fig. 4.8 (a)) and negative (Fig. 4.8 (b)) applied bias voltages.

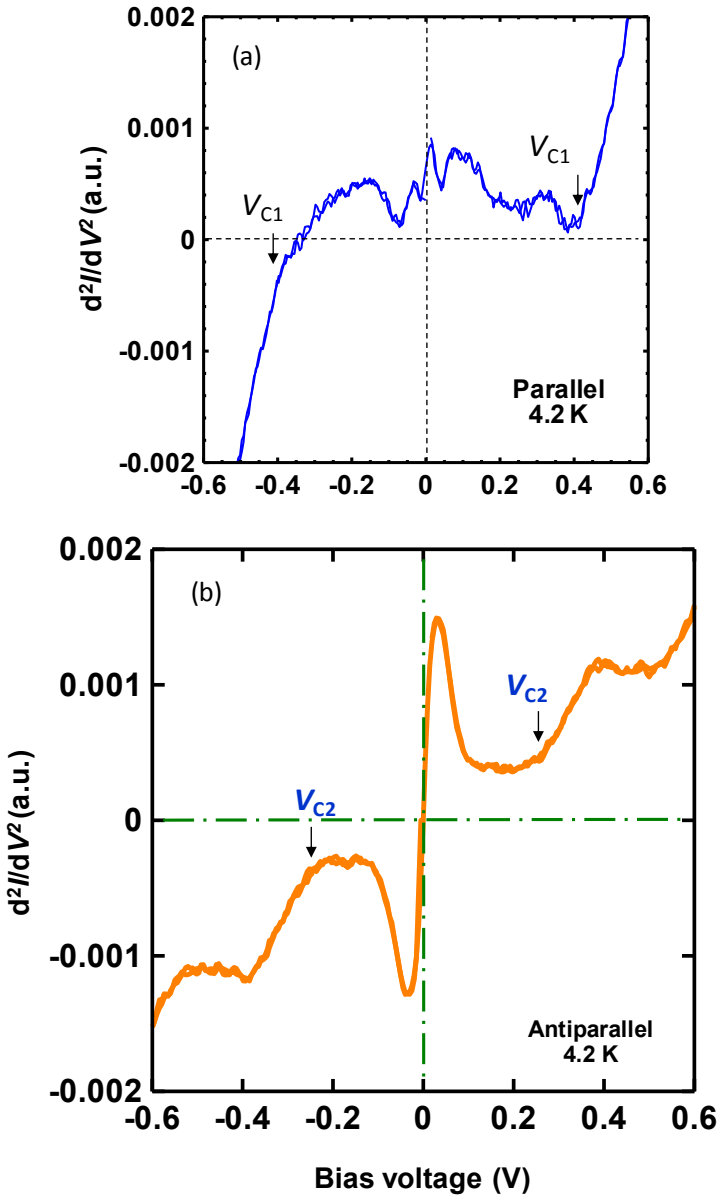

Fig. 4.6. Bias voltage dependence of the second derivative, d^2I/dV^2, of $Co_2Mn_{1.24}Fe_{0.16}Si_{0.84}$/MgO/ $Co_2Mn_{1.24}Fe_{0.16}Si_{0.84}$ MTJ mathematically obtained from the dI/dV data showing the characteristic voltages, V_{c1} and V_{c2} for (a) parallel and (b) antiparallel magnetization configurations.

Parallel

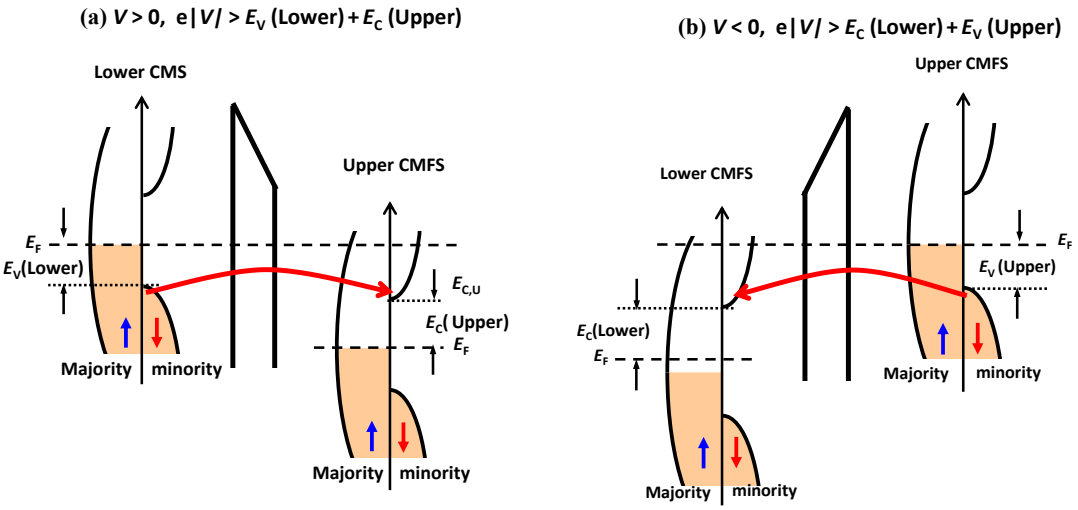

Fig. 4.7. Possible tunneling paths assumed during the parallel magnetization configuration for (a) a positive applied bias voltage (b) a negative applied bias voltage.

Antiparallel

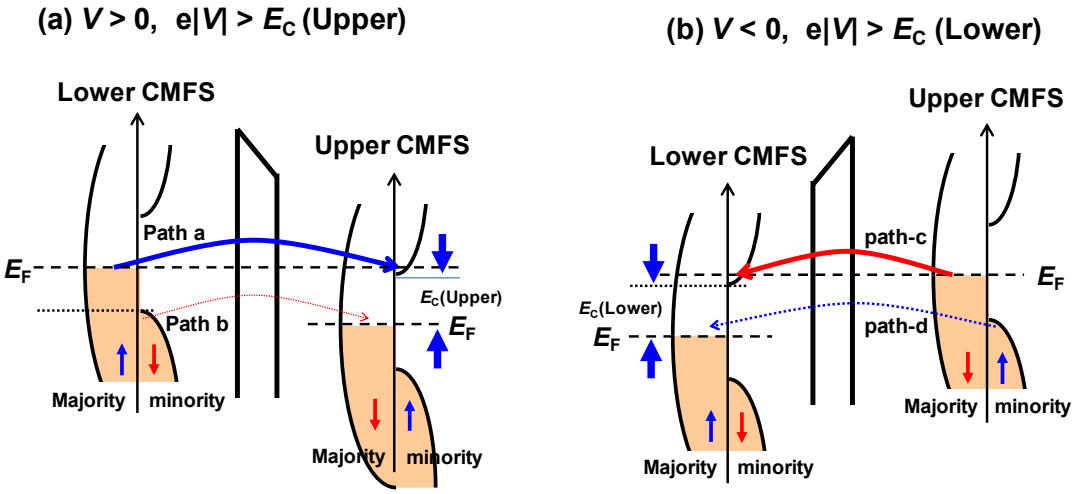

Fig. 4.8. Possible tunneling paths assumed during the antiparallel magnetization configuration for (a) a positive applied bias voltage (b) a negative applied bias voltage.

Given these assignments, we deduced the energy differences E_v and E_c. Then, we obtained the half-metal gap value E_g from $E_g = E_v + E_c$. The relative position of E_F in the half-metal gap is given by E_v/E_g. Then, the half-metal gap value, E_g and the relative position of E_F in the half-metal gap given by E_v/E_g were deduced for the lower and upper electrodes of this MTJ as listed in Table VII. Table VII shows the values of the half-metal gap, E_g, of $Co_2Mn_{1.24}Fe_{0.16}Si_{0.84}$ lower and upper electrodes (LE and UE). These values were deduced from the respective dI/dV versus V (and d^2I/dV^2 versus V) characteristics at 4.2 K of the $Co_2Mn_{1.24}Fe_{0.16}Si_{0.84}$/MgO/ $Co_2Mn_{1.24}Fe_{0.16}Si_{0.84}$ MTJ described above.

The E_g value for the lower electrode, E_g(LE), was slightly larger than that for the upper electrode, E_g(UP) for this MTJ; i.e., E_g(LE) = 0.43 eV, which was in contrast to E_g(UP) = 0.40. Thus, the analysis of the dI/dV vs. V characteristics revealed that the E_F of the $Co_2Mn_{1.24}Fe_{0.16}Si_{0.84}$ was located around the middle of the half-metal gap but a little closer to the top of the minority-spin valence band. Importantly, the relative E_F positions in the half-metal gap of the lower and upper $Co_2Mn_{1.24}Fe_{0.16}Si_{0.84}$ electrodes were 0.40 for the former and 0.29 for the latter.

Table VII. Values of the half-metal gap, E_g, of $Co_2Mn_{1.24}Fe_{0.16}Si_{0.84}$ upper and lower electrodes (UE and LE) obtained experimentally and the relative position of E_F in the half-metal gap, E_v/E_g for the upper and lower electrodes.

MTJ	Electrodes	E_g(LE) (eV)	E_g(UE) (eV)	E_g position (LE): E_v/E_g	E_g position (UE): E_v/E_g
$Co_2Mn_{1.24}Fe_{0.16}Si_{0.84}$ /MgO/ $Co_2Mn_{1.24}Fe_{0.16}Si_{0.84}$	$Co_2Mn_{1.24}Fe_{0.16}Si_{0.84}$	0.43	0.41	0.40	0.29

In order to confirm the validity of our experimental analysis, we compared the value of the half-metal gap obtained from this experimental analysis with that obtained from the theoretical calculation of the total DOS for the Heusler alloy $Co_2Mn_{1.24}Fe_{0.16}Si_{0.84}$. Figure 4.9 shows the spin-projected total DOS of the quaternary Heusler alloy $Co_2Mn_{1.24}Fe_{0.16}Si_{0.84}$ obtained theoretically from the first-principles density functional calculations. It is found that the E_g value obtained from the first-principles density

functional calculations was E_g(th) ≈ 0.40, as compared to E_g(LE) (= 0.43 eV) for the lower electrode and E_g(UP) (= 0.41) for the upper electrode of $Co_2Mn_{1.24}Fe_{0.16}Si_{0.84}$/MgO MTJs. Thus, interestingly, these two values (i.e. $E_g(exp)$ and $E_g(th)$) are in good agreement. Where, $E_g(exp)$ is the experimentally obtained half-metal gap value for the lower (E_g(LE)) and upper (E_g(UP)) electrodes, and $E_g(th)$ is the half-metal gap value theoretically obtained from the first-principles density functional calculations.

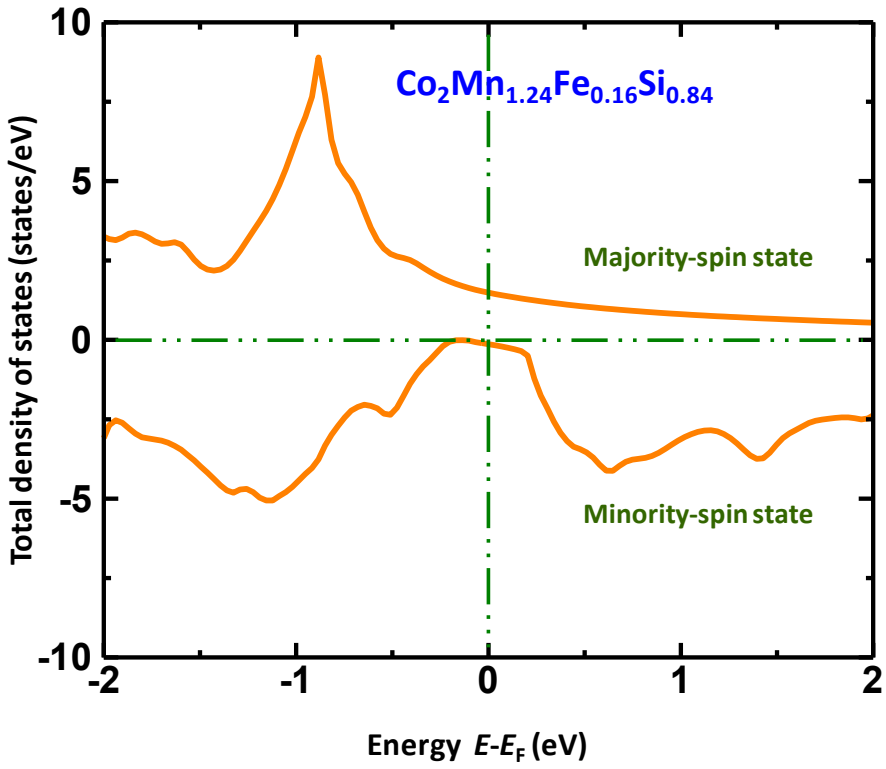

Fig. 4.9. Theoretically calculated spin-projected total DOS per formula unit for a CMFS film having a Mn-composition, *α*', of *α*' = 1.24 and Fe-composition, *β*', of *β*' = 0.16 ($Co_2Mn_{1.24}Fe_{0.16}Si_{0.84}$).

4.3 Summary

To investigate the origin of the giant TMR ratio demonstrated for MTJs with Mn-rich, lightly Fe-doped CMFS electrodes, we studied the film composition dependence of the μ_s for series-B CMFS thin films having a fixed (Mn+Fe)-rich composition of 1.40. Furthermore, we investigated the dependence of the TMR ratio of CMFS MTJs with $Co_2Mn_{\alpha'}Fe_{0.16}Si_{0.84}$ electrodes on α' in the Mn-rich composition region. Through these studies, it was revealed that residual $Co_{Mn/Fe}$ antisites were further suppressed in the Mn-rich, lightly Fe-doped CMFS ($Co_2Mn_{1.24}Fe_{0.16}Si_{0.84}$) because the available (Mn+Fe) composition in (Mn+Fe)-rich CMFS became larger than the critical Mn composition in Mn-rich CMS. This resulted in giant TMR ratios for CMFS MTJs with Mn-rich, lightly Fe-doped CMFS electrodes. On the other hand, a direct experimental observation of the half-metallic electronic states revealed that the position of the Fermi energy for the Heusler alloy with Mn-rich, lighly Fe-doped CMFS electrode is located near the middle of the half-metal gap and thus our analysis further confirms that the giant TMR ratio obtained for a CMFS MTJ with Mn-rich, lightly Fe-doped CMFS electrodes originated from the enhanced half-metallicity of this Heusler alloy.

Chapter 5

Bias voltage dependence of the spin-dependent tunneling conductance of CMFS MTJs

In chapter 1, we have discussed that the TMR ratio is one of the figures of merit of MTJs. In a circuit operation of an MRAM cell consisting of a series circuit of an MTJ and a field effect transistor (FET), a larger read signal difference between the AP state (binary "1" state) and the P state (binary "0" state), $\Delta V_{read} = V_{read}(AP) - V_{read}(P)$ is required. Let's derive the expression of this quantity for a circuit operation of supplying a constant current (I_0) to a selected memory cell. The read signal for P is expressed as $V_{read}(P) = I_0(R_P + R_{on})$, where R_{on} is the resistance of the FET for its on-state, and that for AP is expressed as $V_{read}(AP) = I_0(R_{AP} + R_{on})$. This results in $\Delta V_{read} = I_0(R_{AP} - R_P)$. Let's express the bias voltage that appears across the memory cell for the P state V_a by applying a constant current I_0. Then, we get an expression of $I_0 = V_a/(R_P + R_{on}) = V_a/[R_P(1 + R_{on}/R_P)] = V_0/R_P$, where V_0 is given as $V_0 = V_a/(1 + R_{on}/R_P)$. Thus, ΔV_{read} is expressed as:

$$\Delta V_{read} = V_0\left(\frac{R_{AP} - R_P}{R_P}\right) \qquad (5.1)$$

As shown in Eq. (5.1), a higher TMR ratio defined as $(R_{AP}-R_P)/R_P$ leads to a larger read signal difference ΔV_{read} at a given V_0. Importantly, the tunneling resistances R_P and R_{AP} have the respective bias voltage dependences, resulting in the bias voltage dependence of the TMR ratio. Thus, it is essential to clarify the bias voltage dependence of R_P and R_{AP} because a finite bias voltage of a few hundred millivolts is applied across an MTJ in an MRAM cell.

Previously, strong bias voltage dependence of the tunneling conductance of MTJs with amorphous and single crystalline barriers and ferromagnetic electrodes has been reported [59−80]. In particular, strong bias voltage dependence in the small bias region, called zero bias anomaly, was observed in these MTJs [59−61, 65−67, 69−71, 73, 75−77, 79, 70] for the conductance during the antiparallel magnetization configuration. In this study, we found that the tunneling conductance of both CMFS and CMS MTJs showed

strong bias voltage dependence in the small bias region for antiparallel magnetization alignment of the lower and upper electrodes.

To take full advantage of the half-metallic character of CMS and CMFS thin films for spintronic device applications, it is important to clarify the bias voltage dependence of the spin-dependent tunneling conductance and their origins. The bias voltage dependence of the tunneling conductances for the parallel and antiparallel magnetization alignments of half-metal-based MTJs generally showed respective behaviors for $|V|$ being smaller than E_v/e and E_c/e and for $|V|$ being equal to or larger than E_v/e and E_c/e, where, E_v is the energy difference from E_F to the top of minority-spin valence band and E_c is the energy difference from the bottom of minority-spin conduction band to E_F. For the latter voltage region, both G_P and G_{AP} showed discontinuous increase at the half-metal gap edges associated with opening of tunneling path from the filled-states of minority-spin valence band or that of tunneling path into the empty-states of minority-spin conduction band, which has been described in chapter 4 under section 4.2.

The purpose of this chapter is to clarify the characteristics of the bias voltage (V) dependence of the spin-dependent tunneling conductances of MTJs with half-metallic electrodes, in particular, with quaternary Heusler alloy CMFS electrodes and their origins. To do this, we experimentally investigated the V dependence of differential tunneling conductance, $G = dI/dV$, for the parallel and antiparallel magnetization alignments, G_P and G_{AP}, for MTJs with systematically varied spin polarizations at 4.2 K. In this chapter, we investigated the bias voltage dependence of G_P and G_{AP} for the small V regions of $|V|<E_v/e$ and $|V|<E_c/e$ for CMFS MTJs. We found strong increase in the tunneling conductance of AP for a small V region, resulting in the linear increase of G_{AP} with increasing V up to $V \sim 70$mV. Furthermore, it was found that the slope of G_{AP} versus V up to 70 mV increased with an increase in the spin polarization at 4.2 K. While G_P was almost independent of V. The origin of these features will be discussed in terms of the contribution of the tunneling conductance of inelastic tunneling via a magnon excited by hot electrons in section 5.1.

5.1 Experimental results and discussion

We investigated the bias voltage, V, dependence of the differential tunneling conductance for the parallel (P) and antiparallel (AP) magnetization alignments of the upper and lower electrodes (G_P and G_{AP}, respectively) of CMFS MTJs in order to clarify the origin of the strong V dependence of the spin-dependent tunneling conductance of these MTJs.

Figure 5.1(a) and (b) shows typical G spectra of a CMFS MTJ with $Co_2Mn_{0.73}Fe_{0.62}Si_{0.84}$ electrodes for the P and AP magnetization alignments at 4.2 K, for V of up to ±0.60 V, where G_P and G_{AP} normalized by their respective values at $V = 0$, i.e., $G_{N,P}$ and $G_{N,AP}$, are plotted. Discontinuous increases in $G_{N,P}$ and $G_{N,AP}$ were observed at the characteristic voltages V_{c1} for parallel magnetization alignment and V_{c2} for antiparallel one. The origin of these discontinuous increases is the opening of tunneling paths at the half-metal gap edges involving tunneling from the filled states of minority-spin valence band or that into the empty states of minority-spin conduction band, which has been described in chapter 4 under section 4.2. In this section, we will focus on the spin-dependent tunneling conductance characteristics for a V range of $|V|$ less than E_v/e and $|E_c/e$. Notably, G_{AP} showed a marked linear increase in the small V region of up to 70 mV. The increase in $G_{N,AP}$ was weakened for V of above $V = \pm$ 70 mV. In contrast, G_P was almost independent of $|V|$ as shown in Fig. 5.1(c). These features are similar to those observed for MgO-buffered CMS MTJs [77].

Note that we observed a similar feature for the temperature (T) dependence of G_P and G_{AP}, as that of the V dependence. That is, the G_{AP} showed stronger T dependence from 4.2 K to RT while G_P was relatively independent of T [81]. As it will be discussed in detail later, these two features, i.e. the V and T dependences of the G_{AP}, can be consistently explained by the contribution of spin-flip tunneling via a model by Zhang et al. [59].

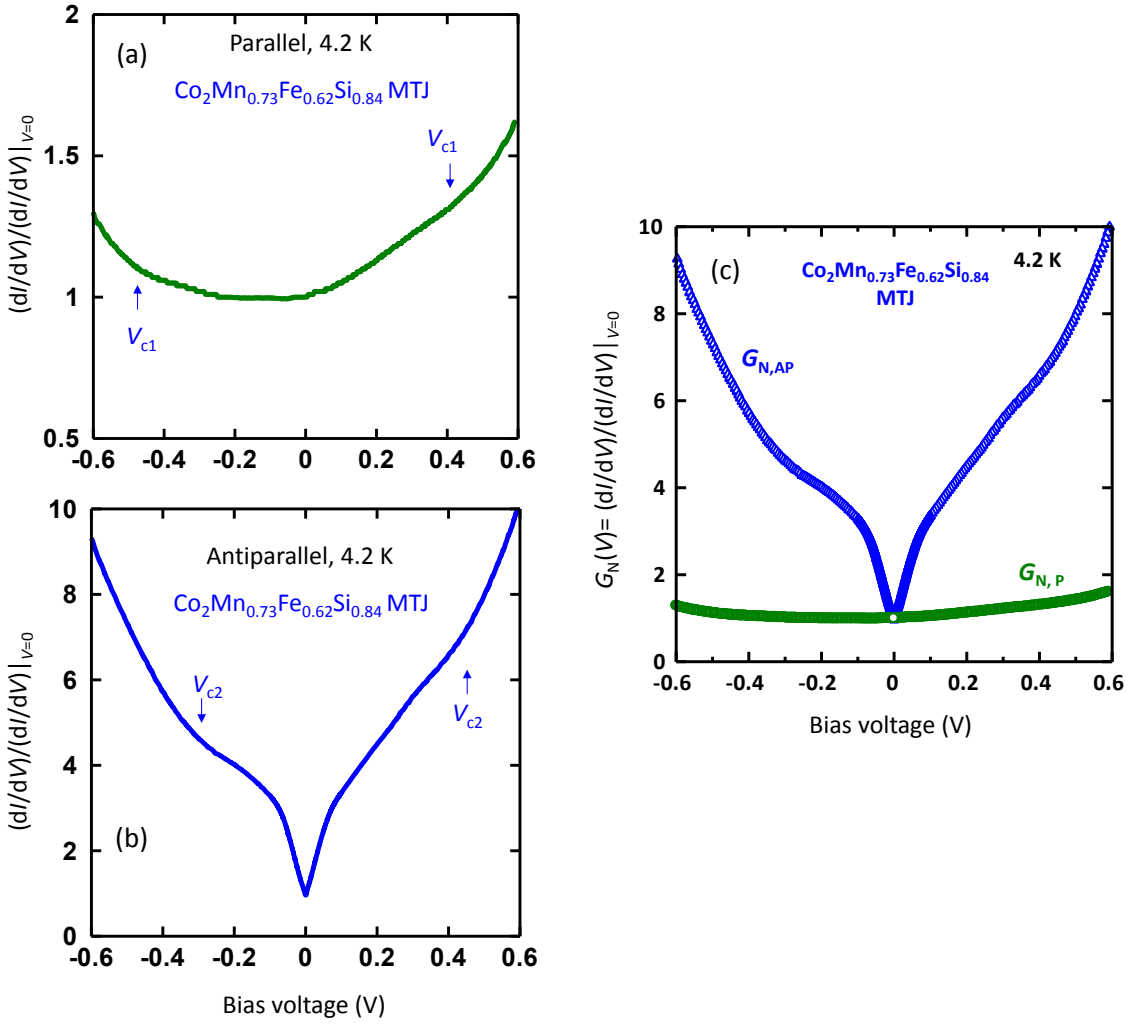

Fig. 5.1. Normalized differential conductance, $G_N(V) = (dI/dV)/(dI/dV)\big|_{V=0}$, as a function of the applied bias voltage for the (a) parallel and (b) antiparallel magnetization configurations showing the respective characteristic voltages (c) comparison of parallel and antiparallel differential conductances of $Co_2Mn_{0.73}Fe_{0.62}Si_{0.84}$/MgO/ $Co_2Mn_{0.73}Fe_{0.62}Si_{0.84}$ MTJ showing a high TMR ratio.

Figure 5.2 shows the V dependence of the TMR ratio for $Co_2Mn_{0.73}Fe_{0.62}Si_{0.84}$/MgO/$Co_2Mn_{0.73}Fe_{0.62}Si_{0.84}$ MTJ. From this figure, we can clearly see that the TMR ratio showed a marked decrease as V was increased from nearly 0 V to 0.7 V. Furthermore, from this feature, we can observe that the strong V dependence of the TMR ratio mainly comes from the V dependence of the G_{AP}. Therefore, given these experimental observations, it is important to study the V dependence of the G_{AP} and its origin in depth. In the following paragraphs we will discuss the origin of the observed features of the G spectra.

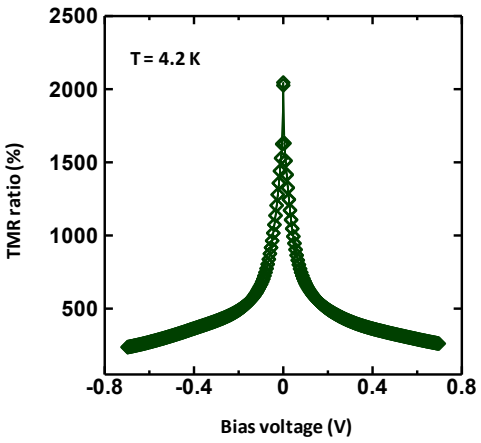

Fig. 5.2. The bias voltage dependence of the TMR ratio of $Co_2Mn_{0.73}Fe_{0.62}Si_{0.84}$/MgO/$Co_2Mn_{0.73}Fe_{0.62}Si_{0.84}$ MTJ experimentally obtained at 4.2 K.

Figure 5.3 shows the $G_{N,AP}$ spectra in a small V region of up to $V = \pm 0.20$ V for CMFS MTJs having various Fe composition, β', in $Co_2Mn_{0.73}Fe_{\beta'}Si_{0.84}$ electrodes (where β' = 0.0, 0.27, 0.57 and 0.62). Note that the TMR ratio increased with increasing (Mn+Fe) composition through β' from 570% at 4.2 K for $\beta' = 0$ (Mn-deficient $Co_2Mn_{0.73}Si_{0.84}$) to 1765% for $\beta' = 0.62$ ((Mn + Fe)-rich $Co_2Mn_{0.73}Fe_{0.62}Si_{0.84}$), as shown in Table VIII. From the comparison of the $G_{N,AP}$ spectra for these MTJs, the following interesting features were observed. First, the values of the characteristic voltage, V_s, up to which $G_{N,AP}$ showed a marked linear increase with V were almost the same for all the MTJs (this value was ≈ 70 mV for all the MTJs). Notably, the slope of $G_{N,AP}$ spectra in the V region of $|V| \leq 70$ mV was larger for an MTJ having higher TMR ratio at 4.2 K, i.e. for an MTJ having a higher spin polarization (P) at 0 K. Thus, the magnitude of $G_{N,AP}$ at $V = V_s$ was larger for an MTJ with higher P at 0 K. We will show these features, including a higher slope in $G_{N,AP}$ spectra in the V region for an MTJ having a higher P at 0 K, can be explained by Zhang's model [59], in which the increase in $G_{N,AP}$ with increasing V up to a certain characteristic voltage is ascribed to spin-flip inelastic tunneling via a magnon excited by a hot electron.

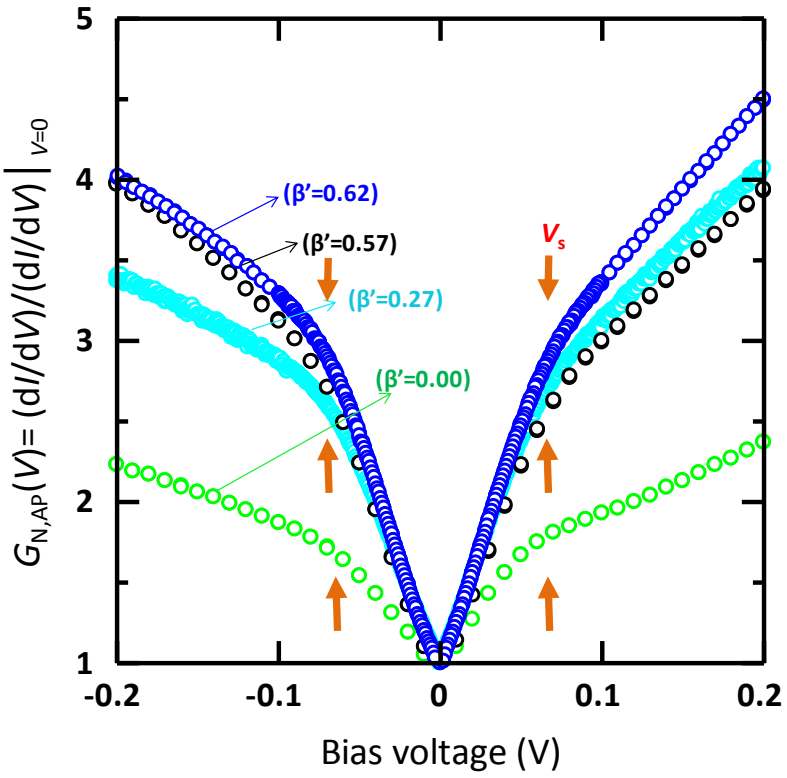

Fig. 5.3. Comparison of the bias voltage dependence of the normalized differential conductance for the antiparallel configuration of $Co_2Mn_{\alpha'}Fe_{\beta'}Si_{0.84}$/MgO/$Co_2Mn_{\alpha'}Fe_{\beta'}Si_{0.84}$MTJs. having a fixed Mn-composition of $\alpha' = 0.73$ and various Fe-compositions, β', ranging from $\beta' = 0$ to $\beta' = 0.62$ in a small bias region of $-0.2\ V < V_{bias} < 0.2\ V$.

Table VIII. Film composition expressed as $Co_2Mn_{\alpha'}Fe_{\beta'}Si_{0.84}$, Fe composition, β', in $Co_2Mn_{0.73}Fe_{\beta'}Si_{0.84}$ and TMR ratio at 4.2 K of $Co_2Mn_{0.73}Fe_{\beta'}Si_{0.84}$/MgO/ $Co_2Mn_{0.73}Fe_{\beta'}Si_{0.84}$ MTJs.

$Co_2Mn_{\alpha'}Fe_{\beta'}Si_{0.84}$ ($\alpha' = 0.73$)	Fe-composition, β', in $Co_2Mn_{0.73}Fe_{\beta'}Si_{0.84}$	TMR ratio (4.2 K)
$Co_2Mn_{0.73}Si_{0.84}$	0.00	575%
$Co_2Mn_{0.73}Fe_{0.27}Si_{0.84}$	0.27	1328%
$Co_2Mn_{0.73}Fe_{0.57}Si_{0.84}$	0.57	1686%
$Co_2Mn_{0.73}Fe_{0.62}Si_{0.84}$	0.62	1749%

Zhang's model [59] predicts a linear increase in the differential tunneling conductances with an increase in V for V of up to a certain characteristic voltage for both parallel and antiparallel magnetization alignments by considering spin-flip inelastic tunneling via a magnon excited by a hot electron. This model treats electron tunneling with a tunneling Hamiltonian. Originally, Zhang et al. derived the expressions of G_P and G_{AP} at finite voltages by assuming non-coherent tunneling, where the transversal crystal momentum of an electron is not conserved for tunneling. Furthermore, they assumed the magnitude of the matrix element of tunneling Hamiltonian (transfer Hamiltonian), $|T_d|$ or $|T_j|$, is independent of the wave vector $\boldsymbol{k}$ of an electron in the emitter before tunneling and $\boldsymbol{k}$' of an electron in the collector after tunneling. Thus, all electronic states at E_F contribute to the tunneling conductance. However, note that Zhang's model is not restricted to non-coherent tunneling.

Thus, Zhang's model predicts the following expressions for the tunneling conductances of P and AP at the limit of $V = 0$. Note that tunneling at a sufficiently small V is spin-conserving elastic tunneling.

Parallel (P): the tunneling path during P magnetization alignment is from Majority- to Majority-spin band or minority- to minority-spin band.

$$G_P(V=0,\ T=0)=\left.\frac{I}{V}\right|_{V\to 0}=\frac{4\pi e^2}{\hbar}\left(|T_d|^2+\left(S_L{}^2+S_R{}^2\right)|T_j|^2\right)\left(\rho_L{}^M\rho_R{}^M+\rho_L{}^m\rho_R{}^m\right) \tag{5.2}$$

Antiparallel (AP): the tunneling path during AP magnetization alignment is from Majority to minority-spin band or from minority to Majority-spin band.

$$G_{AP}(V=0,\ T=0)=\left.\frac{I}{V}\right|_{V\to 0}=\frac{4\pi e^2}{\hbar}\left(|T_d|^2+\left(S_L{}^2+S_R{}^2\right)|T_j|^2\right)\left(\rho_L{}^M\rho_R{}^m+\rho_L{}^m\rho_R{}^M\right) \tag{5.3}$$

where,

T_d: Matrix element which represents direct transfer

T_j: Matrix element which represents spin-dependent transfer

S_L, S_R: the spin operator for the left and right electrode, respectively

ρ_L, ρ_R: Density of states for the left and right electrode at E_F, respectively

V: applied voltage across the junction

Assuming identical lower and upper electrodes (i.e., $\rho_L{}^M = \rho_R{}^M = \rho_M$ and $\rho_L{}^m = \rho_R{}^m = \rho_m$), and with $eV < E_m$ (where $E_m = 3k_BT_c/(S+1)$, as defined below), Zhang's model predicts the voltage dependence of the normalized dI/dV for P and AP ($G_{N,P}$ and $G_{N,AP}$) due to spin-flip inelastic tunneling as follows:

$$\frac{\left.\frac{dI}{dV}\right|_P}{\left.\frac{dI}{dV}\right|_{P,V=0}} = 1 + \frac{|T_j|^2}{\left[|T_d|^2+2S^2|T_j|^2\right]}\frac{2S}{E_m}eV\frac{2\rho_M\rho_m}{(\rho_M{}^2+\rho_m{}^2)} = 1 + \frac{1}{\frac{|T_d|^2}{|T_j|^2}+2S^2}\frac{2S}{E_m}\xi eV$$

Thus,

$$\frac{\left.\frac{dI}{dV}\right|_P}{\left.\frac{dI}{dV}\right|_{P,V=0}} = 1 + Q\frac{2S}{E_m}\xi eV \qquad (5.4),$$

and

$$\frac{\left.\frac{dI}{dV}\right|_{AP}}{\left.\frac{dI}{dV}\right|_{AP,V=0}} 1 + \frac{|T_j|^2}{\left[|T_d|^2+2S^2|T_j|^2\right]}\frac{2S}{E_m}eV\frac{(\rho_M{}^2+\rho_m{}^2)}{2\rho_M\rho_m} = 1 + \frac{1}{\frac{|T_d|^2}{|T_j|^2}+2S^2}\frac{2S}{E_m}\frac{1}{\xi}eV$$

thus,

$$\frac{\left.\frac{dI}{dV}\right|_{AP}}{\left.\frac{dI}{dV}\right|_{AP,V=0}} = 1 + Q\frac{2S}{E_m}\frac{1}{\xi}eV \qquad (5.5),$$

where

$$\xi = \frac{2\rho_M\rho_m}{\rho_M{}^2+\rho_m{}^2} \qquad (5.6)$$

$$\frac{1}{\xi} = \frac{{\rho_M}^2 + {\rho_m}^2}{2\rho_M\rho_m} \tag{5.7}$$

$$Q = \frac{1}{\frac{|T_d|}{|T_j|} + 2S^2} \tag{5.8}$$

E_m is related to the Curie temperature (T_c) as follows:

$$E_m = \frac{3k_B T_c}{S+1},$$

where k_B = 1.38 x 10^{-23} J/K = 0.0861 meV/K and T_c is the Curie temperature

These equations by Zhang's model were derived with the assumption of non-coherent tunneling. Note that, however, Zhang's model is not restricted to non-coherent tunnling. In epitaxial MgO-based MTJs, including CMS and CMFS MTJs, the transversal crystal momentum of an electron is conserved for tunneling, i.e., electron tunneling is coherent tunneling. The derivation of the expressions for G_P and G_{AP} from the tunnling Hamiltonian of Zhang model for coherent tunneling requires all the dispersion curves of electrons and magnons, and therefore, is not realistic. As demonstrated by the comparison of the experimental spin polarization derived from the TMR ratios at 4.2 K with the first-priniciples calculations in Ref. 36 for CMS MTJs and chapter 3 of the present work for CMFS MTJs, it is reasonable to assume that only the electronic states of the majority- and minority-spin bands at E_F that satisfy the condition of coherent tunneling contribute to tunneling in CMS/MgO- and CMFS/MgO-based MTJs. Then, it is reasonable to apply the Zhang's expressions for G_P and G_{AP} to analyse the experimental V dependence of the tunneling conductances of these epitaxial MTJs by interpreting ρ_M and ρ_m appeared in the original expressions as those that satisfy the condition of coherent tunneling.

According to Eqs. 5.4 and 5.5, both $G_{N,P}$ and $G_{N,AP}$ for a small V region ($eV < E_m$) increase linearly with V with a common prefactor ($1 + Q2S/E_m$) but with the respective factors relating to the spin-dependent DOS at E_F, $\xi = 2\rho_M\rho_m/(\rho_M^2 + \rho_m^2)$ for the parallel configuration and $1/\xi = (\rho_M^2 + \rho_m^2)/ 2\rho_M\rho_m$ for the antiparallel configuration. If the spin polarization, P, becomes close to 1, ρ_m, the minority-spin DOS at E_F, becomes close to 0.

Thus, the factor for the parallel configuration, ξ, becomes small, then $G_{N,P}$ becomes small as P changes from low to high. While, the factor for the antiparallel configuration, $1/\xi$, becomes large, then $G_{N,AP}$ becomes large as P changes from low to high.

We will now explain the physical origin for an increase in $G_{N,AP}$ with increasing P in Zhang's model. In the antiparallel configuration, the tunneling conductance, i.e., I/V at V=0 (and T = 0), which is equal to dI/dV at V = 0 proportional to the quadratic sum of the DOS at the E_F, $2\rho_M\rho_m$, where ρ_M is the majority-spin DOS at E_F and ρ_m is the minority-spin DOS at E_F. This is because the spin of tunneling electron is conserved for tunneling (a majority-spin electron in the emitter tunnels into the minority-spin band of the collector and a minority-spin band electron tunnels into the majority-spin band for the antiparallel configuration). However, spin-flip inelastic tunneling via a magnon excited by hot electron induced by applying V occurs at finite V. Then, an electron in the majority-spin band (minority spin-band) in the emitter now has the probability of tunneling into the majority-spin band (the minority spin-band) in the collector through spin-flip inelastic tunneling. Thus, the variation in the differential conductance at a finite V is proportional to $(\rho_M^2 + \rho_m^2)$. Then, the variation in the differential conductance for the antiparallel configuration, ΔG_{AP}, normalized by its value at V = 0, $\Delta G_{AP}(V)/\Delta G_{AP}(V=0)$, is proportional to $[(\rho_M^2 + \rho_m^2)/2\rho_M\rho_m]=(1+ P^2)/(1- P^2)$, where P is the spin polarization at T = 0 K. This relation clearly shows that the contribution of inelastic tunneling via a magnon excited by a hot electron becomes larger as P comes higher.

A similar consideration leads to the P dependence of the contribution of inelastic tunneling via a magnon excited by a hot electron for the parallel configuration normalized by its value at V= 0 with a form of $\Delta G_P(V)/\Delta G_P(V=0)=[2\rho_M\rho_m/(\rho_M^2+\rho_m^2)]=(1-P^2)/(1+P^2)$. Thus, in contrast to the antiparallel configuration, the normalized contribution for the parallel configuration becomes small as P becomes higher, and it gets close to 0 as P gets close to 1.

Now, let's go back to our experimental results. We found that $G_{N,AP}$ showed a strong dependence on V and $G_{N,P}$ showed relatively weak dependence. Thus, the observed experimental feature is in good agreement with Zhang's model [59] described above. Thus, the key factor influencing the strong V dependence for the G_{AP} is the occurrence of inelastic tunneling processes via a magnon excited by hot electron.

In order to further see the correlation between the observed experimental features and that of the model based on spin-flip tunneling via a magnon, we extracted the G_{AP} values at V_s = 70 mV from our experimental data and plotted it as a function of 1/ ξ which is related to ρ_M and ρ_m as shown in Eq. 5.7. Before we discuss the analysis in detail, let's first derive a mathematical relation between ξ and the spin polarization, P. The basic definition of the spin polarization at E_F, P, in terms of ρ_M and ρ_m is:

$$P = \frac{\rho_M - \rho_m}{\rho_M + \rho_m} \tag{5.9}$$

$$P^2 = \left(\frac{\rho_M - \rho_m}{\rho_M + \rho_m}\right)^2 = \frac{1 - \frac{2\rho_M\rho_m}{(\rho_M{}^2+\rho_m{}^2)}}{1 + \frac{2\rho_M\rho_m}{(\rho_M{}^2+\rho_m{}^2)}} = \frac{1-\xi}{1+\xi} \tag{5.10}$$

Thus, ξ is related to P as follows:

$$\xi = \frac{2\rho_M\rho_m}{\rho_M{}^2+\rho_m{}^2} = \frac{1-p^2}{1+p^2} \tag{5.11}$$

Next let's see the derivation of the mathematical relation between ξ and TMR ratio at 4.2 K. From Eqs. (5.2) and (5.3), the expression of G_P and G_{AP} in terms of matrix elements of the transfer Hamiltonians, T_d and T_j, and density of states ρ_M and ρ_m is:

$$\frac{G_P(V=0,\ T=0)}{G_{AP}(V=0,\ T=0)} = \frac{\left(\frac{4\pi e^2}{\hbar}\right)\left[|T_d|^2 + 2S^2|T_j|^2\right](\rho_M{}^2 + \rho_m{}^2)}{\left(\frac{4\pi e^2}{\hbar}\right)\left[|T_d|^2 + 2S^2|T_j|^2\right](2\rho_M\rho_m)} = \frac{\rho_M{}^2 + \rho_m{}^2}{2\rho_M\rho_m} = \frac{1}{\xi} \tag{5.12}$$

Thus, $1/\xi$ is equal to $G_P(V=0, T=0)/ G_{AP}(V=0, T=0)$,

$$\frac{1}{\xi} = \frac{G_P(T=0)}{G_{AP}(T=0)} \tag{5.13}$$

This value is related to the TMR ratio at T = 0 as:

$$\frac{1}{\xi} = \frac{G_P(T=0)}{G_{AP}(T=0)} = \mathrm{TMR}(T=0) + 1 \approx \mathrm{TMR}\ (T=4.2\ \mathrm{K}) + 1 \tag{5.14}$$

Thus, we get the relation,

$$\frac{1}{\xi} = \mathrm{TMR}\ (T=4.2\ \mathrm{K}) + 1 \tag{5.15}$$

Figure 5.4 shows a plot of $G_{N,AP}$ at $V = V_s$ ($G_{N,AP}(V_s)$) of CMFS MTJs as a function of $1/\xi$ ($\approx$ TMR (T = 4.2 K) + 1, from Eq. 5.15). $G_{N,AP}(V_s)$ showed an almost linear dependence on $1/\xi$ ($\approx$ TMR (T = 4.2 K) + 1). This behavior is consistent with Zhang's model [59] (as shown in Eq. (5.5)), where the tunneling conductance as a function of V in a small V region is explained by spin-flip tunneling via a magnon excited by a hot electron. This model predicts that $G_{N,AP}$ increases with $1/\xi = [(\rho_M^2+\rho_m^2)/(2\rho_M\rho_m)] = (1+P^2)/(1-P^2)$, while $G_{N,P}$ increases with ξ. Here, $1/\xi$ is equal to G_P/G_{AP} (at T = 0) = (TMR(0 K) + 1), which was approximated by (TMR (4.2 K) + 1) as shown by Eq. 5.15. Thus, according to this model, the V dependence up to V_s, where eV_s corresponds to the maximum magnon energy of $3kT_c/(S+1)$ [59], is significantly stronger for AP compared with that for P and becomes stronger for the MTJ having an electrode with a higher spin polarization. Thus, the experimentally observed features, in particular, the linear increase in $G_{N,AP}(V_s)$ with (TMR (4.2 K) + 1), can be explained by Zhang's model. Thus, this analysis further confirms that our experimentally observed features are well modeled by the theory based on a spin flip tunneling process and thus the origin of the strong bias voltage dependence in a small bias range of $G_{N,AP}$ can be well explained by an inelastic tunneling process via a magnon.

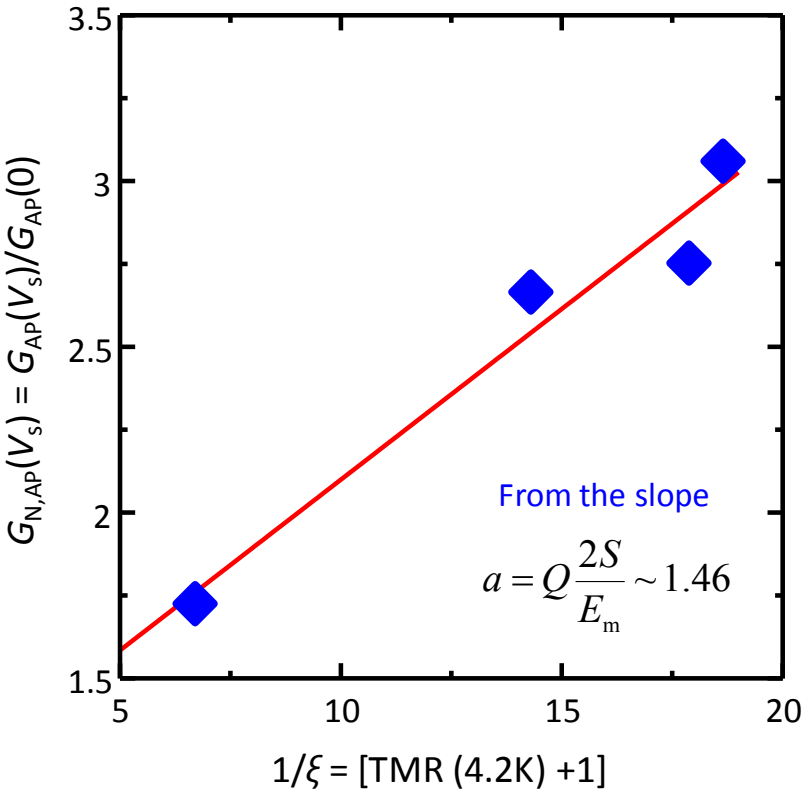

Fig. 5.4. The dependence of the normalized antiparallel conductance at the characteristics voltage, Vs, on $1/\xi$ (= TMR (4.2 K) + 1), of $Co_2Mn_{\alpha'}Fe_{\beta'}Si_{0.84}$/MgO/ $Co_2Mn_{\alpha'}Fe_{\beta'}Si_{0.84}$. MTJs having a fixed Mn-composition of α' = 0.73 and various Fe-compositions, β', ranging from β' = 0 to β' = 0.62.

5.2 Correlation between bias voltage dependence and temperature dependence

In this section, we will briefly discuss the correlation between the bias voltage dependence of the spin-dependent differential tunneling conductance for the antiparallel magnetization configuration and the temperature dependence.

Similar to the V dependence of G_{AP}, Zhang et al. also proposed a model equation for the T dependence of the G_{AP}, as shown by Eq. 5.16. This model also ascribed the strong temperature dependence of the G_{AP} to the spin-flip tunneling process via thermally exited magnons. Then, it is expected that the pre-factors obtained from the V dependence (i.e. Eq. 5.5) and T dependence (Eq. 5.16) should be comparable. Thus, in order to further strengthen our conclusion, we compared the pre-factors obtained from V dependence and that from T dependence. First, we fitted the $G_{N,AP}(V_s)$ shown in Fig. 5.4 (shown by red fitting line) and after some mathematical manipulation, we found the value of $Q2S/E_M$ to be 1.46 (i.e. $Q2S/E_M = 1.46$). Next, we fitted the T dependence of G_{AP} and obtained the value for $Q2S/E_M$ to be ≈ 1.0 (i.e., $Q2S/E_M \approx 1.0$). Therefore, this analysis shows that the pre-factor obtained from the V dependence of $G_{N,AP}$ was in a good agreement with that obtained from the fitting of the T dependence of the tunneling conductance for AP. Thus, these two experimental features (i.e. the strong V and T dependences of the G_{AP}), can be consistently explained by a spin-flip tunneling process via a magnon excited by a hot electron (for the V dependence) and via a thermally excited magnon (for the T dependence).

$$\frac{G_P(T)}{G_P(T=0)} = 1 + Q\frac{2S}{E_m} \bullet \xi \bullet k_B T \bullet f(T) \qquad (5.16)$$

$$\frac{G_{AP}(T)}{G_{AP}(T=0)} = 1 + Q\frac{2S}{E_m} \bullet \frac{1}{\xi} \bullet k_B T \bullet f(T) \qquad (5.17)$$

$$f(T) = ln\left(1 - exp\left(-\frac{E_c}{kT}\right)\right) = \begin{cases} exp\left(-\frac{E_c}{kT}\right), & for\ kT < E_c \\ ln\frac{kT}{E_c}, & for\ kT > E_c \end{cases}$$

5.3 Summary

In summary, we clarified the key tunneling mechanism that determines the spin-dependent tunneling characteristics of CMFS MTJs. We found a strong bias voltage dependence of the differential conductance for AP for CMFS and CMS MTJs that showed giant TMR ratios. Thus, we showed that the bias voltage dependence of the tunneling conductance for AP in a small bias voltage region of up to $V_{\mathrm{bias}} \approx 70$ mV was stronger for electrodes having higher spin polarization. This feature was explained by spin-flip tunneling via a magnon excited by a hot electron. Moreover, we demontrated a correlation between the bias voltage dependence and the temperature dependence of the antiparallel conductance and found that both dependences can be consistently explained by Zhang's model.

Chapter 6
Conclusion

In this dissertation, we investigated the key factors that critically affect the half-metallicity of the quaternary Heusler alloy CMFS by examining the film composition dependence of the saturation magnetization per formula unit, μ_s, of CMFS thin films and the TMR ratio of CMFS/MgO/CMFS MTJs. We also investigated the origin of the giant TMR ratio of up to 2610% at 4.2 K (429% at 290 K) obtained for CMFS MTJs with Mn-rich, lightly Fe-doped CMFS electrodes. Finally, in order to understand the key tunneling mechanism occurring in CMFS and CMS MTJs, we investigated the bias voltage dependence of the spin-dependent tunneling conductance of CMFS and CMS MTJs. This investigation was done by studying the dI/dV versus V characteristics of MTJs having CMFS and CMS electrodes that showed giant TMR ratios.

In summary, the following are the main results we obtained.

[1] The experimentally investigated μ_s and TMR ratios, in combination with first-principles calculations, indicated that $Co_{Mn/Fe}$ antisites in the quaternary alloy are detrimental to half-metallicity, similar to ternary alloy CMS. It was demonstrated that (Mn+Fe)-rich compositions are highly effective at suppressing harmful $Co_{Mn/Fe}$ antisites and that relatively small Fe ratio in the total (Mn+Fe) composition retains a half-metallic state.

[2] The investigation of the origin of the giant TMR ratio for CMFS MTJs with Mn-rich, lightly Fe-doped electrodes revealed that residual $Co_{Mn/Fe}$ antisites were further suppressed in lightly Fe-doped CMFS because the available (Mn+Fe) composition in (Mn+Fe)-rich CMFS became larger than the critical Mn composition in Mn-rich CMS. This resulted in giant TMR ratio for CMFS MTJs with Mn-rich, lightly Fe-doped CMFS electrodes. Furthermore, our spectroscopy analysis results showed that the Fermi energy is located around the middle of the half-metallic energy gap for this quaternary Heusler alloy. Thus, our findings indicate that the appropriate control of off-stoichiometry and film composition of quaternary Heusler alloy CMFS toward a Mn-rich, lightly

Fe-doped composition is highly promising for fully utilizing the half-metallicity of quaternary CMFS thin films as spin source materials.

[3] The dI/dV versus V characteristics (G spectra) of the CMFS and CMS MTJs showed dip structures for antiparallel alignment (AP) in a small bias region of up to ±70 mV. Moreover, it is found that the dI/dV value for AP at characteristic voltages, $V_s = \pm 70$ mV, normalized by the value at $V = 0$ increased linearly with the TMR ratio at 4.2 K. Thus, it was clarified that MTJs having electrodes with higher spin polarization showed stronger bias voltage dependence. This feature was consistently explained by spin-flip tunneling via a magnon excited by a hot electron along with the strong temperature dependence of tunneling conductance for AP by spin-flip tunneling via a thermally excited magnon.

Acknowledgements

First and foremost, Glory to Almighty **God** and **his Mother** for giving me the strength and courage to pass all the difficulties I faced and for all the successes they granted me throughout my life.

First, I would like to express my deepest gratitude to Professor Masafumi Yamamoto, for his continuous and unlimited supervision. I have gained a great experience and knowledge through his excellent and invaluable guidance and supervision.

My deepest thanks also go to Professor Tetsuya Uemura for his wonderful supervision, all his assistance, useful discussions and great help throughout my PhD study.

I am also grateful to Professor Akihisa Tomita and Professor Akihiro Murayama for reviewing this dissertation and offering their helpful comments.

I am also indebted to Professor Yoshio Miura and Professor Masafumi Shirai for their collaboration in the theoretical calculation of the electronic band structure of Co_2(Mn,Fe)Si Heusler alloys. I really appreciate their great contribution in this study and also for the valuable discussions and advice.

I want to also pass my deepest appreciation to senior students who gave me a tremendous help and support on the experimental procedures and on how to operate the experimental apparatuses which I used for this study. Their valuable support and advice really helped me to successfully carryout my experimental works. I also want to say thank you for all the members of Laboratory of Nanoscale Electron Devices for all their collaborations.

I would like to convey my deepest gratitude to the Ministry of Education, Culture, Sports, Science and Technology in Japan (MEXT) for financially supporting me throughout my doctoral course study.

Finally, I want to give a special thanks to my beloved and caring husband Belay Gessesse for his everyday motivation, advice and comfort whenever I feel down. I really thank you for being such a good husband and my only best friend at the same time.

Last but definitely not least, I would like to thank my mother for bringing me up with

unconditional love and extra care. She is a woman of exemplary character who always reminds me to be a strong, independent and hard working person. I will always remember the life time sacrifices you made to grant me a better life than you had. You will continue to be my role model and my hero forever.

References

[1] Magnetic Memory, Fundamentals and technology, Denny D. Tang and Yuan- Jen Lee, MagIC Technologies, Inc., Cambridge University Press, 2010.

[2] I. Žutić, J. Fabian, and S. Das Sarma, Rev. Mod. Phys. **76**, 323 (2004).

[3] S. A. Wolf, D. D. Awschalom, R. A. Buhrman, J. M. Daughton, S. von Molnár, M. L. Roukes, A. Y. Chtchelkanova, and D. M Treger, Science **294**, 1488 (2001).

[4] W. H. Butler, X. –G. Zhang, T. C. Schulthess, and J. M. MacLaren, Phys. Rev. B **63**, 054416 (2001).

[5] J. Mathon and A. Umerski, Phys. Rev. B **63**, 220403(R) (2001).

[6] S. Yuasa, T. Nagahama, A. Fukushima, Y. Suzuki, and K. Ando, Nature Mater. **3**, 868 (2004).

[7] S. S. Parkin, C. Kaiser, A. Panchula, P. M. Rice, B. Hughes, M. Samant, and S. H. Yang, Nature Mater. **3**, 862 (2004).

[8] R. A. de Groot, F. M. Müller, P. G. v. Engen, and K. H. J. Buschow, Phys. Rev. Lett. 50, 2024, (1983).

[9] T. Graf, C. Felser, and S. S. P. Parkin, Prog. Solid State Chem. **39**, 1 (2011).

[10] M. Yamamoto, T. Marukame, T. Ishikawa, K.-i. Matsuda, T. Uemura, and M. Arita, J. Phys. D: Appl. Phys. **39**, 824 (2006).

[11] T. Ishikawa, T. Marukame, H. Kijima, K.-i. Matsuda, T. Uemura, M. Arita, and M. Yamamoto, Appl. Phys. Lett. **89**, 192505 (2006).

[12] N. Tezuka, N. Ikeda, F. Mitsuhashi, and S. Sugimoto, Appl. Phys. Lett. 94, 162504 (2009).

[13] M. Yamamoto, T. Ishikawa, T. Taira, G.-f. Li, K.-i. Matsuda, and T. Uemura, J. Phys.: Condens. Matter **22**, 164212 (2010).

[14] H.-x. Liu, Y. Honda, K.-i. Matsuda, M. Arita, T. Uemura, and M. Yamamoto, Jpn. J. Appl. Phys. **51**, 093004 (2012).

[15] H.-x. Liu, Y. Honda, T. Taira, K.-i. Matsuda, M. Arita, T. Uemura, and M. Yamamoto, Appl. Phys. Lett. **101**, 132418 (2012).

[16] T. Marukame, T. Ishikawa, T. Taira, K.-i. Matsuda, T. Uemura, and M. Yamamoto, Phys. Rev. B **81**, 134432 (2010).

[17] W. Wang, E. Liu, M. Kodzuka, H. Sukegawa, M. Wojcik, E. Jedryka, G. H. Wu,

K. Inomata, S. Mitani, and K. Hono, Phys. Rev. B **81**, 140402 (R) (2010).

[18] T. Furubayashi, K. Kodama, H. Sukegawa, Y. K. Takahashi, K. Inomata, and K. Hono, Appl. Phys. Lett. **93**, 122507 (2008).

[19] Y. Sakuraba, K. Izumi, T. Iwase, S. Bosu, K. Saito, K. Takanashi, Y. Miura, K. Futatsukawa, K. Abe, and M. Shirai, Phys. Rev. B **82**, 094444 (2010).

[20] Y. K. Takahashi, A. Srinivasan, B. Varaprasad, A. Rajanikanth, N. Hase, T. M. Nakatani, S. Kasai, T. Furubayashi, and K. Hono, Appl. Phys. Lett. **98**, 152501 (2011).

[21] M. J. Carey, S. Maat, S. Chandrashekariaih, J. A. Katine, W. Chen, B. York, and J. R. Childress, J. Appl. Phys. 109, 093912 (2011).

[22] J. Sato, M. Oogane, H. Naganuma, and Y. Ando, Appl. Phys. Express **4**, 113005 (2011).

[23] Y. Sakuraba, M. Ueda, Y. Miura, K. Sato, S. Bosu, K. Saito, M. Shirai, T. J. Konno, and K. Takanashi, Appl. Phys. Lett. **101**, 252408 (2012).

[24] X. Y. Dong, C. Adelmann, J. Q. Xie, C. J. Palmstrøm, X. Lou, J. Strand, P. A. Crowell, J.-P. Barnes, and A. K. Petford-Long, Appl. Phys. Lett. **86**, 102107 (2005).

[25] M. Ramsteiner, O. Brandt, T. Flissikowski, H. T. Grahn, M. Hashimoto, J. Herfort, and H. Kostial, Phys. Rev. B **78**, 121303(R) (2008).

[26] T. Akiho, J. Shan, H.-x. Liu, K.-i. Matsuda, M. Yamamoto, and T. Uemura, Phys. Rev. B. **87**, 235205 (2013).

[27] P. Bruski, Y. Manzke, R. Farshchi, O. Brandt, J. Herfort, and M. Ramsteiner, Appl. Phys. Lett. **103**, 052406 (2013).

[28] T. Saito, N. Tezuka, M. Matsuura, and S. Sugimoto, Appl. Phys. Express **6**, 103006 (2013).

[29] Y. Ebina, T. Akiho, H.-x. Liu, M. Yamamoto, and T. Uemura, Appl. Phys. Lett. **104**, 172405 (2014).

[30] T. Uemura, T. Akiho, Y. Ebina, and M. Yamamoto, Phys. Rev. B **91**, 140410(R) (2015).

[31] S. Ishida, S. Fujii, S. Kashiwagi, and S. Asano, J. Phys. Soc. Jpn. **64**, 2152 (1995).

[32] S. Picozzi, A. Continenza, and A. J. Freeman, Phys. Rev. B **66**, 094421 (2002).

[33] I. Galanakis, P. H. Dederichs, and N. Papanikolaou, Phys. Rev. B **66**, 174429 (2002).

[34] P. J. Webster, J. Phys. Chem. Solids **32**, 1221 (1971).

[35] S. Picozzi, A. Continenza, and A. J. Freeman, Phys. Rev. B **69**, 094423 (2004).

[36] G.-f. Li, Y. Honda, H.-x. Liu, K.-i. Matsuda, M. Arita, T. Uemura, M. Yamamoto, Y. Miura, M. Shirai, T. Saito, F. Shi, and P. M. Voyles, Phys. Rev. B **89,** 014428 (2014).

[37] J.-P. Wüstenberg, R. Fetzer, M. Aeschlimann, M. Cinchetti, J. Minár, Jürgen Braun, H. Ebert, T. Ishikawa, T. Uemura, and M. Yamamoto, Phys. Rev. B **85**, 064407 (2012).

[38] S. Ouardi, G. H. Fecher, S. Chadov, B. Balke, X. Kozina, C. Felser, T. Taira, and M. Yamamoto, Applied Physics A: Materials Science & Processing **111**, 395 (2013).

[39] X. Kozina, J. Karel, S. Ouardi, S. Chadov, G. H. Fecher, C. Felser, G. Stryganyuk, B. Balke, T. Ishikawa, T. Uemura, M. Yamamoto, E. Ikenaga, S. Ueda, and K. Kobayashi, Phys. Rev. B **89**, 125116 (2014).

[40] R. Fetzer, S. Ouardi, Y. Honda, H.-x. Liu, S. Chadov, B. Balke, S. Ueda, M. Suzuki, T. Uemura, M. Yamamoto, M. Aeschlimann, M. Cinchetti, G. H. Fecher, and C. Felser, J. Phys. D: Appl. Phys. **48**, 164002 (2015).

[41] D. Asakura, T. Koide, S. Yamamoto, K. Tsuchiya, T. Shioya, K. Amemiya, V. R. Singh, T. Kataoka, Y. Yamazaki, Y. Sakamoto, A. Fujimori, T. Taira, and M. Yamamoto, Phys. Rev. B **82**, 184419 (2010).

[42] V. R. Singh, V. K. Verma, K. Ishigami, G. Shibata, T. Kadono, A. Fujimori, D. Asakura, T. Koide, Y. Miura, M. Shirai, G.-f. Li, T. Taira, and M. Yamamoto, Phys. Rev. B **86**, 144412 (2012).

[43] V. R. Singh, V. K. Verma, K. Ishigami, G. Shibata, A. Fujimori, T. Koide, Y. Miura, M. Shirai, T. Ishikawa, G. -f. Li, and M. Yamamoto, J. Appl. Phys. **117**, 203901 (2015).

[44] Y. Miura, K. Nagao, and M. Shirai, Phys. Rev. B **69**, 144413 (2004).

[45] M. Jullière, Phys. Lett. **54A**, 225 (1975).

[46] T. Ishikawa, H.-x. Liu, T. Taira, K-i. Matsuda, T. Uemura, and M. Yamamoto, Appl. Phys. Lett. **95**, 232512 (2009).

[47] H.-x. Liu, T. Kawami, K. Moges, T. Uemura, M. Yamamoto, F. Shi and P. M. Voyles, J. Phys. D: Appl. Phys. **48**, 164001 (2015).

[48] T. Saito, T. Katayama, T. Ishikawa, M. Yamamoto, D. Asakura, and T. Koide, Appl. Phys. Lett. **91**, 262502 (2007).

[49] T. Saito, T. Katayama, T. Ishikawa, M. Yamamoto, D. Asakura, T. Koide, Y. Miura, and M. Shirai, Phys. Rev. B **81**, 144417 (2010).

[50] R. Fetzer, B. Stadtmüller, Y. Ohdaira, H. Naganuma, M. Oogane, Y. Ando, T. Taira, T. Uemura, M. Yamamoto, M. Aeschlimann, and M. Cinchetti, Sci. Rep. **5**, 8537 (2015).

[51] L. G. Parratt, Phys. Rev. **95**, 359 (1954).

[52] W. Kohn and N. Rostoker, Phys. Rev. **94**, 1111 (1954).

[53] H. Akai and P. H. Dederichs, Phys. Rev. B **47**, 8739 (1993).

[54] M. Rasolt and D. J. W. Geldart, Phys. Rev. B **34**, 1325 (1986).

[55] B. Hülsen, M. Scheffler, and P. Kratzer, Phys. Rev. B **79**, 094407 (2009).

[56] W. H. Butler, X.-G. Zhang, T. C. Schulthess, and J. M. MacLaren, Phys. Rev. B **63**, 054416 (2001).

[57] J. Mathon and A. Umerski, Phys. Rev. B **63**, 220403(R) (2001).

[58] Y. Miura, H. Uchida, Y. Oba, K. Nagao, and M. Shirai, J. Phys.: Condens. Matter **19**, 365228 (2007).

[59] S. Zhang, P. M. Levy, A. C. Marley and S. S. P. Parkin, Phys. Rev. Lett. **79**, 3744 (1997).

[60] J. S. Moodera, J. Nowak, and R. J. M. van de Veerdonk, Phys. Rev. Lett. **80**, 2941 (1998).

[61] J. Zhang, and R. M. White, J. Appl. Phys. **83**, 6512 (1998).

[62] J. Murai, Y. Ando, M. Kamijo, H. Kubota, and T. Miyazaki, Jpn. J. Appl. Phys. **38**, 1106 (1999).

[63] R. Jansen, and J. S. Moodera, Phys. Rev. B **61**, 9047 (2000).

[64] P. LeClair, H. J. M. Swagten, J. T. Kohlhepp, and W. J. M. de Jonge, Appl. Phys. Lett. **76**, 3783 (2000).

[65] X.-F. Han, A. C. C. Yu, M. Oogane, J. Murai, T. Daibou, and T. Miyazaki, Phys. Rev. B **63**, 224404 (2001).

[66] C. Lü, M. W. Wu, X. F. Han, Phys. Lett. A **319**, 205 (2003).

[67] J. Schmalhorst, S. Kammerer, G. Reiss, and A. Hütten, Appl. Phys. Lett. **86**, 052501 (2005).

[68] S.-J. Ahn, T. Kato, H. Kubota, Y. Ando, and T. Miyazaki, Appl. Phys. Lett. **86**, 102506 (2005).

[69] Y. Ando, T. Miyakoshi, M. Oogane, T. Miyazaki, H. Kubota, K. Ando, and S. Yuasa, Appl. Phys. Lett. **87**, 142502 (2005).

[70] R. Matsumoto, Y. Hamada, M. Mizuguchi, M. Shiraishi, H. Maehara, K. Tsunekawa, D. D. Djayaprawira, N. Watanabe, Y. Kurosaki, T. Nagahama, A. Fukushima, H. Kubota, S. Yuasa, and Y. Suzuki, Solid State Commun. **136**, 611 (2005).

[71] L. Yuan, S. H. Liou, and D. Wang, Phys. Rev. B **73**, 134403 (2006).

[72] G.-x. Miao, K. B. Chetry, A. Gupta, W. H. Butler, K. Tsunekawa, D. Djayaprawira, and G. Xiao, J. Appl. Phys. **99**, 08T305 (2006).

[73] T. Marukame, T. Ishikawa, K.-i. Matsuda, T. Uemura, and M. Yamamoto, J. Appl. Phys. **99**, 08A904 (2006).

[74] S. Tsunegi, Y. Sakuraba, M. Oogane, K. Takanashi, and Y. Ando, Appl. Phys. Lett. **93**, 112506 (2008).

[75] S. Nishioka, R. matsumoto, H. Tomita, T. Nozaki, Y. Suzuki, H. Itoh, and S. Yuasa, Appl. Phys. Lett. **93**, 122511 (2008).

[76] T. Ishikawa, N. Itabashi, T. Taira, K.-i. Matsuda, T. Uemura, and M. Yamamoto, Appl. Phy. Lett. **94**, 092503 (2009).

[77] T. Ishikawa, N. Itabashi, T. Taira, K.-i. Matsuda, T. Uemura, and M. Yamamoto, J. Appl. Phys. **105**, 07B110 (2009).

[78] A. A. Khan, J. Schmalhorst, G. Reiss, G. Eilers, M. Münzenberg, H. Schuhmann, and M. Seibt, Phys. Rev. B **82**, 064416 (2010).

[79] J. Bernos, M. Hehn, F. Montaigne, C. Tiusan, D. Lacour, M. Alnot, B. Negulescu, G. lengaigne, E. Snoeck, and F. G. Aliev, Phys. Rev. B **82**, 060405(R) (2010).

[80] J. M. Teixeira, J. Ventura, M. P. Fernández-García, J. P. Araujo, J. B. Sousa, P. Wisniowski, and P. P. Freitas, Appl. Phys. Lett. **100**, 072406 (2012).

[81] B. Hu, K. Moges, Y. Honda, H.-x. Liu, T. Uemura, and Masafumi Yamamoto, Jun-ichiro Inoue, and Masafumi Shirai, (submitted).

Appendix

Publication list

1. Publications related to this dissertation

1. Kidist Moges, Yusuke Honda, Hong-xi Liu, Tetsuya Uemura, Masafumi Yamamoto, Yoshio Miura, and Masafumi Shirai, "Enhanced half-metallicity of off-stoichiometric quaternary Heusler alloy Co_2(Mn,Fe)Si investigated through saturation magnetization and tunneling magnetoresistance", Phys. Rev. B, vol. 93, 134403 (15pp), 2016.

2. Kidist Moges, B. Hu, H. Liu, T. Uemura and M. Yamamoto, "Bias Voltage Dependence of the Spin-dependent Tunneling Conductance of Co_2(Mn,Fe)Si-Based Magnetic Tunnel Junctions Exhibiting Giant Tunneling Magnetoresistances", 2015 International Conference on Solid State Devices and Materials (SSDM2015), Extended Abstracts (USB memory), PS-12-5 (2pp), Sapporo, Japan, Sep. 28-30, 2015.

3. Kidist Moges, Hong-xi Liu, Takeshi Kawami, Tetsuya Uemura, and Masafumi Yamamoto, "Half-metallic electronic structure of Co_2(Mn,Fe)Si electrodes investigated through tunneling spectroscopy for fully epitaxial magnetic tunnel junctions", IEEE International Magnetics Conference 2015 (Intermag 2015), Digests (USB memory), GB-06 (2pp), Beijing, China, May 11-15, 2015.

4. Kidist Moges, Y. Honda, T. Uemura, M. Yamamoto Y. Miura and M. Shirai, "Effect of nonstoichiometry on the half-metallicity of Co_2(Mn,Fe)Si thin films investigated through saturation magnetization", 59th Annual Conference on Magnetism and Magnetic Materials (MMM), Abstracts (USB memory), pp. 48−49, AH-08, Honolulu, Hawaii, USA, November 3–7, 2014.

5. Kidist Moges, Bing Hu, Tetsuya Uemura, and Masafumi Yamamoto, "Bias voltage dependence of the spin-dependent tunneling conductance of Co_2(Mn,Fe)Si/MgO-based MTJs showing giant tunneling magnetoresistance ratios", to be submitted.

2. Publications related to other researches

1. Hong-xi Liu, Takeshi Kawami, Kidist Moges, Tetsuya Uemura, Masafumi Yamamoto, Fengyuan Shi and Paul M. Voyles, "Influence of film composition in quaternary Heusler alloy $Co_2(Mn,Fe)Si$ thin films on tunnelling magnetoresistance of $Co_2(Mn,Fe)$/MgO-based magnetic tunnel junctions", J. Phys. D: Appl. Phys., vol. 48, 164001 (9pp), 2015.

2. B. Hu, Kidist Moges, H. Liu, Y. Honda, T. Uemura and M. Yamamoto, "Temperature Dependence of Spin-Dependent Tunneling Conductance of Magnetic Tunnel Junctions with Highly Spin-Polarized Electrodes", 2015 International Conference on Solid State Devices and Materials (SSDM2015), PS-12-6, Sapporo, Japan, Sep. 28-30, 2015.

3. Bing Hu, Hong-xi Liu, Takeshi Kawami, Kidist Moges, Yusuke Honda, Tetsuya Uemura, and Masafumi Yamamoto, "Temperature dependence of spin-dependent tunneling resistances of Co_2MnSi-based and $Co_2(Mn,Fe)Si$-based magnetic tunnel junctions showing high tunneling magnetoresistances", IEEE International Magnetics Conference 2015 (Intermag 2015), GB-11, Beijing, China, May 11-15, 2015.

4. T. Kawami, H. Liu, Y. Honda, Kidist Moges, T. Uemura, F. Shi, P. M. Voyles and M. Yamamoto, "Giant tunnel magnetoresistance in fully epitaxial $Co_2(Mn,Fe)Si$/MgO/$Co_2(Mn,Fe)Si$ magnetic tunnel junctions", 58th Annual Conference on Magnetism and Magnetic Materials, Abstracts, P. 614, FX-03, Denver, Colorado, USA, November 4 – 8, 2013.

5. Bing Hu, Kidist Moges, Yusuke Honda, Hon-xi Liu, Tetsuya Uemura, and Masafumi Yamamoto, Jun-ichiro Inoue, and Masafumi Shirai, "Temperature dependence of spin-dependent tunneling conductance of magnetic tunnel junctions with half-metallic Co_2MnSi electrodes", (submitted).

3. Presentations

1. Kidist Moges, B. Hu, H. Liu, T. Uemura and M. Yamamoto, "Bias Voltage Dependence of the Spin-dependent Tunneling Conductance of Co_2(Mn,Fe)Si-Based Magnetic Tunnel Junctions Exhibiting Giant Tunneling Magnetoresistances", 2015 International Conference on Solid State Devices and Materials (SSDM2015).

2. Kidist Moges, Hong-xi Liu, Takeshi Kawami, Tetsuya Uemura, and Masafumi Yamamoto, "Half-metallic electronic structure of Co_2(Mn,Fe)Si electrodes investigated through tunneling spectroscopy for fully epitaxial magnetic tunnel junctions", IEEE International Magnetics Conference 2015 (Intermag 2015).

3. Kidist Moges, Y. Honda, T. Uemura, M. Yamamoto Y. Miura and M. Shirai, "Effect of nonstoichiometry on the half-metallicity of Co_2(Mn,Fe)Si thin films investigated through saturation magnetization", 59th Annual Conference on Magnetism and Magnetic Materials (MMM 2014).

4. Kidist Moges, Bing Hu, T. Uemura and M. Yamamoto, "Origin of the strong bias voltage dependence of tunneling conductance for the antiparallel configuration of Co_2(Mn, Fe)Si-based magnetic tunnel junctions", 51st Conference of Hokkaido Chapter, The Japan Society of Applied Physics (2016).

5. Kidist Moges, Bing Hu, Honxi Liu, Tetsuya Uemura, and Masafumi Yamamoto, "Spin dependent tunneling conductance characteristics of half-metallic Co_2(Mn,Fe)Si based magnetic tunnel junctions", 76th Autumn Meeting 2015, The Japan Society of Applied Physics (2015).

6. Kidist Moges, Yusuke Honda, Bing Hu, Honxi Liu, Tetsuya Uemura, and Masafumi Yamamoto, "Effect of off-stoichiometry on the half-metallicity of quaternary Heusler alloy Co_2(Mn,Fe)Si investigated through saturation magnetization and tunneling magnetoresistance", 39th Fall Annual Conference

on MAGNETICS in Japan (2015).

7. Kidist Moges, Bing Hu, Tetsuya Uemura, and Masafumi Yamamoto, “Bias voltage dependence of spin-dependent tunneling conductance of MTJs with Co_2(Mn,Fe)Si electrodes”, 157th Fall Annual Meeting 2015, The Japan Institute of Metals and Materials (2015).

8. Kidist Moges, Yusuke Honda, Tetsuya Uemura, Masafumi Yamamoto, Yoshio Miura and Masafumi Shirai, “Effect of off-stoichiometry on the half-metallic character of Heusler alloy Co_2(Mn,Fe)Si thin films”, 62nd Autumn Meeting 2015, The Japan Society of Applied Physics (2015).

9. Kidist Moges, Y. Honda, T. Uemura, M. Yamamoto, Y. Miura and M. Shirai, “Effect of defects on the half-metallicity of quaternary Heusler alloy Co_2(Mn,Fe)Si thin films”, 50th Conference of Hokkaido Chapter, The Japan Society of Applied Physics (2015).

10. Kidist Moges, Yusuke Honda, Tetsuya Uemura, Masafumi Yamamoto, Yoshio Miura, and Masafumi Shirai, “Effect of nonstoichiometry on the half-metallicity of Co_2(Mn,Fe)Si thin films investigated through saturation magnetization”, 13th Spintronics Seminar and workshop, Oct. 27−29, 2014, Sendai, Japan.